Check for updates

Band-structure tunability *via* the modulation of excitons in semiconductor nanostructures: manifestation in photocatalytic fuel generation

Srabanti Ghosh, [iD] *[a,b] Dipendu Sarkar,[a] Sweta Bastia[b,c] and Yatendra S. Chaudhary [iD] [b,c]

Understanding the energetics of electron transfer at the semiconductor interface is crucial for the development of solar harvesting technologies, including photovoltaics, photocatalysis, and solar fuel systems. However, modern artificial photosynthetic materials are not efficient and limited by their fast charge recombination with high binding energy of excitons. Hence, reducing the exciton binding energy can increase the generation of charge carriers, which improve the photocatalytic activities. Extensive research has been dedicated to improving the exciton dissociation efficiency through rational semiconductor design *via* heteroatom doping, vacancy engineering, the construction of heterostructures, and donor−π−acceptor (D−π−A) interfaces to extend the charge carrier migration, promoting the dissociation of excitons. Consequently, functionalized photocatalysts have demonstrated remarkable photocatalytic performances for solar fuel production under visible light irradiation. This review provides the fundamental aspects of excitons in semiconductor nanostructures, having a high binding energy and ultrafast exciton formation together with promising photo-redox properties for solar to fuel conversion application. In particular, this review highlights the significant role of the excitonic effect in the photocatalytic activity of newly developed functional materials and the underlying mechanistic insight for tuning the performance of nanostructured semiconductor photocatalysts for water splitting, CO_2 reduction, and N_2 fixation reactions.

1 Introduction

Solar to fuel conversion is one of the well-recognized energy conversion technologies, where solar radiation delivers energy in the form of heat, electricity, or photons to convert H_2O and CO_2 into fuels.[1–3] Materials with ultrahigh photocatalytic efficiency may sustainably enhance the solar-to-chemical conversion but are limited by their sluggish redox reactions. Thus, significant effort has been devoted to optimizing the photocatalytic activities and electronic structures of semiconductors, which play a pivotal role in driving solar-to-chemical conversion reactions, such as water reduction into hydrogen, CO_2 reduction into C1 and C2 products, dinitrogen reduction into ammonia, and H_2O_2 from O_2 and H_2O.[4–8] There are many reviews in literature, which excellently summarize the development of photocatalysts for various redox reactions, such as water splitting, CO_2 reduction, and N_2 fixation.[9–15] To date, many reviews focused

on low-dimensional semiconductor materials and the influence of heterostructures; however, the progress on the impact of excitonic processes involved in photocatalysts has rarely been summarized.[16–18] Excitons are distinct electron–hole pairs generated by the photoexcitation process and bound together by Coulomb interaction. To acquire completely dissociated charges, the exciton activation energy (E_a) must be higher than the exciton binding energy (E_b, order of 0.1 eV to 0.5 eV), which contributes to outstanding efficiency for solar fuel production. Hence, a deep understanding of the modulation of band structures and charge separation, the development of models of material behaviour, and optimizing their active functions during photocatalytic applications are highly required. Notably, the dissociation of excitons occurs at the interface of the semiconductor heterojunction due to the presence of a built-in electric field, which further prevents the recombination of excitons and promotes photocatalytic redox reactions. For example, 2D–2D p-MoS_2/n-$MgIn_2S_4$, which is a Type II heterojunction, demonstrated improved exciton dissociation as electrons migrates from the more negative potential of p-MoS_2 to the less negative potential of n-$MgIn_2S_4$ and the holes migrate to the opposite direction under irradiation.[19] Homojunctions follow a similar trend in promoting exciton dissociation and suppressing exciton recombination.[20] For example, Wang *et al.*[21] pro-

[a]Energy Materials & Devices Division, CSIR – Central Glass and Ceramic Research Institute, Raja S. C. Mullick Road, Jadavpur, Kolkata 700032, India. E-mail: ghosh.srabanti@gmail.com, srabanti@cgcri.res.in
[b]Academy of Scientific & Innovative Research (AcSIR), Ghaziabad, India
[c]Materials Chemistry Department, CSIR-Institute of Minerals and Materials Technology, Bhubaneswar 751013, India

posed that both singlet and triplet excitons dissociate into electrons and holes at the order–disorder interfaces of the homojunction-like structure. In another approach, the selective extraction of electrons and lowering of charge recombination were observed in an ordered graphitic carbon nitride (g-C$_3$N$_4$) chain. The ordered g-C$_3$N$_4$ possesses lower HOMO and LUMO energy levels, which promote electron injection in comparison to disordered structures, as validated by density functional theory (DFT) simulations.[22–33] This review aims to highlight the fundamental understanding of electron behaviours of photocatalysts and recent impressive progress in electronic structure–property–function relationship in photocatalysis. The present review provides a detailed description of the diverse approaches such as surface modification, heteroatom doping, vacancy engineering, band structure tuning, and heterostructure engineering to regulate the electronic structures of semiconductors. Furthermore, we correlate the advantages of electronic-structure engineering and highlight various excitonic processes in several photocatalysts including metal oxides, metal sulfides, oxyhalides, metal nitrides, metal carbides (2D layered structures and bismuth-containing materials), organic semiconductors (COF, g-C$_3$N$_4$, etc.) and heterostructures for various photocatalytic reactions by combining experimental results with fundamental DFT analysis.[34–40] Recently, the photocatalytic nitrogen reduction reaction has been considered as an alternative route to realize the green synthesis of NH$_3$. However, its insufficient conversion

with a low NH$_3$ yield remains a significant challenge. The nitrogen reduction reaction (NRR) performance is intrinsically related to the electronic structure of catalysts, and thus the conversion efficiency can be improved via rational catalyst design, such as introducing vacancies, constructing a heterointerface and exciton modulation.[41–51] A summary of the recent development of photocatalysts through the modulation of excitons is presented in Fig. 1a. Moreover, a correlation with the function of excitons in photocatalysis and solar fuel production is established. Considering the significance of the excitonic effect in photocatalysis and the potential of newly developed functional materials, a comprehensive review on evaluating excitonic effects to study the mechanism of nanostructured photocatalysts is urgently needed. Finally, insights into the challenges and opportunities of the excitonic effect in photocatalytic materials are presented.

2 Excitonic modulation in semiconductors for photocatalytic activity

2.1 Role of excitons in photocatalysis

Excitons are photoexcited electron and hole pairs, which are formed when light is absorbed by semiconductors and play a
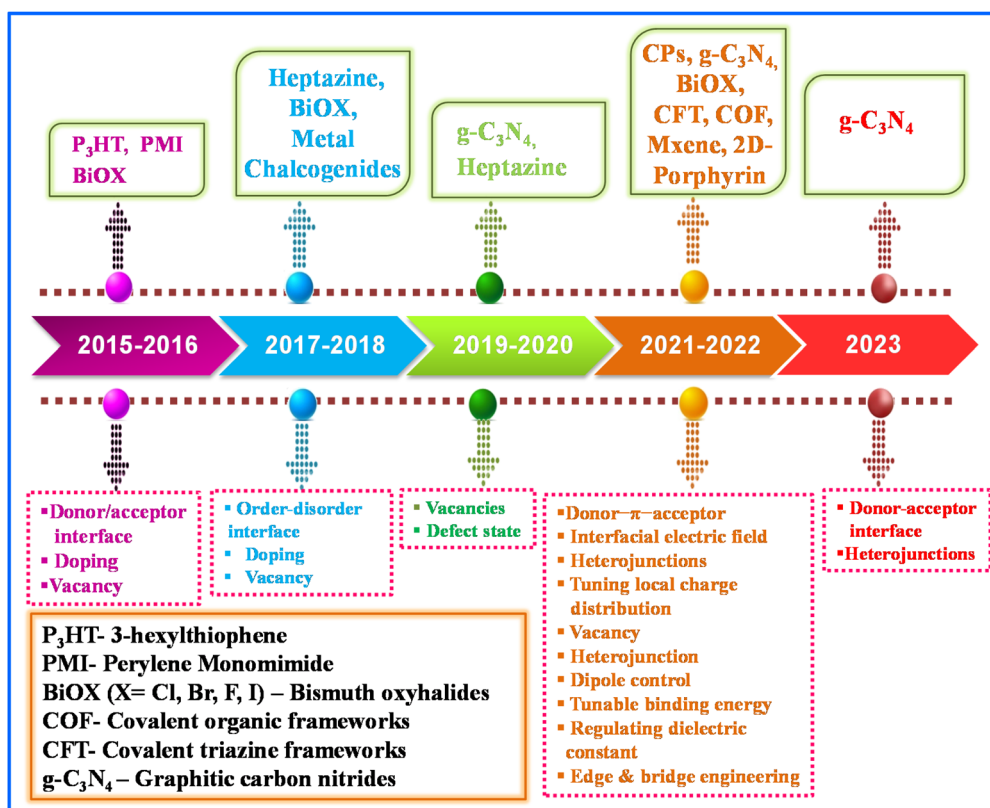

Fig. 1 Timeline showing the development of photocatalysts through the modulation of excitons for photocatalytic applications.

crucial role in photocatalytic applications. The first question that arises is why excitons play a role in semiconductors? This is because the importance of the excitonic effect on semiconductors has not been fully studied to date. Generally, the efficiency of photocatalysis is considered in terms of the separation and transfer of photo-generated charge carriers during the reduction and oxidation of water (water splitting) and CO_2 reduction, neglecting excitonic effects. Notably, the binding energy of photo-generated excitons strongly depends on the corresponding energy states due to the quantum confinement effect in low-dimensional (0D, 1D, and 2D) semiconductors. To achieve high photocatalytic activity, excitons must be dissociated into electron–hole pairs, which occurs when the binding energy of the excitons (E_b) is less than $T\Delta S_{diss}$, where T is room temperature and ΔS_{diss} is the increase in entropy due to exciton dissociation.[52] In the quasi-equilibrium process, the relationship between excitons (n_x) and dissociated photogenerated electron–hole pairs ($n_e = n_h = n_c$) is as follows (eqn (1)):[53]

$$n_c^2 = n_x T^{\frac{3}{2}} \exp\left(\frac{-E_b}{2K_B T}\right) \quad (1)$$

where T is the temperature, E_b is the exciton binding energy, and K_B is the Boltzmann constant. When the other parameter are constant, the number of available free carriers (n_c) may be reduced by a factor with an increase in E_b. Consequently, the reduction in n_c directly reduces the photocatalytic efficiency of a semiconductor. Moreover, an additional limitation of low-dimensional semiconductors is their fast recombination of electron–hole pairs, which can be defined by the Auger recombination process (R_{Auger}), where the rate of recombination is $R_{Auger} \propto E_b^3$.[54] Hence, it is important to consider the exciton effect in low-dimensional semiconductors to achieve high photocatalytic activity. It is noteworthy that excitons are situated just below the bottom of the conduction band (CB), which may be labelled by the principal quantum number $n = 1, 2, 3$, etc. due to the lower energy of excitons than conduction electrons. As n increases, the excitonic energy increases with a shift in its energy level towards the bottom of the CB (Fig. 2a). Now, considering the low-dimension of semiconductors, the photo-generated free electrons at the bottom of the CB and holes at the top of the valence band (VB) are bound by releasing extra energy, which are called "quasiparticles" or "excitons". Nevertheless, the electrons in the CB are termed "CB energy (E_C)", and similarly the holes in the VB are named "VB energy (E_V)". Thus, the wavefunctions of electrons and holes
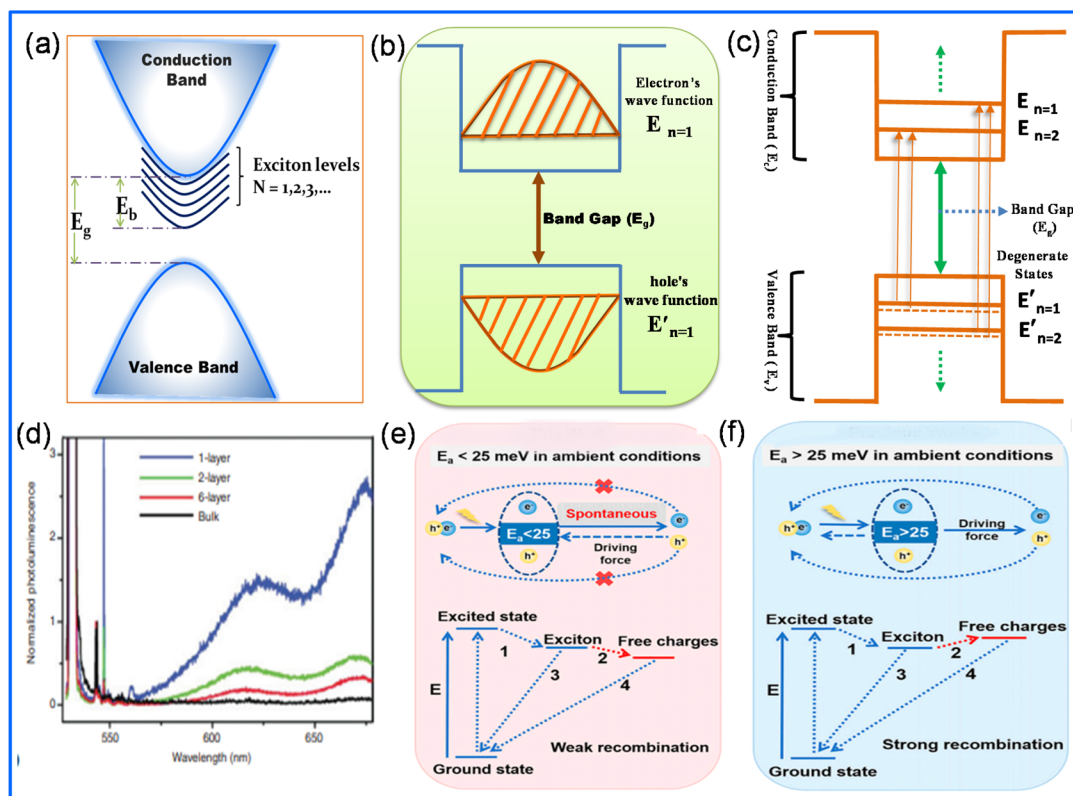

Fig. 2 (a) Illustration of excitonic energy levels. (b) Electrons and holes bound wave function in the CB and VB. (c) Diagram of discrete energy levels. Electron transfer from degenerate VB energy levels to non-degenerate CB energy level (allowed transition, $\Delta n = 0$). Valence energy bands are double degenerate with light holes and heavy holes. (d) PL spectra of MoS_2 from bulk to monolayer. Reproduced with permission from ref. 55. Copyright 2010, the American Chemical Society. (e) and (f) Pathway for the generation of free charge carriers by exciton dissociation. Reproduced with permission from ref. 58. Copyright 2022, Proc. Natl. Acad. Sci. U. S. A.

are confined/localized/bound in the potential, which is called quantum confinement, as shown in Fig. 2b. Fig. 2c shows the discrete energy levels in both the VB and CB; however, the presence of "light holes" and "heavy holes" creates doubly-degenerate energy states with different wavefunctions. It should be noted that $\Delta n = 0$ is the allowed transition but $\Delta n = 1$ is not forbidden (partially allowed). These excitonic transitions may generate sharp peaks in the absorption spectrum and the two peaks observed correspond to the $n = 1$ and $n = 2$ levels due to the presence of degenerate states. Fig. 2d presents the photoluminescence (PL) peaks obtained for MoS_2 mono/bi-layers, indicating the generation and recombination of excitons in low-dimensional systems. In contrast, none of these peaks were observed in their bulk counterpart at room temperature.[55] When thermal energy (K_BT) of a semiconductor is higher than the exciton binding energy ($K_BT > E_B$), excitons will dissociate into free electrons and holes. In general, the thermal energy of semiconductors is around 25 meV at room temperature; however, the E_b of excitons is in the range of 0.1 eV–0.5 eV, which is significantly higher than thermal energy. If E_b is not high enough, then the dissociated charge carriers become strongly attracted and recombine (Fig. 2e). Thus, to overcome this obstacle, various strategies such as the application of an external field including electric, magnetic, and stress with varying strengths can be used as a driving force in the opposite direction of the coulomb force between electron–hole, reducing E_b, which leads to a lower excitonic binding energy compared to the room temperature thermal energy, as shown in Fig. 2f.[56,57] Finally, excitons may dissociate to charges, promoting their participation in photocatalysis (Fig. 2f).[58]

2.2 Size- and dimensionality-dependence of excitonic effects

The size- and dimensionality-dependence of excitonic effects in semiconductor nanostructures have been identified to be important parameters to develop efficient nanoscale excitonic photocatalysts.[59–63] Notably, the excitonic effects are significantly enhanced with a reduction in the size of the semiconductor nanostructure compared to the bulk exciton Bohr radius. Furthermore, the lifetime of low-dimensional excitons becomes longer in comparison to bulk excitons due to the differences in the confinement dimensionality. Subsequently, improved electron–hole exchange interactions are expected in low-dimensional structures owing to the enriched excitonic effects. Recently, several new 2D materials have emerged, for example, interfacing semiconducting transition-metal dichalcogenide (TMD) monolayers with other patterned 2D materials such as hexagonal boron-nitride (hBN), which can effectively modulate the exciton energy landscape without altering its properties.[64,65] Conceptually, low-dimensional systems can be identified as 0D (e.g., quantum dots and nanoclusters), 1D (e.g., nanorods and nanotubes) and 2D (e.g., sheets, plates, and layered structures). Considering multidimensional aspects, quantum dots (QDs) do not possess any translational symmetry due to the absence of dimensionality. In contrast, quantum wires and quantum wells have translational symmetry in one or two

dimensions; consequently, a large number of excitons can be formed compared to QDs.[66] The separation of quantized energy levels strongly depends on the size of the QDs, for example, smaller quantum dots show larger energy level separation. Alternatively, the band edge points of the CB and VB of bulk materials are close enough to form a quasi-continuous curve. Particularly, the non-zero value of the lowest energy (i.e., the VB energy) of QDs suggests they possess a larger electronic band gap than bulk systems, as shown in Fig. 3a. The band gap of QDs represents the sum of the bulk band gap confinement energy for electrons and holes (excitons) and the coulombic attraction between excitons (eqn (2) and (3)).

$$E_g \ (\text{dot}) = E_g \ (\text{bulk}) + E \ (\text{confinement}) + E \ (\text{coulomb}) \quad (2)$$

The confinement energy:

$$E(\text{confinement}) = \frac{\hbar^2 \chi_{ml}^2}{2Ma^2} \quad (3)$$

where χ_{ml} is the Bessel function, $M = m_e^* + m_h^*$ where m_e^* and m_h^* are the effective masses of electrons and holes respectively, a is the radius of the QDs, and h is Planck's constant.

The coulombic energy (eqn (4)):

$$E(\text{coulombic}) = -\frac{\frac{\mu R_y}{m_0 \varepsilon_r^2}}{n^2} = -\frac{R_X}{n^2} \quad (4)$$

where $R_X = \left(\frac{\mu R_y}{m_0 \varepsilon_r^2} \right)$, which has a constant value for each semiconductor, R_y is the Rydberg constant in the unit of energy, ε_r is the relative permittivity of the semiconductor, n is the principle quantum number, m_0 is the mass of electrons, and $\mu = \frac{m_e^* m_h^*}{m_e^* + m_h^*}$ is the reduced mass of electrons and holes.

The total quantum mechanical energy (E_{nml}) for a particle in spherical potential is as follows (eqn (5)):

$$E_{nml} = E_g - \frac{R_X}{n^2} + \frac{\hbar^2 \chi_{ml}^2}{2Ma^2} \ n, m, l = 1, 2, 3, \dots . \quad (5)$$

Thus, an exciton in a spherical QD is represented by the quantum number, where n corresponds to the internal states generated through Coulomb electron–hole interaction and m and l are related to the center-of-mass motion in the presence of an external potential barrier due to the spherical symmetry. Now, depending on the box radius "a", the confinement can be signified by two parts, as follows:

(i) If a becomes significantly larger than the Bohr radius (a_H), then the excitonic energy shift (ΔE_{nml}) becomes negligible, i.e., "weak Confinement".

(ii) If a becomes significantly smaller than the Bohr radius (a_H), then the excitonic energy shift (ΔE_{nml}) becomes remarkable, i.e., "strong confinement".

Absorption occurs through the optical transitions between the fully discrete energy states in the VBs and CBs, and then the continuous absorption spectrum of a bulk sample is
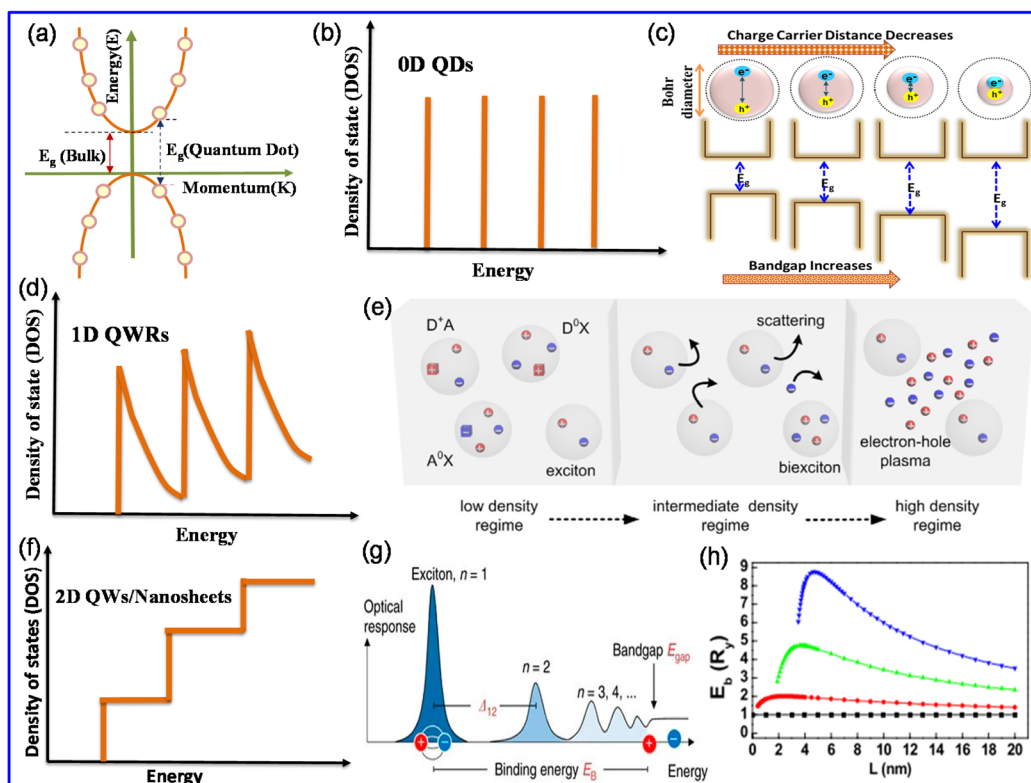
Fig. 3 (a) Energy *vs.* momentum curve for bulk semiconductors (quasi-continuous states) and quantum dots (discrete states). (b) Density of states for QDs. (c) Schematic illustration of size-dependent band gap of CdSe QDs. (d and f) Density of states of 1D nanowires and 2D nanosheets, respectively. (e) Schematic presentation of exciton–exciton interaction in II–VI semiconductors. Cubes and spheres represent the point defects and electrons and holes, respectively. Reproduced with permission from ref. 70. Copyright 2014, IOP Publishing Ltd. (g) Optical response of a 2D semiconductor. Reproduced with permission from ref. 71. Copyright 2017, Nature Publishing Group. (h) Correlation between exciton binding energy *versus* length of semiconductor. Black squares: bulk, blue downward triangles: 0D QDs, green upward triangles: 1D QRs, and red circles: 2D QWs. Reproduced with permission from ref. 72. Copyright 2017, IOP Publishing Ltd.

reduced to a set of discrete sharp lines. The density of states (DOS) in 0D is as follows (eqn (6)):

$$g(E) = \delta\,(E_g - E) \qquad (6)$$

which leads to sharp discontinuous peaks in the DOS lines, as shown in Fig. 3b. Further, the charge separation strongly depends on the size of the QDs, for example, Zhong *et al.*[67] reported the band gap tunability of CdSe QDs in the presence of WS$_2$ nanosheets (NSs). When the band gap of CdSe QDs matched well with that of WS$_2$ NSs, the charge separation was promoted under irradiation.[68] Alternatively, when the dimensions of CdSe QDs was smaller, efficient charge separation and transfer occurred between the CB level of CdSe QDs with the CB of WS$_2$ NSs. However, the difference between these two CBs may causes energy loss due to charge transfer. A schematic of differed sized CdSe QDs with a tunable band gap is shown in Fig. 3c.

In the case of 1D quantum rods (QRs), one degree of freedom may exist and the density of states (DOS) in a set of sub-bands may bunch into sharp peaks, leading to the inverse-

square-root of single particle singularities, as shown in Fig. 3d.[69] The equation of DOS in 1-D is as follows (eqn (7)):

$$g(E) = \frac{m^\star}{\hbar\pi}\sqrt{\frac{m^\star}{2(E_g - E)}} \qquad (7)$$

where $m^\star$ is the effective mass of electrons and E_g is the electronic band gap of the semiconductor.

Xu *et al.*[70] reported a detailed study on the excitonic behaviour of semiconductor nanowires and nanobelts. Mainly, excitons or exciton complexes are separated at a low excitation density due to their lack of interactions (Fig. 3e). However, the excitons are denser due to the increase in their population in the intermediate density regime, which enhances the interaction and scattering between the excitons and exciton complexes, leading to the formation of biexcitons. In the higher density regime, the exciton binding energy significantly decreases due to the lower electron–hole attraction energy, which causes the dissociation of excitons into electron–hole plasma. The understanding of the excitonic behaviour of semiconductors in nano-dimensions plays a crucial role in energy conversion device applications. Notably, the DOS is indepen-

dent of energy and a constant absorption up to some range of energy and discreet spectrum is observed in the absorption spectra of 2D semiconductors (Fig. 3f). The density of states in 2D quantum nanosheets (QNSs) or quantum wells (QWs) can be written in terms of energy (eqn (8)), as follows:

$$g(E) = \frac{m^*}{\pi\hbar^2}\sigma(E_g - E) \tag{8}$$

Raja *et al.*[71] showed the relationship between excitonic energy levels and the electronic bandgap of 2D semiconductors. The difference between the electronic band gaps and quantized excitonic energy levels defines the excitonic binding energies. Fig. 3g illustrates Δ_{12} as the excitonic binding energy of the ground state, corresponding to the $n = 1$ state. In each quantized level, the excitonic energy decreases with an increase in n following the Rydberg equation (eqn (9)):

$$E_n = E_g - \frac{\mu e^4}{2\hbar^2\varepsilon^2 n^2} \tag{9}$$

where E_g is the electronic band gap, μ is the reduced mass of electrons and holes and ε is the dielectric constant of the semiconductor. Fig. 3h indicates a strong correlation between the excitonic binding energy *versus* the length of nano/quantum wires, quantum dots, 2D nanosheets and bulk materials.[72] With a decrease in the length of the nanoparticles, E_b increases significantly and reaches a maximum value at a certain length. Mainly, QDs show the highest E_b at a particular length, indicating their maximum bandgap. No significant change was observed in E_b for the bulk, confirming the formation of excitons near the ground state. Furthermore, the coulomb interaction between excitons gets stronger with a reduction in their length, which consequently reduces E_b. Thus, the band gap increases with a decrease in L and may vary with a reduction in dimensionality. The relation between optical bad gap energy and dimension is as follows (eqn (10)):

$$E_{ex} = E_g + \frac{A}{L^B} \tag{10}$$

where E_{ex} is the excitonic energy levels and A and B are constants.

Xiao *et al.*[73] demonstrated the effect of excitons on 2D layered van der Waals materials such as transition metal dichalcogenides (TMDCs) and molybdenum- and tungsten-based disulphides and diselenides (MoS_2, $MoSe_2$, WS_2, WSe_2, *etc.*). Typically, bulk TMDC semiconductors possess an indirect band gap; however, an indirect-to-direct band gap transition occurs when they are mechanically exfoliated to a monolayer. Consequently, the reduced interlayer interactions lower the VB energy, forming a direct band gap with strong photoluminescence emission. In contrast, the absorption spectra of 2D black phosphorus (BP) and 2D tellurium (Te) display strong light absorption in few-layer β-Te from the ultraviolet (UV) band to visible band, as reported by Wu *et al.*[74] Remarkably, a thickness-dependent band dispersion was observed for few-layer β-Te, where the absorption coefficient decreased with an increase in the thickness and interlayer electronic hybridization.

### 2.3 Effect of excitonic dissociation in photocatalysis

Typically, the carrier concentrations of a semiconductor are dependent on the dissociation rate of the excitons, leading to their generation and transport properties, which promote the recombination process. According to Saha–Langmuir, the concentration ratio of excitons to free photoexcited charge carriers can be described as follows (eqn (11)):

$$\frac{x^2}{1-x} = \frac{1}{n}\left(\frac{2\pi\mu k_B T}{h^2}\right)^{\frac{3}{2}} e^{\left(\frac{-E_b}{k_B T}\right)} \tag{11}$$

where x denotes the ratio of free charge carriers to the total number of particles (*i.e.*, free charge carriers and excitons) and n is the total number of energetic particles.

Hence, regulating the dissociation of excitons at the surface of a semiconductor into free photo-redox charge carriers may lower the carrier recombination and increase the number of hot electrons generated. In this case, many effective strategies have been reported to achieve effective exciton dissociation such as creating a donor–acceptor interface, artificially introducing vacancies in semiconductors, applying an external electric/magnetic field opposite to coulomb attraction force, introducing an order–disorder interface, and forcefully doping with semiconductors.[75,76] A different process to modulate dissociate excitons into free charge carriers has been described to realize enhanced photocatalytic activity, as shown in Scheme 1.

For example, Wang *et al.*[77] observed augmented hot carrier generation in heptazine-based melon due to the faster exciton
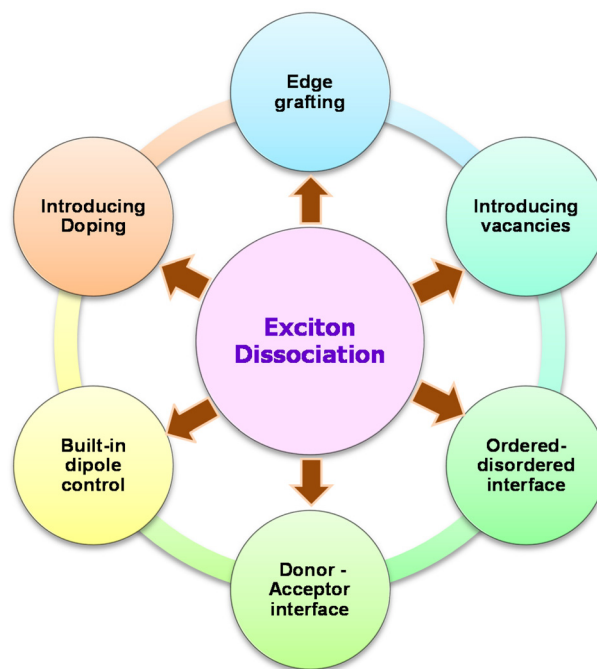
Scheme 1 Schematic representation of different processes to modulate exciton dissociation to promote photocatalytic activity.

dissociation at the order–disorder interfaces. DFT simulations suggested that the ordered chain of heptazine-based melon has slightly reduced highest occupied molecular orbital (HOMO) and lowest unoccupied molecular orbital (LUMO) energy levels compared to the disordered chain. Fig. 4a shows electron transfer towards the ordered chains and hole blocking in the disordered chains, resulting in the separation of the free hot-charge carriers generated in melon. Subsequently, the electrons in the ordered chains migrate towards the surface to participate in the photocatalytic process.

Significant intensity differences in the PL spectra of semi-crystalline heptazine-based melon (SC-HM) and pristine HM (Fig. 4b) were observed. Additionally, a blue-shift was observed in the PL spectrum of SC-HM, which suggests reduced the population of singlet excitons (S_1). The time-resolved photo-luminescence (TRPL) spectra showed a decrease in lifetime from 4.75 ns to 1.10 ns for the pristine HM and SC-HM, as shown in the inset of Fig. 4b, which indicates an enhancement in singlet exciton dissociation to free hot-charge carriers in

SC-HM. Moreover, SC-HM exhibited weakened p-type delayed fluorescence with respect to pristine-HM, representing a decrease in the triplet exciton concentration, as displayed in Fig. 4c. Moreover, the inset of Fig. 4c indicates the delayed fluorescence lifetimes of the pristine HM and SC-HM at 2.43 ms and 1.93 ms, respectively, which indicate an enhancement in the triplet exciton dissociation in SC-HM. Fig. 4d displays the homojunction-like structure in SC-HM, which promotes electron injection toward the ordered chains, whereas hole blocking in the disordered chains. This reduces the charge recombination, consequently facilitating electron migration toward the surface of the semiconductor for photocatalytic processes. Remarkably, low exciton concentrations may reduce the excitonic interactions, and thus enhance the dissociation of excitons. According to the Mott–Schottky analysis, the calculated flat band potential of SC-HM exhibits a more negative value compared to pristine-HM, which indicates the improved reduction ability of SC-HM, as shown in Fig. 4e. The linear sweep voltammetry (LSV) curve showed an enhance-
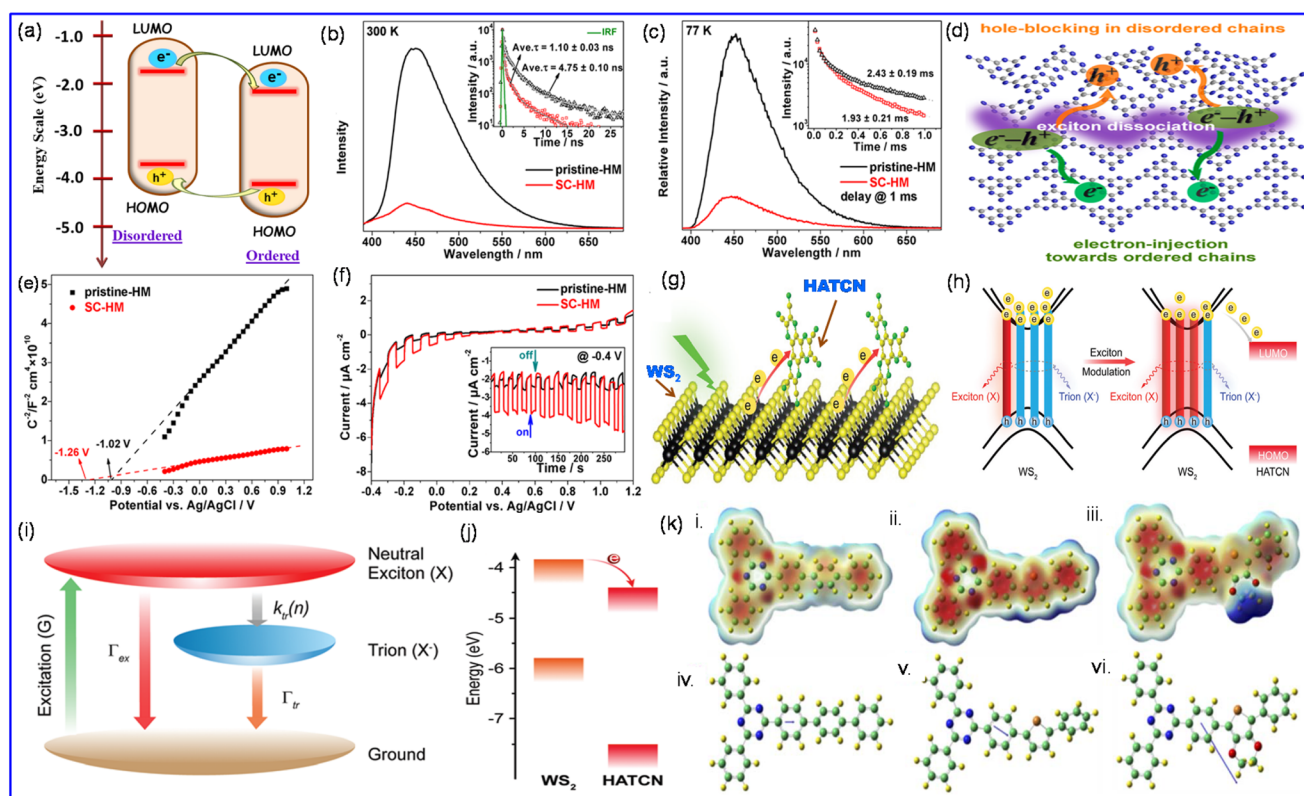

Fig. 4 (a) Schematic illustration of charge transfer mechanism in ordered and disordered heptazine-based chains. (b) Photoluminescence spectra at 300 K (inset: time-resolved PL spectra). (c) PL spectra at 77 K with a 1 ms delay (inset: time-resolved delayed PL spectra). (d) Exciton dissociation and charge transfer in heptazine-based melon. (e) Mott–Schottky curves and (f) potential-bias-dependent photocurrent measurements for pristine-HM (black) and SC-HM (red). Inset: transient photocurrent response. Reproduced with permission from ref. 77. Copyright 2022, the American Chemical Society. (g) Schematic diagram of (HATCN) doping in monolayer WS_2. (h) Schematic presentation of chemical doping-induced exciton modulation in WS_2. (i) Proposed three-energy level model, where G represents the excitation of excitons, $k_{tr}(n)$ is the generation rate of trions (X^-) from neutral excitons (X) after doping, and Γ_{ex} and Γ_{tr} represent the decay rates of neutral excitons and trions, respectively. (j) Schematic presentation of charge transfer mechanism between CB of WS_2 and LUMO of HATCN. Reproduced with permission from ref. 78. Copyright 2018, The Royal Society of Chemistry. (k) (i–iii) Charge distributions in Ph-CTF, Th-CTF, and DD-CTF and (iv–vi) molecular dipoles for the oligomers of Ph-CTF, Th-CTF, and DD-CTF, respectively. Reproduced with permission from ref. 79. Copyright 2022, The Royal Society of Chemistry.

ment in current at negative bias for SC-HM compared to pristine-HM (Fig. 4f). The transient photocurrent spectra indicate the better stability of SC-HM in comparison to HM (inset in Fig. 4f). In another example, Tao et al.[78] proposed that chemically doped TMDCs possess remarkable PL due to the presence of extra electrons, which reduce the bonding of electrons with excitons (known as trions) through charge transfer from TMDCs to the dopant chemical. Fig. 4g shows the doping of p-type hexaazatriphenylenehexacarbonitrile (HATCN) in monolayer WS_2. Fig. 4h demonstrates the mechanism of doping HATCN on monolayer WS_2. A three-level model was considered to understand the variation in PL intensity in HATCN-doped WS_2 (Fig. 4i). The radiative decay rate of trions is significantly lower than that of excitons. After doping, the trions in the doped monolayer WS_2 can be converted to neutral excitons through the transfer of excess electrons from the CB of WS_2 to the CB of HATCN, consequently generating free charge carriers, as shown in Fig. 4j. Zhang et al.[79] proposed a unique approach to modulate the excitonic binding energy via built-in dipole control in covalent triazine frameworks (CTFs). By integrating several functional groups such as phenyl (Ph), thiophene (Th), and 2,3-dihydrothieno dioxine (DD) moieties into CTFs, the E_b was significantly lowered, which caused the dissociation of excitons, and thus the generation of free charge carriers. The mechanism behind lowering the binding energy was supported by DFT calculations, as shown in Fig. 4k. Notably, a more positive charge distribution was observed in

the oligomers of Th-CTF and DD-CTF than that of Ph-CTF, which enhanced the separation of excitons in Th-CTF and DD-CTF. This promoted the delocalization of the electron cloud, reduced E_b and the excitons became more dissociated in CTFs. In another approach, Shi et al.[80] investigated the faster exciton dissociation in bismuth oxyhalides (BiOX, X = Cl, Br, and I), which further participated in the generation of singlet oxygen ($^1O_2$). Fig. 5a displays the layered BiOX characterized by $[Bi_2O_2]^{2+}$ and $[X_2]$ layers interacting via weak van der Waals forces.[81] BiOX is composed of a tetragonal matlockite crystalline structure and with an increase in the atomic number of X, the absorption range of incident photons shifted from UV light (BiOCl) to red light (BiOI). Remarkably, the band gap gradually decreased with an increase in atomic number, as shown in Fig. 5b. The difference between the mechanisms of the charge transfer process and exciton-involved energy transfer process was examined based on photocatalytic activity. Fig. 5c demonstrates the charge-carrier-involved process of photogenerated excited electrons, which localized in the electron trap state (ETS) and electrons can participate in the catalytic process. Additionally, the excitons in the singlet excited state (S_1) may transfer to the triplet excited state (T_1) by intersystem crossing (ISC), which participate in photocatalytic activity (Fig. 5d).

Xing et al.[82] proposed edge grafting in porous ultrathin tubular graphitic carbon nitride (TCN) using L-cysteine (Lc), which can dissociate excitons into free electrons and holes as
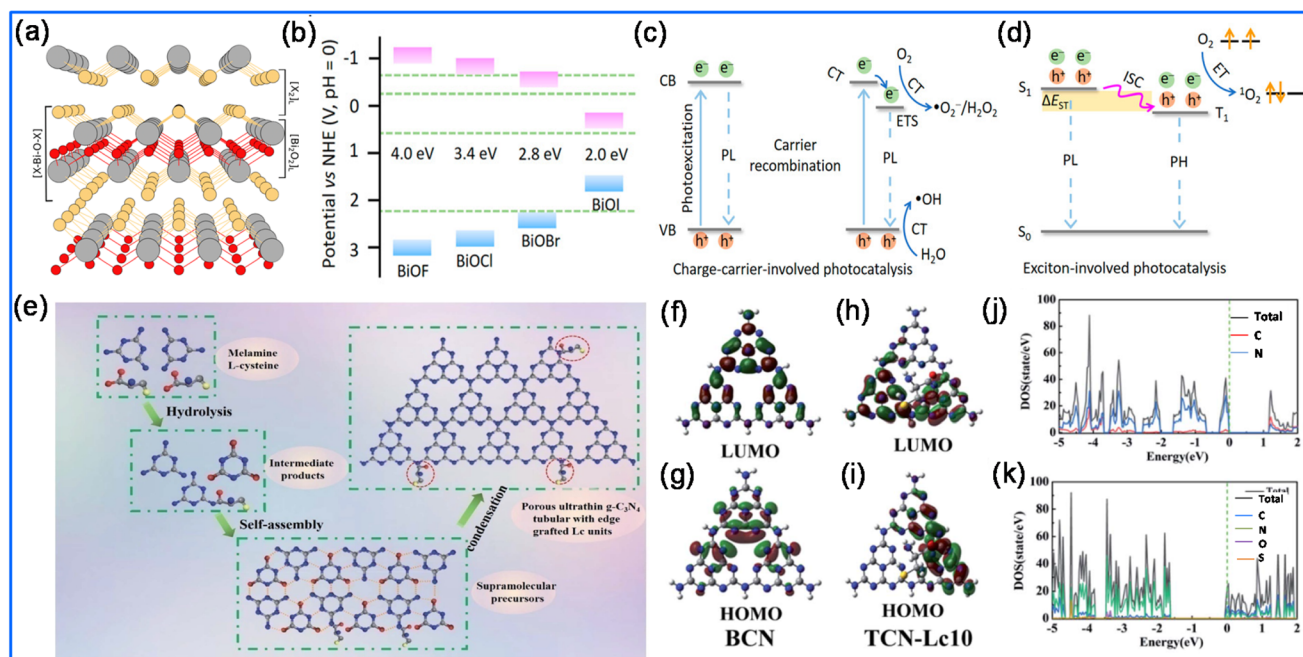

Fig. 5 (a) Crystal structure of BiOX systems. The elements Bi, X, and O are shown in grey, yellow, and red, respectively. Reproduced with permission from ref. 81. Copyright 2022, the American Chemical Society. (b) Band gaps of BiOX. (c) Superoxide radical generation by charge transfer process via the generation of electron trap states. (d) Generation of singlet oxygen by energy transfer (ET) process via the generation of triplet excited states. Reproduced with permission from ref. 80. Copyright 2022, the American Chemical Society. (e) Schematic diagram of the polymerization process of TCN-Lc10. (f) and (g) LUMO and HOMO energy states of BCN, respectively. (h) and (i) LUMO and HOMO energy states of TCN-Lc10, respectively. Density of states of BCN (j) and TCN-Lc10 (k). Reproduced with permission from ref. 82. Copyright 2022, The Royal Society of Chemistry.

well as accelerate charge transfer from g-C_3N_4 (CN) to the active sites (*i.e.*, edge effect). The presence of carboxyl groups in lc and the hydrolysis of melamine into the supramolecular precursors resulted in further stacking in the vertical direction into a 1-D rod-like structure (Fig. 5e). The DFT study revealed the dissociation of the electronic state and formation of disordered interfaces, which promote charge transfer to the surface. The DFT calculations revealed that the LUMO and HOMO states may have originated from the contribution of the C–N bond orbital and connection of nitrogen p_z orbitals in bulk CN (BCN), as shown in Fig. 5f and g. Thus, fast charge carrier recombination may happen due to the availability of two orbitals states in similar tri-s-triazine. Fig. 5h and i show the LUMO located in the C–N bond orbitals around the lc units and HOMO dominated by lc units after introducing 100 mg lc units in TCN (TCN-lc10), which enhanced the charge separation, respectively. According to Fig. 5j and k, it can be concluded that an intermediate band appears in TCN-lc10 across the band gap. In contrast, for BCN, the Fermi level is situated in the mid-band gap, which indicates the presence of a strong localized charge density around tri-s-triazine. Recently, the introduction of a donor–acceptor interface in heptazine-based polymeric g-C_3N_4, namely BPCN, resulted in a lower band gap compared to normal polymeric g-C_3N_4 (PCN), as reported by Xie *et al.*[83] Significantly, the Frenkel exciton gets relaxed to a charge transfer (CT) exciton due to the creation of a donor–acceptor interface, and then dissociates to free charge carriers.[84] The Frenkel excitons relax to CT excitons, which provide excess energy to dissociate into free charge carriers, and the electrons move towards the LUMO of the acceptor, as shown in Fig. 6a. The exciton dissociation rate depends on various parameters such as the exciton binding

energy, dielectric constant of organic materials, LUMO offset between the acceptor and donor, excitonic Bohr radius and reduced mass of excitons. In Fig. 6b, a red shift in BPCN can be observed in the UV-Vis diffuse reflectance spectroscopy (DRS) measurement, which confirms the lowering of the band gap of the semiconductor from 2.76 eV to 2.2 eV. Fig. 6c displays the band structures of PCN and BPCN, a donor–acceptor interface in the polymer system. The exciton binding energy for both PCN and BPCN can be calculated from low-temperature PL spectroscopy (Fig. 6d and e, respectively), suggesting that E_b decreases for BPCN due to the presence of phonon vibration. Notably, higher O_2 evolution was observed for BPCN than PCN due to the generation of a higher number of free holes in the HOMO of the donor (Fig. 6f). Hence, BPCN showed a much higher H_2 evolution and O_2 production rate compared to PCN upon visible-light irradiation (Fig. 6g and h, respectively). This study suggests the advantage of the donor–acceptor interface in the photocatalytic performance.

Nanda *et al.*[85] synthesized CdS–sodium niobate nanorods, which demonstrated a significant enhancement in photocurrent density (7.6 mA cm^{-2} at 0.2 V *vs.* SHE) of ~3 fold higher than bare sodium niobate nanorods. The PL investigation revealed efficient charge carrier separation across the lattice-matched heterointerface, which led to enhanced activity in the hydrogen evolution reaction (HER).[85] Qiu *et al.*[86] theoretically proved that the exciton band structure contains non-analytical discontinuities due to the exchange scattering between electron–hole pairs, as supported by quantum mechanics. Sun *et al.*[87] employed the many-body perturbation theory to investigate the excitonic effects in pure and water-adsorbed g-C_3N_4. Interestingly, the excitonic energy of g-C_3N_4 decreased for the P1 buckled configuration (2.7 eV) in com-
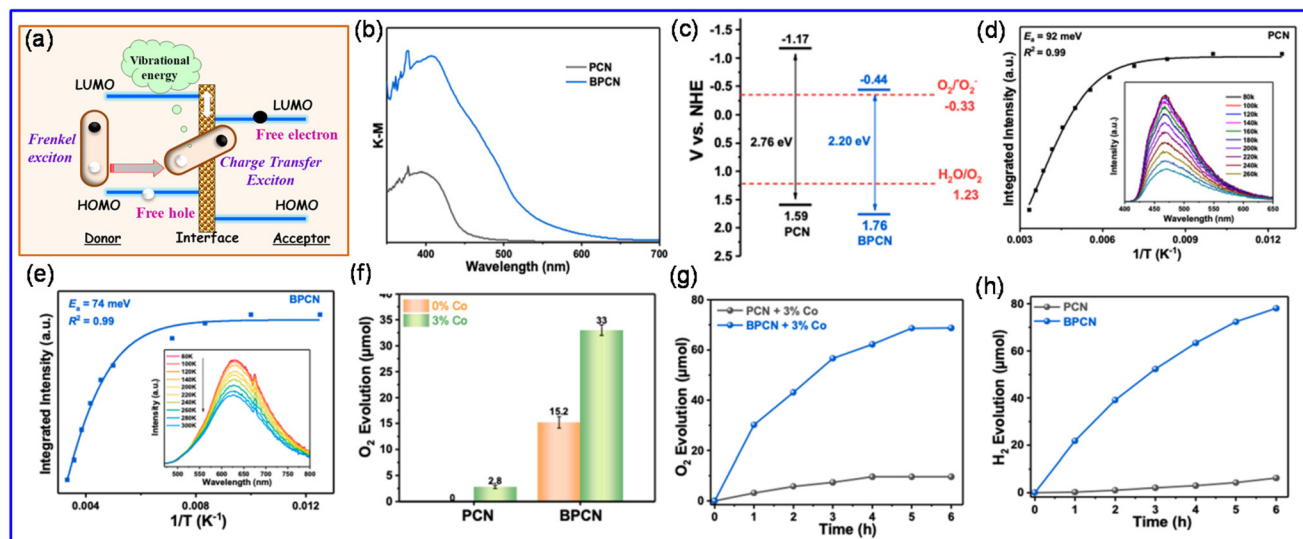

Fig. 6 (a) Frenkel exciton relaxes to charge transfer exciton, which helps to increase the molecular vibrational energy in the form of phonons, and then the vibrational energy dissociates the CT exciton. (b) UV-vis DRS and (c) band structures of PCN and BPCN. Temperature-dependent integrated PL emission intensity (from 80 to 300 K). Inset: PL spectra of (d) PCN and (e) BPCN. (f) O_2 evolution rate of PCN and BPCN. (g) O_2 production with time and (h) H_2 production with time. Reproduced with permission from ref. 83. Copyright 2023, Elsevier Publishing Group.

parison to the high symmetry planar structure (3.8 eV). Chiu et al.[88] successfully demonstrated the surface plasmon resonance-mediated charge transfer via photo-redox hot charge carriers in Au-modified ZnO nanocrystals, resulting in a significant enhancement in visible light-driven photoelectrochemical water splitting. They further established the correlation among Au content, SPR-mediated charge transfer and enhanced photoelectrochemical response due to the generation of the maximum number of hot carriers.

Also, modulation of the charge dynamics in semiconductor heterostructures may enhance the photocatalytic activity, which can be measured by ultrafast laser spectroscopy (transient absorption spectroscopy, time-resolved PL, etc.) and has been studied by several groups.[89–91] Transient absorption spectroscopy (TAS) is a valuable tool for understanding the behaviour of photoexcited charges and the TA signals contributed from excited-state absorption (positive), stimulated emission (negative), and ground-state bleach (negative) are usually directly reported as changes in the optical density (OD) of a photocatalysts. Notably, transient changes in the excited-state features can be directly observed given that different excited states have characteristic absorption behaviours. A continuous kinetic trace from picoseconds to seconds obtained during

semiconductor photocatalysis represents the processes occurring including charge generation, recombination, and interfacial charge transfer. Time-resolved photoluminescence (TRPL) also plays an important role in understanding the fundamental photophysical processes and monitoring the rates of radiative recombination in semiconductor photocatalysts on timescales ranging from femtoseconds to seconds.

The modulation of the exciton dissociation by different strategies reported to date is summarized in Table 1.

### 2.4 Engineering of vacancies in modulation of excitons

Defect engineering is an efficient approach to tune the optical, charge separation, and surface properties of semiconductor materials, which may overcome fast photogenerated charge recombination and poor light absorption.[112] The effect of the introduction of vacancies on the photocatalytic properties of semiconductor materials for photocatalytic hydrogen generation, CO_2 reduction and nitrogen fixation applications is summarized in Table 2. For example, the chemical doping strategy to modulate the optical properties of TMDCs induces excess electrons, which promote the formation of electron-bound trions. Further, the number of trions is reduced through charge transfer from TMDCs to the chemical dopant,

Table 1 Summary of segregation of excitons by different strategies for photocatalysis

Material	Process of dissociation of exciton	Photocatalytic application	Ref.
Perylene monomimide chromophore	Coupling between chromophores	H_2 production	92
Monolayer of WS_2	Phenylenehexacarbonitrile doping	—	78
Graphitic carbon nitride	Edge effect-modulation by edge grafting of tuneable L-cysteine units	H_2 production	82
Heptazine-based melon	Order–disorder interfaces	—	77
Covalent triazine frameworks	Phenyl, thiophene, and 2,3-dihydrothienodioxine in CFT via built-in dipole control	—	79
CdS–sodium niobate nanorod	Lattice matched heterointerface	Water splitting	85
Polymeric carbon nitride	Introducing triazine–heptazine junctions	Water splitting	93
2D porphyrin-based conjugated polymers	Tailoring the binding energy of excitons	CO_2 reduction	94
Pyrene, dibenzo[b,d]thiophene 5,5-dioxide, and diethynyl benzene	Donor–π–acceptor structures	H_2 and O_2 evolution reactions	95
g-C_3N_4	g-C_3N_4 modified with cyano group to promote electron storage ability	—	96
g-C_3N_4	Introducing structural defect	H_2 evolution and H_2O_2 generation	97
g-C_3N_4	Enhanced electron accumulation capacity	H_2 production	98
Ultrathin porous g-C_3N_4	Heterostructure formation with boron nitride quantum dots	O_2 activation	99
g-C_3N_4	Introducing oxygen-substitution	O_2 activation	100
Covalent organic framework	Regulating dielectric constant	H_2O_2 and reactive oxygen species generation	101
Rose flower-like carbon nitride	Heterojunction with biomass-derived carbon dots	H_2O_2 production	102
TiO_2	Formation of heterojunction with black phosphorous quantum dots	H_2 production	103
Carbon nitride	Edge- and bridge-engineering	H_2 production	104
Fe_2O_3-$PrFeO_3$/g-C_3N_4	Double Z-scheme heterojunction	H_2 evolution	105
Carbon nitride	Modulating local charge distribution	Ammonia production	106
Carbon nitride	Construction of K^+ ion gradient	—	107
Porous g-C_3N_4	P-doping	H_2 production	108
Phosphorylated BiOBr	Interfacial electrostatic field	H_2 production and molecular oxygen activation	109
Heptazine-based melon	Defect engineering	O_2 activation and chlorobenzene degradation	110
Selenium- and cyanamide-functionalized heptazine-based melon	Introducing biomimetic donor–acceptor motifs	Hydrogen evolution	111

Table 2 Summary of the separation of excitons by creating vacancies in photocatalysts

Material	Type of vacancy to dissociate excitons	Photocatalytic application	Ref.
BiOBr	O_2 vacancy	O_2 activation	117
BiOCl	O_2 vacancy	CO_2 conversion	118
g-C_3N_4	N_2 vacancy	CO_2 reduction	119
WS_2	S vacancy	—	120
$Bi_{24}O_{31}Br_{10}$	Bi vacancy	Cr reduction	121
$WO_{2.9}$/ g-C_3N_4	O_2 vacancy	—	122
g-C_3N_4	C-Vacancy	CO_2 reduction	123
PbBiO$_2$Br	O_2 vacancy	CO_2 conversion	124
ReS$_2$	S vacancy	CO_2 reduction	125
$Ti_3C_2T_x$/ g-C_3N_4	C-vacancy	CO_2 conversion	126
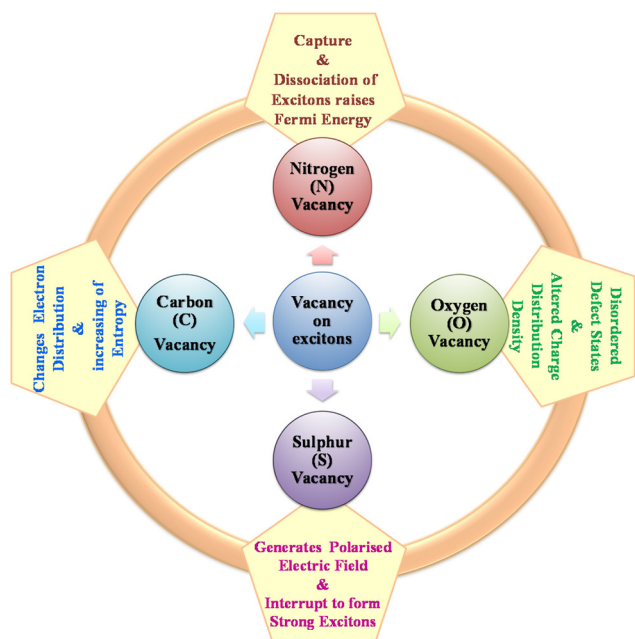
Scheme 2 Schematic representation of the effect of different types of vacancies on excitons.

which is an effective strategy to tune the optical properties *via* exciton modulation, making TMDCs useful semiconductor-based photonic materials. A series of reports highlighted the role of vacancies in low-dimensional materials in their photocatalytic activity, where the coulomb attraction between electrons and holes becomes high, consequently reducing the catalytic activity for hydrogen and oxygen generation. The vacancies create free photogenerated charge carriers and affect the dissociation of excitons to promote the catalytic activity (Scheme 2).

He *et al.*[113] demonstrated a single atomic sulphur (S) vacancy-induced spin polarization electric field (PEF) in CdS NRs, which increased the spatial charge separation and directional charge transfer to the surface redox sites. When S vacancies (S_v) are created, they break the centrosymmetry,

which introduces a net polarization in the unit cell. Consequently, the free electrons in the opposite direction of the coulomb attraction force between electrons and holes may increase the energy of photogenerated charge carriers. Then, the charge carriers can travel from the bulk phase to the surface redox sites, and the recombination rate also decreases. Consequently, the positive and negative charge carriers migrate in opposite directions and participate in the water splitting reaction.

Fig. 7a shows the process for the fabrication of CdS nanorods *via* a simple hydrothermal process, followed by anaerobic heat treatment at different temperatures from 700 °C to 900 °C, which forms S vacancy-containing CdS, denoted as Sv-CdS1, Sv-CdS2, and Sv-CdS3. In Fig. 7b, it can clearly be observed that the S and Cd atoms are staggered, whereas the intensity of the Cd and S atomic columns has no noticeable change with respect to distance in the bulk or on the surface of CdS NRs. In the case of Sv-CdS2, the intensity measurement showed very small differences in the intensities of the Cd atom columns, while that of the S atom intensities was very low at the surface compared to the bulk (Fig. 7c), which represents single-atomic S-vacancy CdS. Regarding Sv-CdS3, a few S atoms and Cd atoms separate from both the surface and bulk phase, which determine the multiatomic vacancies of Cd–S, as shown in Fig. 7d. To further understand the enhancement in catalytic activity, the Hall effect measurement indicated that the Sv-CdS2 NRs have higher Hall mobility and much higher carrier concentration (11- and 34-times) than pure CdS NRs, respectively. Remarkably, Sv-CdS2 satisfied the maximum criteria compared to the other compositions, including the conductivity of charge carriers, as shown in Fig. 7e. This was further supported by transient PL emission spectroscopy, which showed a lower intensity (Fig. 7f) and UV-Vis DRS showed a red-shift in Sv-CdS2, indicating lowering of its band gap, as calculated from the Tauc plot (Fig. 7g and inset). A similar trend was obtained in the photocurrent measurement, with a higher current density for Sv-CdS2 than the other compositions (Fig. 7h). Hence, single atomic S-vacancy-induced PEF in Sv-CdS is efficient for photo-redox activity. Moreover, the introduction of oxygen vacancies in layered low-dimensional bismuth oxyhalides can favourably enhance the dissociation of excitons into free photogenerated charge carriers given that oxygen vacancies manipulate the band-edge charge density near the VB and CB, as proposed by Wang *et al.*[114] Fig. 8a illustrates the delocalization of charge density of Br atoms by O-vacancies (VB-edge charge density mainly dominated by O and Br atoms) at the edge of VB. In contrast, the CB-edge contained the dominant disordered charge distribution by Bi atoms around the O-vacancies, as shown in Fig. 8b. Particularly, Fig. 8c implies the dependency of the band edge charge density on the distance of Bi, O, and Br from the O-vacancies. With a decrease in the distance between the atoms and O-vacancies, the band edge charge density increased rapidly except for O atoms, indicating that the exciton stability became weak for BiOBr. The fluorescence spectra of BiOBr and BiOBr with O-vacancy at room tempera-
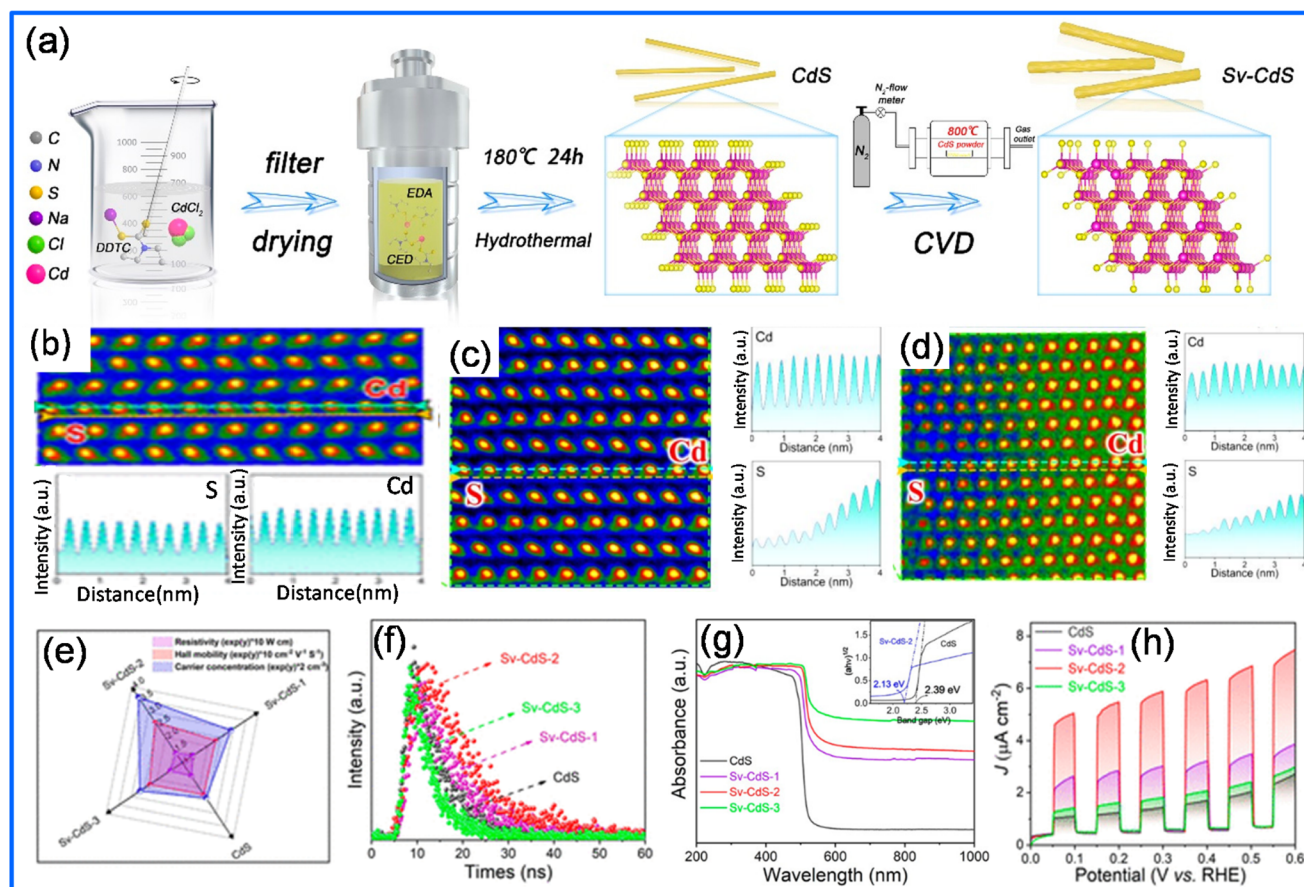
Fig. 7 (a) Fabrication of CdS and Sv-CdS NRs. (b)–(d) Pseudocolor processing image and column intensities of S and Cd atoms of the selected region. (e) Comparison of the Hall effect measurement of four materials, (f) transient PL emission spectra, and (g) UV-vis DRS, and inset: KM plots. (h) Chopped current density *vs.* potential curves. Reproduced with permission from ref. 113. Copyright 2021, the American Chemical Society.

ture (300 K) and low temperature (8 K) showed a blue shift in the second peak (from 610 nm to 570 nm) for BiOBr with O-vacancy because of the reduced exciton–phonon interaction at low temperature (Fig. 8d and e, respectively). The mechanism of O-vacancy-induced exciton modulation is schematically presented in Fig. 8f. After the formation of excitons in the bottom of the CB, the excitons transfer to an intermediate state called the exciton-mediated trap state. Then, the excitons transfer to the O-vacancy-mediated trap state, where the excitons dissociate into free charge carriers, which further participate in the photocatalytic reaction.

Song *et al.*[115] established exciton dissociation by introducing carbon vacancies (V_C) in the $Ti_3C_2T_x$/Vc-CN 2D/2D heterostructure. Zhang *et al.*[116] investigated the band structure modulation of g-C_3N_4 by introducing nitrogen vacancies through the thermal polymerization of urea. Wang *et al.*[117] reported the formation of excitons in the CB of the heterostructure after visible light irradiation, which further transferred to the intermediate state called the exciton-mediated trap state. Then, these excitons transfer to the V_C-modified trap state, where the excitons are relaxed to the defect state, as shown in Fig. 8g. The introduction of nitrogen and carbon

defects in g-C_3N_4 is shown in Fig. 8h, which can modify the electron distribution, enhancing the energy disorder and exciton dissociation. This indicates the formation of free charge carriers and reduces the electron–hole recombination rate. Nitrogen vacancies may capture and dissociate excitons at the energy disordered area. Further, dissociated electrons may raise the Fermi energy (E_F), which causes the CB to move to a negative potential, and due to the confinement effect, the VB potential also becomes more positive, which in turn alters the band gap of N_2 vacancy-modified g-C_3N_4. Fig. 8i shows the EPR spectra of different types of g-C_3N_4 from precursors such as CN-ml (melamine), CN-th (thiourea) and CN-ua (urea). Notably, CN-ml and CN-th have a strong EPR peak due to the presence of an unpaired sp^2 electron, whereas no EPR signal was observed for CN-ua due to the reduced unpaired electron density. It was proposed that the presence of several amino groups in CN-ml may facilitate the recombination process, which reduces the charge separation (Fig. 8j). However, for the other two materials (CN-th and CN-ua), the presence of NVs (nitrogen vacancies) facilitated the separation of excitons into free holes and electrons, leading to an upshift in the Fermi level. In fact, the more positive potential of the VB in low-
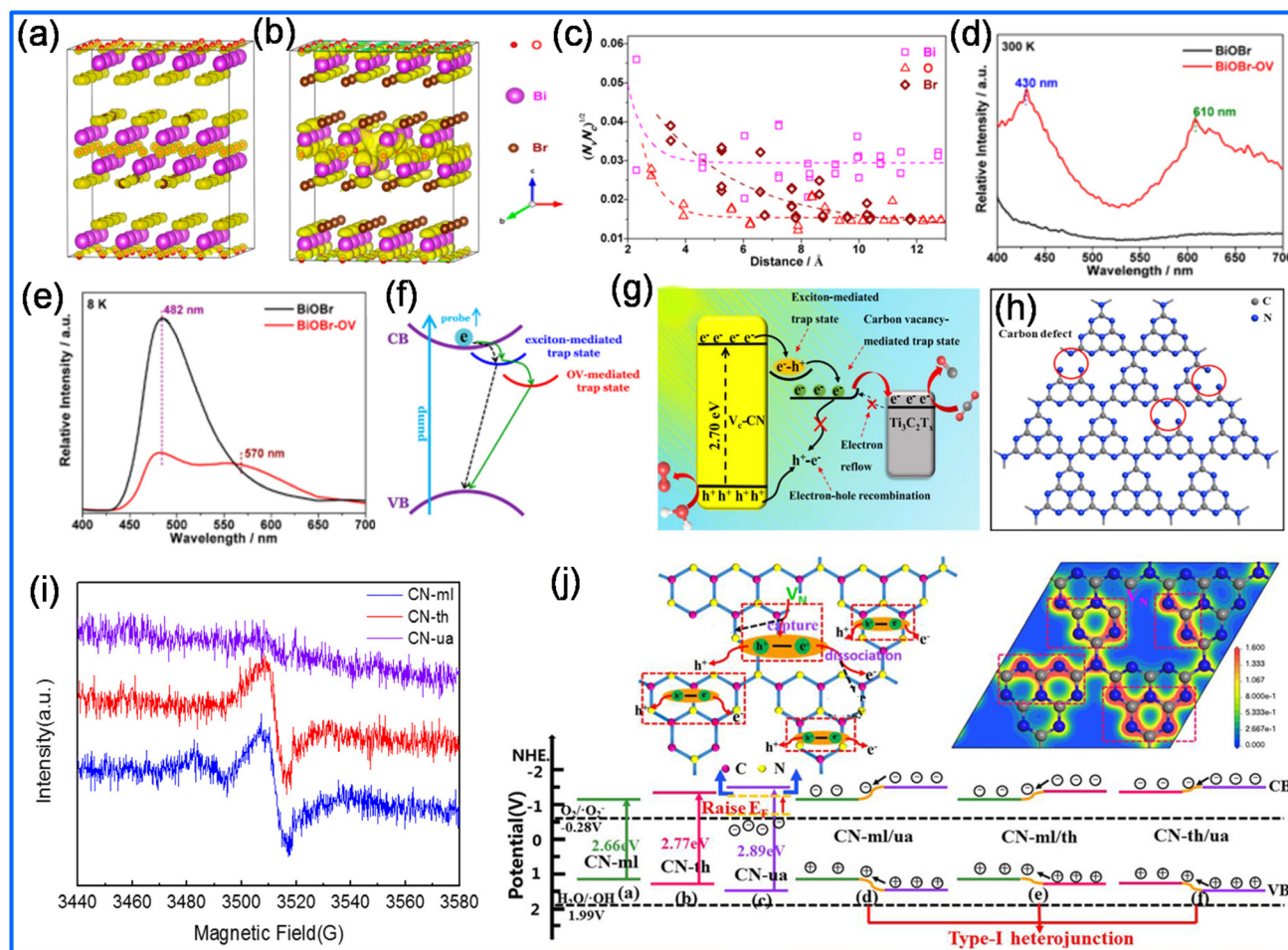
Fig. 8 (a) and (b) VB and CB edge charge density of O-vacancy BiOBr. (c) VB edge charge density (N_v)/CB edge charge density (N_c)^2 vs. distance of the atoms from O-vacancy distribution curve. (d) and (e) Photoluminescence spectra of BiOBr and O-vacancy BiOBr at room temperature (300 K) and low temperature (8 K), respectively. (f) Schematic mechanism of exciton transfer from CB edge to O-vacancy-mediated trap state through exciton-mediated trap state. Reproduced with permission from ref. 114. Copyright 2018, the American Chemical Society. (g) Mechanism of exciton transfer and traps in 2D/2D heterostructure. Vc-CN indicates carbon vacancy-containing CN. (h) Carbon vacancy implementation in g-C$_3$N$_4$. Reproduced with permission from ref. 115. Copyright 2022, Elsevier Publishing Group. (i) EPR spectra of g-C$_3$N$_4$. (j) Schematic diagram of the excitonic dissociation by N$_2$ vacancies. Reproduced with permission from ref. 116. Copyright 2020, Elsevier Publishing Group.

dimensional semiconductors is due to the quantum confinement effect and the broader band gap with strong redox ability.

2.5 Heterostructure engineering

One of the important factors that restricts the overall efficiency of water splitting and photo-reduction of CO$_2$ and N$_2$ is the faster recombination of excitons (~10^{-9} s) compared to electron diffusion to the surface reaction sites of the photocatalyst (10^{-8}–10^{-1} s).[127] Furthermore, it is unlikely that a single photocatalyst will satisfy the two critical parameters, i.e., wide light-absorption range and strong redox ability. Thus, to tune these intriguing elemental processes, the design of heterojunction photocatalysts has been explored. The hetero-junction imparts synergistic properties including high absorption coefficient in the visible light range, high charge carrier mobility, and high dielectric permittivity (diminishes the charge separation dis-

tance at the interface), arising from both semiconducting components. Consequently, this leads to enhanced charge separation at the hetero-interface and reduces the recombination probability. The detailed strategies explored for these reactions are discussed in detail in the following section. The band energy alignment at the interface of two semiconductors is the foundation for the formation of a heterostructure. The resulting heterostructure photocatalysts can achieve excellent photocatalytic efficiency due to the selection of suitable materials, which allow the efficient separation of excitons and broaden the spectral range of light absorption.[128,129] Heterojunctions are formed between the interface of two semiconductors having an unequal band structure, which upon contact realizes band alignment. Fig. 9 shows a heterostructure semiconductor (such as conventional heterojunction, p–n heterojunction and Z-scheme heterojunction) having an intimate interface and with a larger surface area between its constituent, resulting in
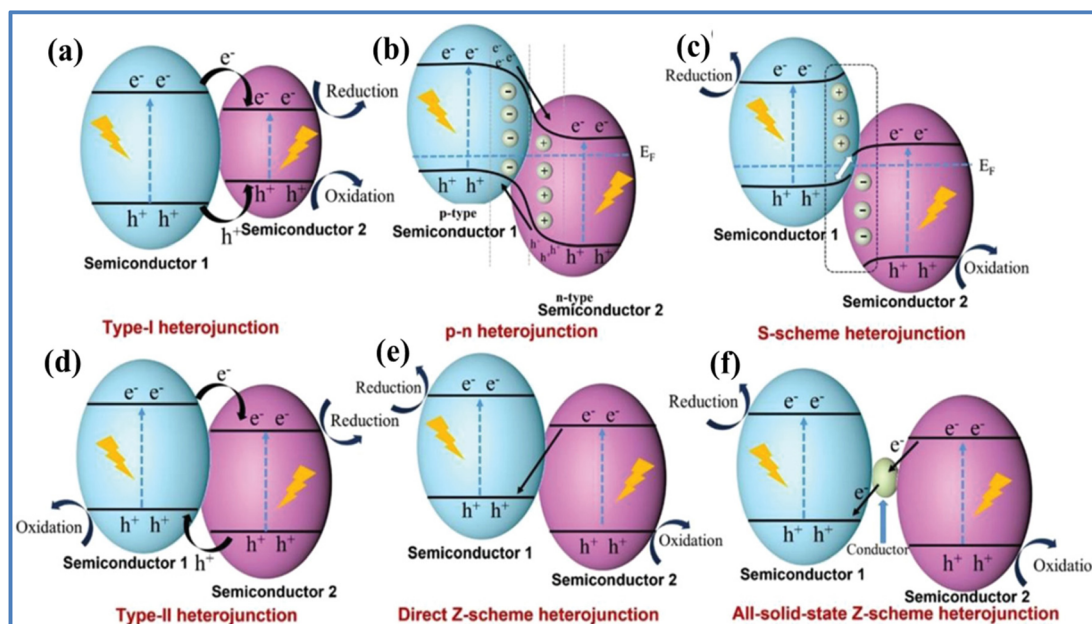
Fig. 9 Schematic illustration of charge separation in a heterojunction. (a) Type-I heterojunction. (b) p–n junction. (c) S-scheme heterojunction. (d) Type-I heterojunction. (e) Direct Z-scheme heterojunction. (f) All-solid-state Z-scheme heterojunction under light irradiation. Reproduced with permission from ref. 132. Copyright 2021, Wiley Publishing Group.

efficient exciton separation and charge transfer across the interface, which leads to an enhancement in photocatalytic conversion.[130,131] Conventional heterojunctions can be classified as straddling heterojunction (Type-I), staggered heterojunction (Type-II), and broken heterojunction (Type-III). To identify the type of heterojunction, first the VB and CB position must be identified. The heterojunction type can be determined based on the knowledge of the relative CB and VB positions.

2.5.1 Type-I heterojunction. In Type-I semiconductor photocatalysts, the band gap of semiconductor 2 is between the band gap of semiconductor 1, and consequently the photocarriers (excitons) migrate to the same semiconductor (Fig. 9a). However, this is not conductive to exciton separation, and thus Type-I semiconductors are less reported.[130] Fan *et al.*[133] reported the synthesis of a heterostructure of g-C_3N_4 with OV-In (OH)$_3$ *via* a precipitation growth method. The as-prepared heterostructure showed excellent photocatalytic nitrogen fixation. g-C_3N_4/γ-Ga_2O_3[134] and MoS_2/C-ZnO[135] are examples of Type-I semiconductors.

2.5.2 Type-II heterojunction. In Type-II semiconductor photocatalysts, both the CB and VB of semiconductor 1 are above the bands of semiconductor 2 (Fig. 9d). This type has the opposite migration of excitons, which results in the confinement of photogenerated electrons and holes in semiconductor 2 and 1, respectively, and consequently the better separation of excitons to participate in redox reactions.[136] Liu *et al.*[137] first reported the preparation of a TiO_2@C and g-C_3N_4 heterojunction of MXene derivatives (Fig. 10a). Its ammonia output under visible light irradiation reached as high as 250.6 μmol g^{-1} h^{-1}. Given that TiO_2 has more positive CB and

VB positions than g-C_3N_4, the photogenerated electrons migrated from the CB of g-C_3N_4 to TiO_2, while the photogenerated holes in the VB of TiO_2 transferred to g-C_3N_4 (Fig. 10b), and eventually the separation efficiency of excitons improved. The major active sites, *i.e.*, the thermally generated Ti^{3+} states from the $Ti_3C_2T_x$ MXene, captured the photoexcited electrons, when they were transferred to TiO_2. In Type-II heterojunction photocatalysts, the N_2 reduction and O_2 evolution processes occur on the semiconductor with lower reduction and oxidation potentials, respectively, significantly decreasing their redox capabilities. Thus, to address the electron–electron repulsion, which will obstruct the charge transfer and separation, the NRR must quickly consume electrons. In this context, heteroatom doping or the addition of surface vacancies and defects can be performed to increase the number of active sites and specific surface area for the adsorption, activation, and reduction of N_2.

2.5.3 p–n junction. The p-type semiconductor in p–n heterojunctions has an E_F close to the VB, while the n-type semiconductor has an E_F close to the CB (Fig. 9b). The Fermi levels of both semiconductors are incrementally approached until becoming equal after they contact and generate an internal electric field. This is due to the difference in electron gain and loss ability of p- and n-type semiconductors as well as the diffusive migration of electrons and holes. Upon illumination, photogenerated electrons and holes migrate to the CB of the n-type semiconductor and VB of the p-type semiconductor, respectively, at the p–n heterojunction.[139] For example, Wang *et al.*[140] successfully synthesized TiO_2/BiOBr p–n heterojunction catalysts *via* the *in situ* growth technique, which showed outstanding photocatalytic nitrogen fixation activity with the
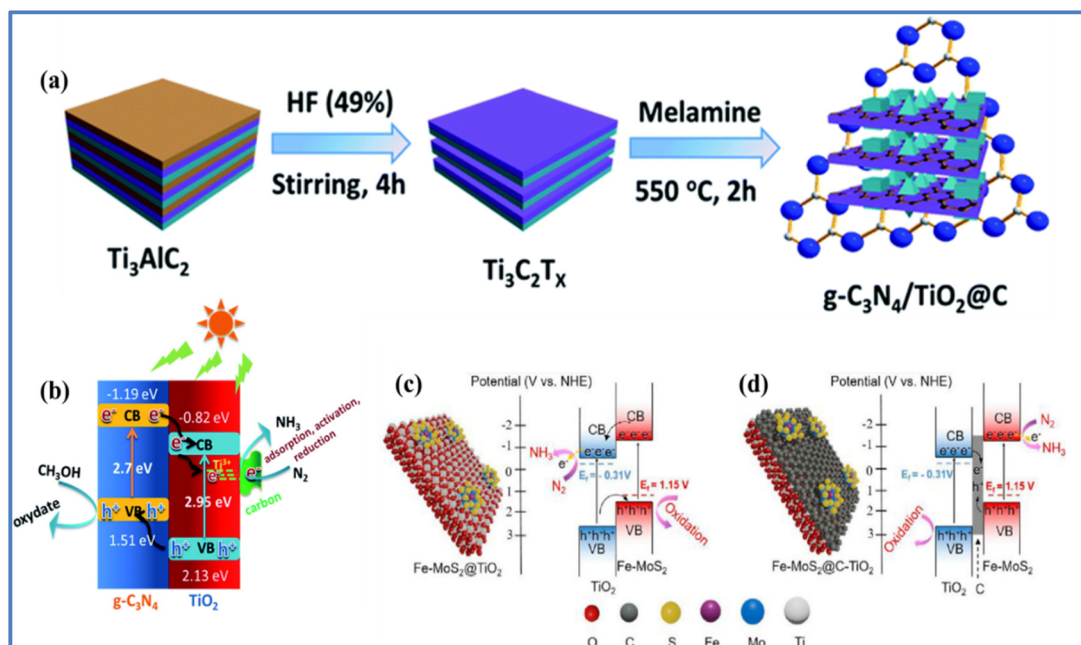
Fig. 10 Schematic illustration of (a) synthesis process of TiO$_2$@C/g-C$_3$N$_4$ and (b) energy band structure and electron−hole separation of TiO$_2$@C/g-C$_3$N$_4$. Reproduced with permission from ref. 137. Copyright 2018, The Royal Society of Chemistry. Schematic presentation of the band alignment of all-solid-state heterojunctions: (c) Fe-MoS$_2$@TiO$_2$ p−n heterojunction and (d) Fe-MoS$_2$@C-TiO$_2$ Z-scheme heterojunction. Reproduced with permission from ref. 138. Copyright 2021, Elsevier Publishing Group.

NH$_3$ production of 1.43 mmol g^{-1} h^{-1}, around 4-times greater than that of pure BiOBr, and strong cycling stability.[136] Other p−n junction photocatalysts have been also reported for water splitting and CO$_2$ and N$_2$ reduction such as Cu$_2$O/CN,[141] Ni$_3$V$_2$O$_8$/g-C$_3$N$_4$,[142] Cu$_2$O/PPy,[139] and ZnO/PDPB.[143–145]

2.5.4 Z-scheme heterojunction. Z-scheme heterojunctions are composed of two semiconductors, *i.e.*, photosystem I (PS I) and photosystem II (PS II), and a conducting medium. These heterojunctions can be broadly categorised as conventional, all-solid-state, and direct heterojunctions.[146,147] In conventional heterojunctions, there is no contact between the two photosystems, as shown in Fig. 9e. However, the use of the free redox ion pairs (such as Fe^{3+}/Fe^{2+}, and IO^{3+}/I) can effectively separate the electron–hole pairs (excitons) and improve the redox ability.[130,148] Song *et al.*[138] fabricated Fe-MoS$_2$@C-TiO$_2$ all-solid-state Z-scheme heterojunction catalysts for photocatalytic nitrogen fixation. The comparison of the Z-scheme heterojunctions with p−n heterojunctions (Fig. 9d and e) showed that the Fe-doped MoS$_2$ nanostructure supplies more active sites, which contribute to the improved performance of the Z-scheme heterojunction. Direct Z-scheme structures are formed by direct contact between the two photosystems (PS-I and PS-II), as shown in Fig. 9f. Direct Z-scheme heterojunctions are frequently utilized for photocatalytic redox reactions and solar to fuel conversion application due to the efficient charge separation with powerful redox active sites.

2.5.5 S-scheme heterojunction. Two semiconductors with different E_F converge to equilibrium after merging in p−n heterojunctions and S-scheme heterojunctions (Fig. 9c), respectively, resulting in the development of an internal electric field at the contact surface. Nguyen *et al.*[149] synthesized zinc oxide/zinc stannate/carbon dot heterostructures (ZnO/ZnSnO$_3$/CDs) *via* the hydrothermal method with an S-scheme structure. These materials were used to study the NRR, and the creation of the heterojunction increased their catalytic performance by 11.5- and 2.1-times compared to ZnO and ZnO/ZnS, respectively. The internal electric field causes the migration of carriers after being stimulated by light energy. Among the various types of heterojunctions, the S-scheme heterojunction has emerged most recently.[150]

3 Role of excitons for solar fuel generation

3.1 Water splitting

Water splitting into hydrogen (H$_2$) and oxygen (O$_2$) using solar energy is exceedingly valuable given that it is an environment-friendly energy source; however, the complexity of the involved multi-electrons remains a major challenge.[151–155] The total quantum yield of free charge carriers is governed by electron–hole pair separation and depends on the nature of materials. In the case of inorganic semiconductors, the formation of heterojunctions and forceful introduction of vacancies increase the entropy of the system and help to dislocate the excitons to free photo redox charge carriers, which participate in the H$_2$ evolution reaction. Due to the low dielectric constant of polymer system, they exhibit a high exciton binding energy. To

regulate excitons, several structural factors need to be introduced for the dissociation of excitons in the energy trap state, which participate in the water redox reaction and produce H_2. Previously in photocatalytic solar fuel generation, most of the work considered the role of free electrons and holes (*i.e.*, charge transfer mechanism), where triplet oxygen ($^3O_2$) is converted into superoxide radical (O_2^{2-}) by combining with free electrons. However, the contribution of excitons is unavoidable for low-dimensional systems, and exciton-mediated energy transfer should be considered. The energy transfer process may be dominated by excitons and $^3O_2$ converted into $^1O_2$.[156–158] The relevant discussion on two mechanisms based on energy transfer and charge transfer is included in the following section.

3.1.1 Photocatalytic water splitting by exciton dissociated charge transfer mechanism. Guan *et al.*[159] experimentally proved the boosting of H_2 production in a black phosphorus (BP) quantum dot (QD)/TiO$_2$ heterojunction by enhancing the exciton dissociation. The driving force originating from the energy difference between the CBs is the main reason for the dissociation of excitons in the BP/TiO$_2$ heterojunction. The experimental results indicated enhanced catalytic activity for the BP/TiO$_2$ heterojunction (112 µmol g^{-1} h^{-1} H$_2$ evolution), whereas TiO$_2$ demonstrated 47 µmol g^{-1} h^{-1} under full spectrum illumination, as shown in Fig. 11a. Fig. 11b indicates H$_2$ evolution under visible light with a 420 nm cut-off filter, where

the BP/TiO$_2$ heterojunction showed 46 µmol g^{-1} h^{-1}. In the DRS measurement, the BP/TiO$_2$ heterostructure exhibited absorption both in the ultraviolet and visible light regions, whereas bare TiO$_2$ only absorbed in the ultraviolet region, implying lowering of the band gap for BP/TiO$_2$. This suggests the efficient visible light absorption of the heterostructure compared to TiO$_2$ (Fig. 11c).

As shown in Fig. 11d, the TRPL measurement showed that the BP/TiO$_2$ heterojunction has a longer lifetime (3.5 ns) than TiO$_2$ (2.7 ns). This suggests a longer time for the existence of photo-redox carriers together with a greater opportunity for the dissociation of excitons. The current density *vs.* time (I–t) (Fig. 11e) showed a nearly 2.4-times higher current density for BP/TiO$_2$ than the pristine TiO$_2$, indicating a higher concentration of charge carriers and greater charge carrier mobility. Moreover, the electrochemical impedance spectroscopy (EIS) measurement (Fig. 11f) showed a lower charge transfer resistance for the heterostructure, which denotes an enhancement in carrier separation. Fig. 11g displays that the work function of TiO$_2$ is higher than that of the BP QDs, and thus charge transfer may happen from BP to TiO$_2$ after the formation of the heterostructure. The contact angles of TiO$_2$ and BP/TiO$_2$ are 39° and 28°, respectively, which suggest that a decrease in the contact angle enhanced the hydrophilicity of the catalyst, and hence BP/TiO$_2$ can be useful for proton adsorption on its surface (Fig. 11h). Fig. 11i displays the charge transfer mecha-
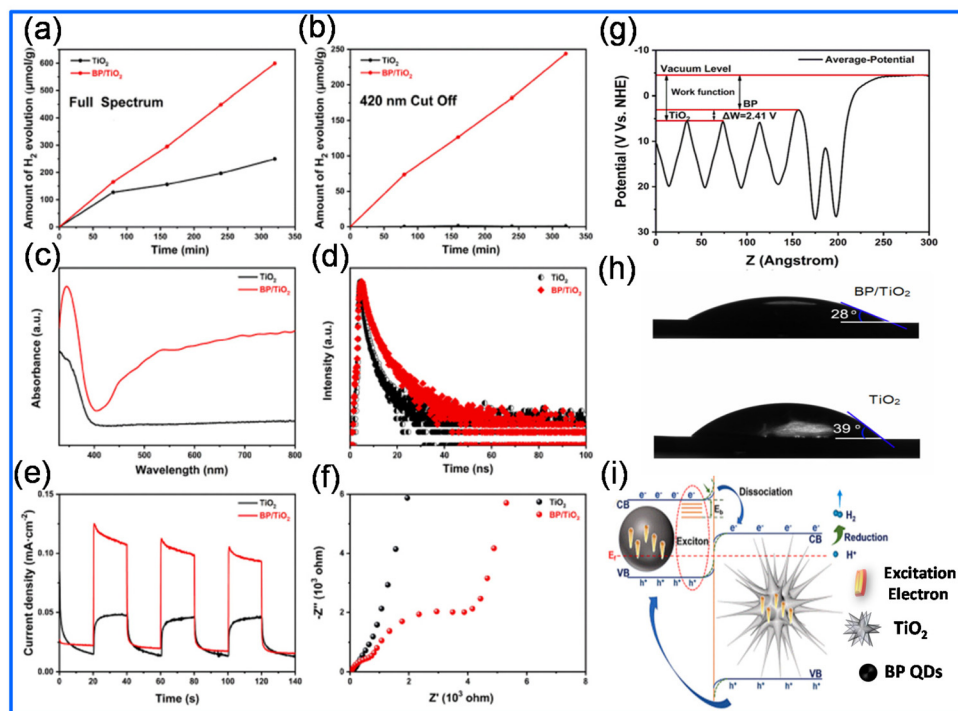

Fig. 11 H$_2$ generation at different reaction times using TiO$_2$ and BP/TiO$_2$ composite as photocatalysts under (a) solar light and (b) visible light (420 nm cut off filter). (c) UV-VIS DRS of TiO$_2$ and BP/TiO$_2$. (d) Fluorescence lifetime of TiO$_2$ and BP/TiO$_2$. (e) Transient photocurrent curves of TiO$_2$ and BP/TiO$_2$. (f) Impedance spectra of TiO$_2$ and BP/TiO$_2$. (g) Work-function of BP/TiO$_2$ composite. (h) Contact angle measurement of TiO$_2$ and BP/TiO$_2$. (i) Mechanistic representation of H$_2$ production on BP/TiO$_2$. Reproduced with permission from ref. 159. Copyright 2022, Elsevier Publishing Group.

nism of the heterostructure. After the formation of the heterojunction, electron transfer may occur from the CB of BP to the CB of TiO₂ due to the low work function of the BP QDs. However, due to the strong coulombic attraction between them, electron–hole excitons may be formed, which also dissociate because of the internal driving force (difference between the work function of the two materials). The internal driving force is higher than the exciton binding energy and allows electron transfer from the CB of BP to the CB of TiO₂. These electrons further participate in the proton reduction reaction for hydrogen evolution. Pan *et al.*[160] proposed that the introduction of triazine-heptazine in polymeric CN (PCN) (also called melon) enhanced the separation of excitons. They compared the catalytic performance of H-CN (heptazine-based melon) and TH-CN with varying amounts of H-CN such as TH-CN-1 (3 g), TH-CN-2 (1.5 g), TH-CN-3 (0.2 g). The EPR measurement (Fig. 12a) showed that TH-CN-2 exhibited the highest intensity peak among the compositions, indicating the maximum concentration of free charge carriers, which makes it suitable for application in photocatalysis. The UV-Vis absorp-

tion spectra (Fig. 12b) showed a slightly red-shift in the intrinsic absorption of TH-CN-2 compared to pristine H-CN, indicating a decrease in the band gap and T-CN (triazine CN). The fluorescence spectra (Fig. 12c) demonstrated a peak at around 455 nm, indicating the recombination of excitons. Fig. 12d shows the time-resolved photoluminescence (TRPL) spectra, where the TH-CN-2 excitons have a shorter lifetime (2.9 ns) than that of H-CN (3.6 ns), implying that the exciton dissociation is much faster in TH-CN-2 than H-CN. EIS (Fig. 12e) showed that the charge transfer resistance is much smaller in the complex than the pristine material, enhancing the charge transfer. Also, a similar trend was obtained in the photocurrent measurement (Fig. 12f) curve, where TH-CN-2 exhibited a much higher current density compared to H-CN at the same applied potential, implying the generation of hot free charge carriers at the triazine-heptazine junction by the built-in electric field. In the temperature-dependent PL spectra (low temperature measurement) (Fig. 12g and h), it can be observed that the exciton binding energy decreases from 64 meV to 48 meV, which suggests an increase in singlet exciton dis-
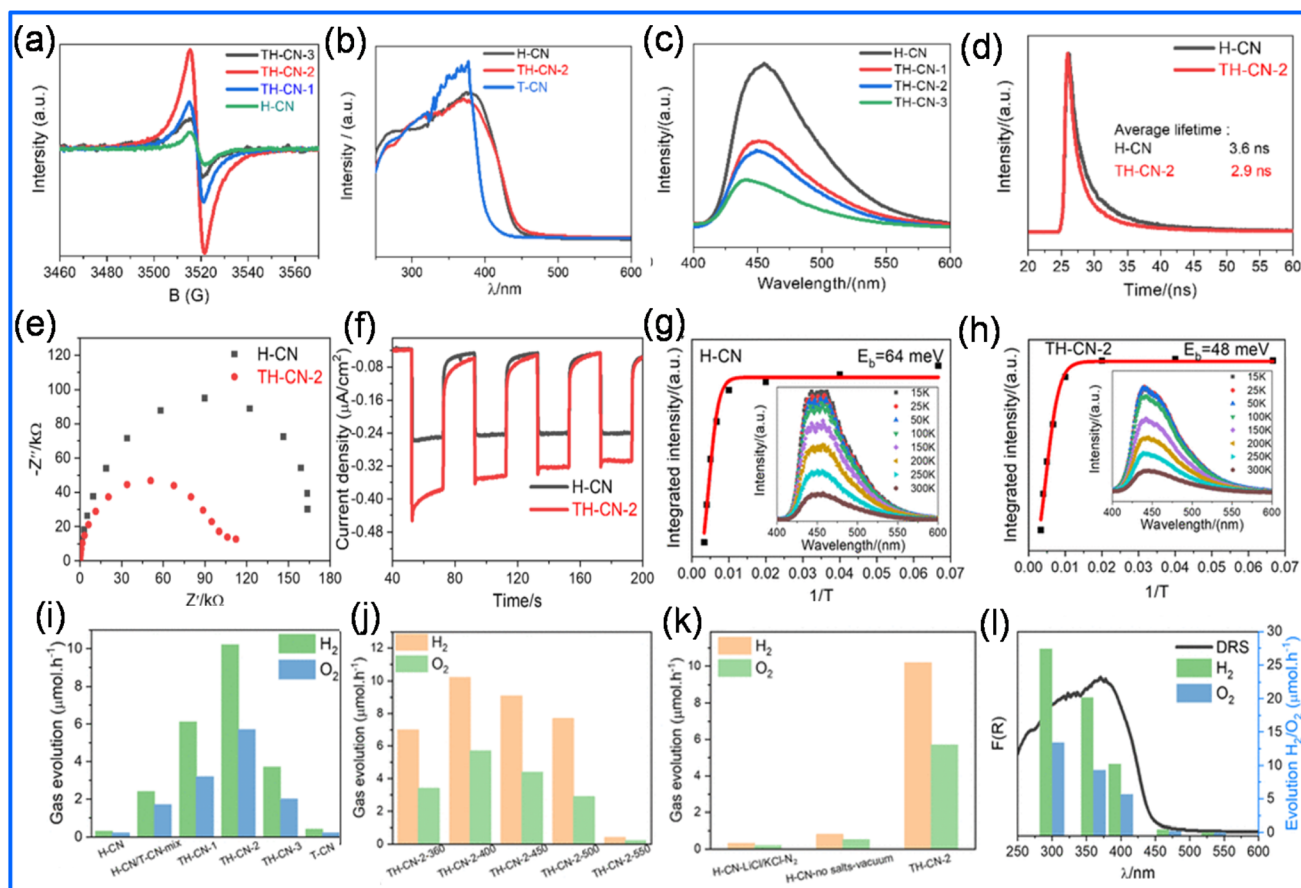

Fig. 12 (a) EPR spectra of T-CN and TH-CN-*x*. (b) UV-Vis optical absorption and (c) PL spectra of H-CN and TH-CN-*x*. (d) TRPL profiles of H-CN and TH-CN-2. (e) EIS of pristine H-CN and TH-CN-2. (f) Transient photocurrent of pristine H-CN and TH-CN-2. PL emission of (g) H-CN and (h) TH-CN-2. (i) Comparison the amount of gas evolved of different samples. (j) Comparison of gas evolution of TH-CN at different salt-melt temperatures varying from 360 °C–550 °C. (k) Photocatalytic overall water splitting rate of H-CN-no salts-vacuum, H-CN-LiCl/KCl-N₂ and TH-CN-2. (l) Wavelength dependence water splitting of TH-CN-2 photocatalyst. Reproduced with permission from ref. 160. Copyright 2021, the American Chemical Society.

sociation into hot free charge carriers. The reduction in the excitonic binding energy can be linked to the H_2 and O_2 evolution performance, where H-CN-2 showed the maximum gas evolution (Fig. 12i) under visible light, which is 34 times higher than that of H-CN. With an increase in the salt-melt temperature from 360 °C–550 °C (Fig. 12j), the gas evolution decreased due to the transformation of the structure from heptazine to triazine. In contrast, the gas evolution significantly decreased in the case of H-CN post-calcined in the absence of salt or vacuum (Fig. 12k). Fig. 12l displays the dual plot of gas evolution of TH-CN-2 at different wavelengths of light and the UV-Vis DRS data. This suggests that with an increase in absorption, the gas evolution also increases due to the maximum number of hot charge carriers generated at a particular wavelength of light irradiation.

It was reported that single atomic S vacancy-induced PEF in Sv-CdS-2 contributed the highest free charge carrier density, charge mobility and high photocurrent. Fig. 13a shows the photocatalytic H_2 evolution measurement, where Sv-CdS-2 has the highest catalytic performance, which is nearly 53-times higher than that of the pristine CdS. Fig. 13b illustrates the gas evolution performance with the vacancy content (%), suggesting that the multi-atomic S vacancies in Sv-CdS-3

produce the minimal amount of H_2 given that they weaken the PEF, which cannot prevent electron–hole recombination. Sv-CdS-2 had a much higher gas evolution rate compared to other semiconductor (such as graphene and MoS_2) heterostructures with CdS, as shown in Fig. 13c. By increasing the incident photonic wavelength, the H_2 evolution rate decreased due to the fast charge recombination rate, which reduced the photoredox charge carrier density (Fig. 13d). Fig. 13e shows that CdS and Sv-CdS-3 do not exhibit any catalytic activity at a wavelength greater than 420 nm due to the fast rate of charge recombination and presence of multiatomic S vacancies. Surprisingly, Sv-CdS-1 and Sv-CdS-2 displayed H_2 and O_2 evolution (efficiency ratio of H_2/O_2 of ∼ 2 : 1) activity, and Sv-CdS-2 with the optimal S vacancy-induced spin PEF showed a much higher overflow efficiency for H_2/O_2.

Liu et al.[161] proposed a donor–acceptor (D–A) interaction-based COF to regulate excitonic effects by dissociation into high lifetime-induced free photo-redox charge carriers. Fig. 14a displays the synthesis of benzobisthiazole-bridged COFs with adjustable D–A interactions through the acid-catalysed Schiff-base reaction between the donor unit Tz (benzo[1,2-b:4,5-d] bisthiazole-2,6-diamine) and the acceptor unit BTA (1,3,5-benzenetricarboxalde-hyde derivatives) benzo-

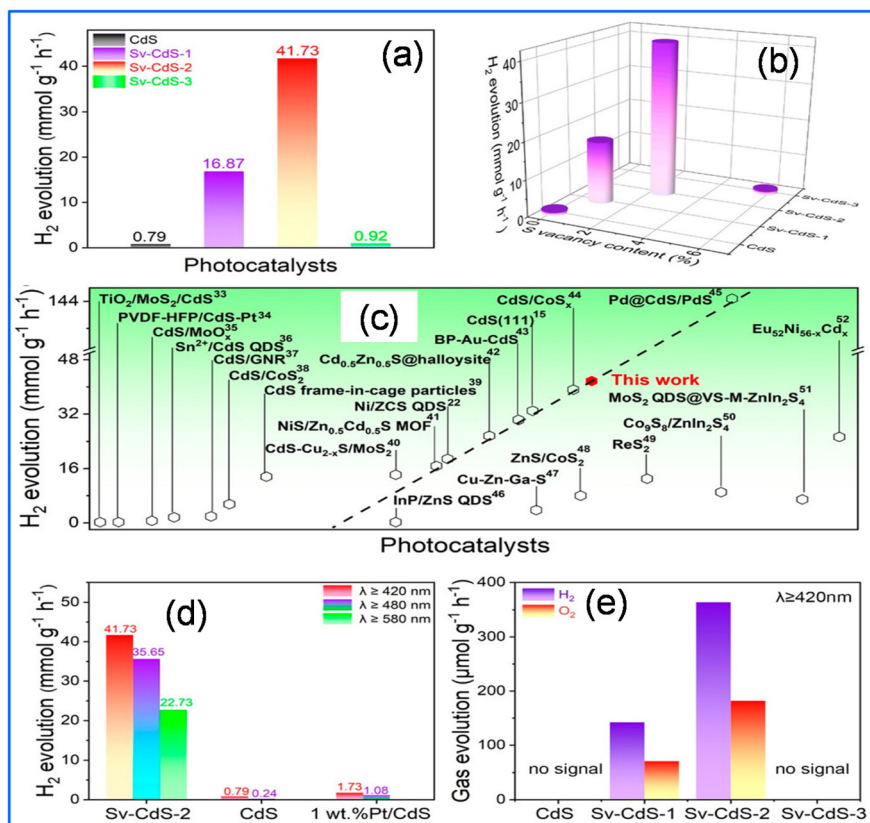**Fig. 13** (a) H_2 generation of CdS and Sv-CdS under visible light irradiation ($\lambda \geq 420$ nm). (b) Correlation between S vacancy concentration and H_2 generation rate. (c) H_2 evolution efficiency comparison under $\lambda \geq 420$ nm irradiation. (d) H_2 generation of CdS, Sv-CdS-2, and 1 wt% Pt/CdS under irradiation at different wavelengths. (e) Overall H_2O splitting efficiency for CdS and Sv-CdS. Reproduced with permission from ref. 113. Copyright 2021, the American Chemical Society.
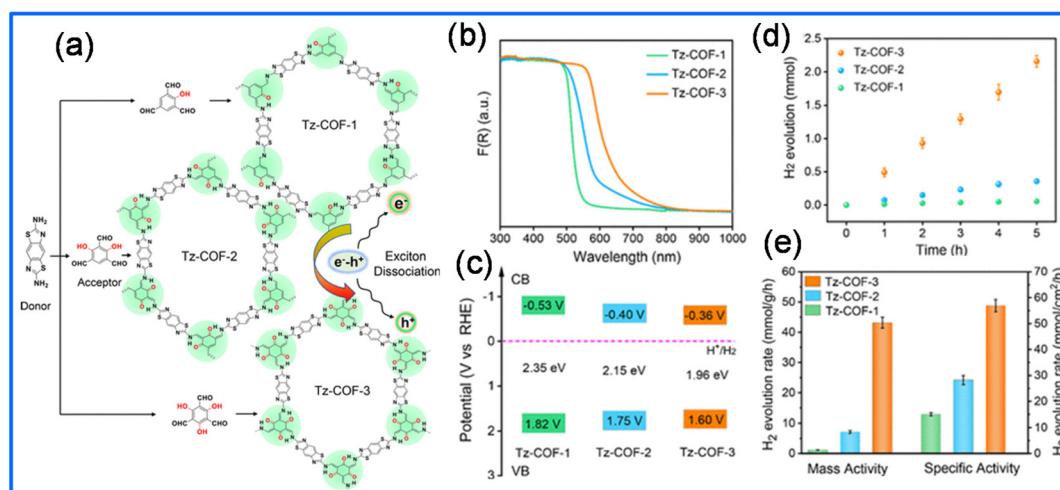
Fig. 14 (a) Synthesis of Tz-COFs with adjustable D–A interactions. (b) UV-Vis DRS spectra of Tz-COFs. (c) Band structure of Tz-COFs. (d) Time-dependent H_2 evolution of Tz-COFs. (e) H_2 evolution rates of Tz-COFs. Reproduced with permission from ref. 161. Copyright 2022, the American Chemical Society.

bisthiazole-bridged COFs. Notably, the increasing number of hydroxyl groups on BTA allow the formation of more ketoenamines with strong electron-accepting ability, which further enhance the D–A interactions. The UV-Vis DRS spectra showed a lower band gap in Tz-COF-3 due to the maximum number of carbonyl groups compared to the other compositions, which enhanced the D–A interaction in the COF, as shown in Fig. 14b. Consequently, the amount of free carriers increased, which further indicates that the magnitude of the flat band potential is lower in Tz-COF-3. The calculated E_C (*vs.* reverse hydrogen electrode) values are −0.53 V, −0.40 V, and −0.36 V for Tz-COF-1, Tz-COF-2, and Tz-COF-3, respectively. Thus, the CB is more negative for all three sample than required for H^+ to generate H_2, indicating that all the samples can be applied for water splitting. A schematic of the band diagram for all the materials is shown in Fig. 14c, confirming that the band gap becomes narrower on going from Tz-COF-1 to Tz-COF-3. Subsequently, the gas evolution rate is the highest in Tz-COF-3, where the H_2 generation linearly increased with time (Fig. 14d). Also, the E_b is the lowest for Tz-COF-3, indicating the higher dissociation of excitons and increase in the drift velocity of photo-redox charge carriers, which further participate in redox reactions. It is evident in Fig. 14e that the H_2 evolution of Tz-COF-3 is nearly 3-times higher than that of Tz-COF-1.

3.1.2 Photocatalytic water splitting by excitonic energy transfer mechanism. Given that excitons also act as dominant photoinduced energy species, the excitonic energy transfer also needs to be considered in low-dimensional semiconductors for photocatalytic activity. Exciton energy transfer is crucial for understanding the quantum efficiency of semiconductors, which can be described *via* two mechanisms, namely, Förster energy transfer (FRET) and Dexter energy transfer.[162–164] FRET is a non-radiative energy transfer process, which enables the long-range hopping of excitons in donor–acceptor systems. Dexter energy transfer involves the transfer of excitons from the donor to acceptor due to the hopping of electrons, which is facilitated by the exchange interaction. The wavefunctions of both the donor and acceptor must overlap in Dexter energy transfer.[165,166] Hence, due to the overlapping electron clouds in the donor and acceptor materials, excitons may diffusively hop from one material to the next without a change in spin. Particularly, Förster energy transfer occurs over a large distance compared to Dexter energy transfer. For example, the typical distance range for FRET is around 100 Å, whereas that for Dexter energy transfer is around 10 Å. All the excitonic energy transfer processes follow the above-mentioned mechanisms to generate reactive oxygen species (ROS) for photocatalytic solar fuel generation. Ding *et al.*[167] investigated singlet oxygen production for molecular oxygen activation by regulating the reaction time of BiOBr. At different solvo-thermal reaction times, different vacancies such as single oxygen vacancies $(V_O^{\bullet\bullet})$, which mainly form at the surface, and double-atom defect cluster $((V_{Bi}''V_O^{\bullet\bullet}))$ and triple-atom defect clusters $(V_{Bi}''V_O^{\bullet\bullet}V_{Bi}''$ and $V_{Br}^\bullet V_{Bi}'''V_O^{\bullet\bullet})$ at the subsurface and bulk of the BiOBr, respectively, as shown in Fig. 15a. To study the effect of defect clusters on the relaxation of excitons, steady-state PH spectra were measured, as displayed in Fig. 15b, indicating the robust formation of triplet excitons in the $V_{Br}^\bullet V_{Bi}'''V_O^{\bullet\bullet}$ cluster-associated BiOBr compare to the $V_{Bi}''V_O^{\bullet\bullet}$ cluster-associated BiOBr. The energy diffidence between the singlet and triplet states (ΔE_{ST}) is measured based on the difference between steady-state PL and phosphorescence (PH), as shown in Fig. 15c, indicating that the $V_{Br}^\bullet V_{Bi}'''V_O^{\bullet\bullet}$ cluster-obtained BiOBr has a smaller energy difference compared to $V_{Bi}'''V_O^{\bullet\bullet}$.

The triplet to singlet molecular oxygen activation is governed by the ISC rate. According to the Franck–Condon principle, the ISC rate between the singlet and triplet excited sates depends on ΔE_{ST} and the spin–orbit coupling (SOC) between the spin–orbit coupling states. Thus, the small ΔE_{ST} and large
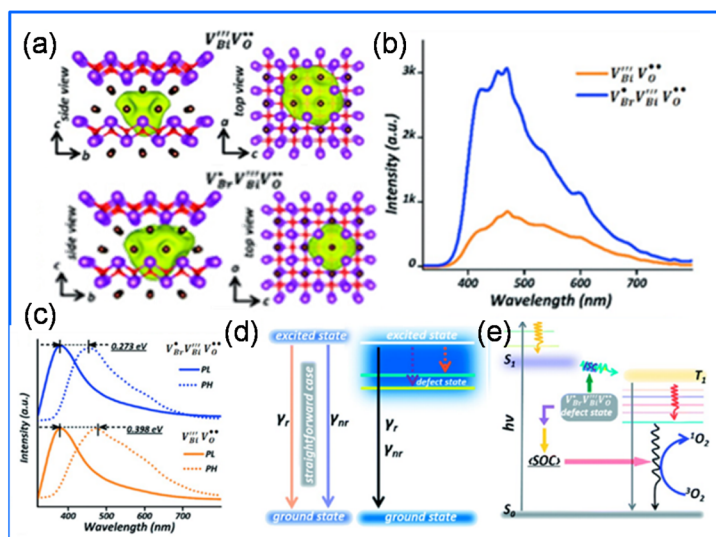
Fig. 15 (a) Positron density distribution in BiOBr with $V'''_{Bi}V^{\bullet\bullet}_O$ and $V^{\bullet}_{Br}V'''_{Bi}V^{\bullet\bullet}_O$ cluster associates. (b) Steady-state phosphorescence spectra. (c) Normalized steady-state PH and PL spectra. (d) Schematic illustration of electronic energy states different defect states. (e) Schematic diagram of singlet O_2 generation in BiOBr. Reproduced with permission from ref. 167. Copyright 2017, The Royal Society of Chemistry.

SOC of the $V^{\bullet}_{Br}V'''_{Bi}V^{\bullet\bullet}_O$ cluster-containing BiOBr promoted the ISC process, which enhanced the generation of singlet molecular oxygen ($^3O_2 \rightarrow {}^1O_2$), as illustrated in Fig. 15e.[168] Wang *et al.*[169] investigated the photocatalytic H_2 evolution through the generation of $^1O_2$ in g-C_3N_4. The H_2 evolution rate sharply decreased from 6.7 μmol h^{-1} to 0.4 μmol h^{-1} due to the addition of 2-bromoethanol to g-C_3N_4 (Fig. 16a).

Electron spin resonance (ESR) measurement for both ethanol and 2-bromoethanol in the presence of 5,5-dimethyl-1-pyrroline-N-oxide was performed (DMPO, as a trapping agent of superoxide radicals, $^{\bullet}O_2{}^-$), where the signal corresponding to the generation of DMPO-OOH suggests the production of $^{\bullet}O_2{}^-$, as shown in Fig. 16b. The ESR signal showed the typical 1 : 1 : 1 triplet using a mixture of 2,2,6,6-tetramethylpiperidine
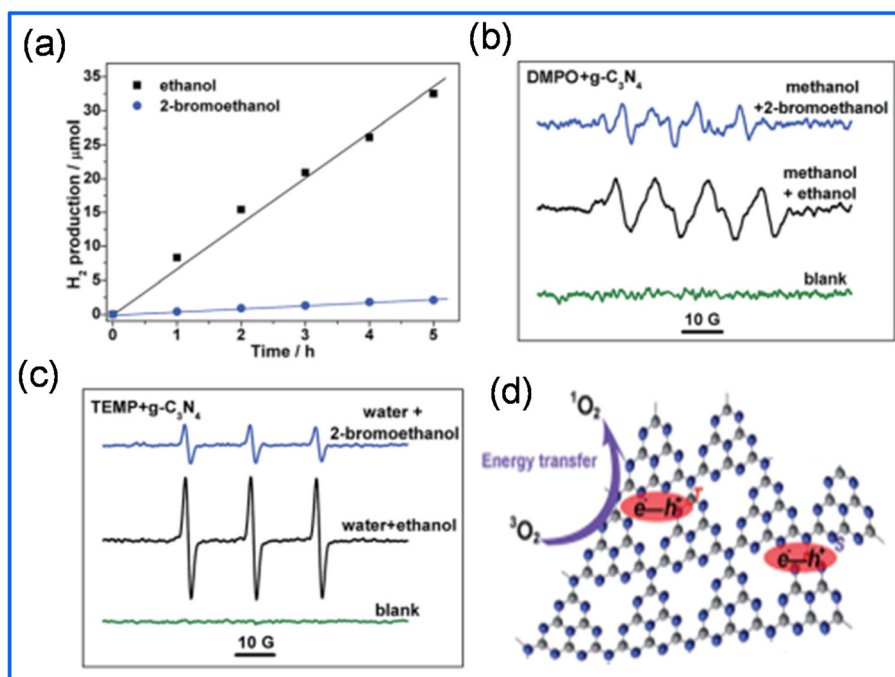

Fig. 16 (a) Photocatalytic H_2 generation on g-C_3N_4. (b) DMPO and (c) TEMP superoxide radical-trapped ESR spectra of g-C_3N_4 in different solutions. (d) Schematic representation of energy and charge transfer mechanism for photocatalysis application. Reproduced with permission from ref. 169. Copyright 2017, The Royal Society of Chemistry.

(TEMP) and g-C$_3$N$_4$ (Fig. 16c). This confirmed the generation of ^{1}O$_2$ molecules in the photocatalytic process. The photocatalytic performance in the presence of 2-bromoethanol suggested the formation of triplet–triplet annihilation, which consumed the excitons (Fig. 16d). Yu et al.[170] investigated the boosted generation of ROS by modulating the excitonic effect in COFs for photocatalysis. Porphyrinic COFs, mainly DhaTph, have a strong excitonic effect due to their low dielectric constant, where ^{1}O$_2$ can be generated via energy transfer from the triplet excited state to ground sate triplet oxygen species. After the modification of a COF with a metal organic framework (MOF), specially NH$_2$-MIL-125, the photocatalytic activity improved due to the free charge carrier generation from exciton dissociation. Fig. 17a shows the schematic mechanism for the generation of ^{1}O$_2$ in DhaTph via a photoinduced excitonic charge transfer process. Prompt fluorescence (PF) measurement of both DhaTph and M@DhaTph showed that the PF intensity of M@DhaTph is lower than that of DhaTph (Fig. 17b). This indicates low charge carrier recombination in M@DhaTph and high radiative decay of singlet excitons in the DhaTph system. Fig. 17c and d show that the PF intensity in DhaTph and M@DhaTph at 77K is higher than that at 298K due to the high decay of concentrated singlet excitons. This is

attributed to the additional energy received by the excitons from the reduced phonon vibration. The phosphorescence indicates the generation of triplet excitons in the triplet energy state and the decrease in PH intensity in M@DhaTph compared to DhaTph defines the reduced concentration of triplet excitons and their decay into free charge carriers, as illustrated in Fig. 17e. To observe the generation of ^{1}O$_2$, ESR spectroscopy measurement was useful (Fig. 17f and g). The ESR spectrum showed the typical 1 : 1 : 1 triple signal in the presence of the trapping agent 2,2,6,6-tetramethylpiperidine (TEMP), which indicates the production of ^{1}O$_2$ in both DhaTph and M@DhaTph. Specifically, the slight decrease in the peak intensity for M@DhaTph compared to DhaTph suggests that the production of ^{1}O$_2$ was suppressed owing to the dissociation of excitons. In the presence of DMPO as a scavenger of ROS ($^•$O$_2^-$ and $^•$OH), M@DhaTph demonstrated the typical ESR signal of DMPO; however, DhaTph had a weak signal, indicating the negligible amount of free charge carriers. Hence, ^{1}O$_2$ was formed in DhaTph via the excitonic energy transfer process and a Z-scheme heterostructure was formed for M@DhaTph (Fig. 17h).

Wang et al.[171] investigated excitons in the triple excited state of g-C$_3$N$_4$ (pristine CN). Remarkably, pristine CN and its
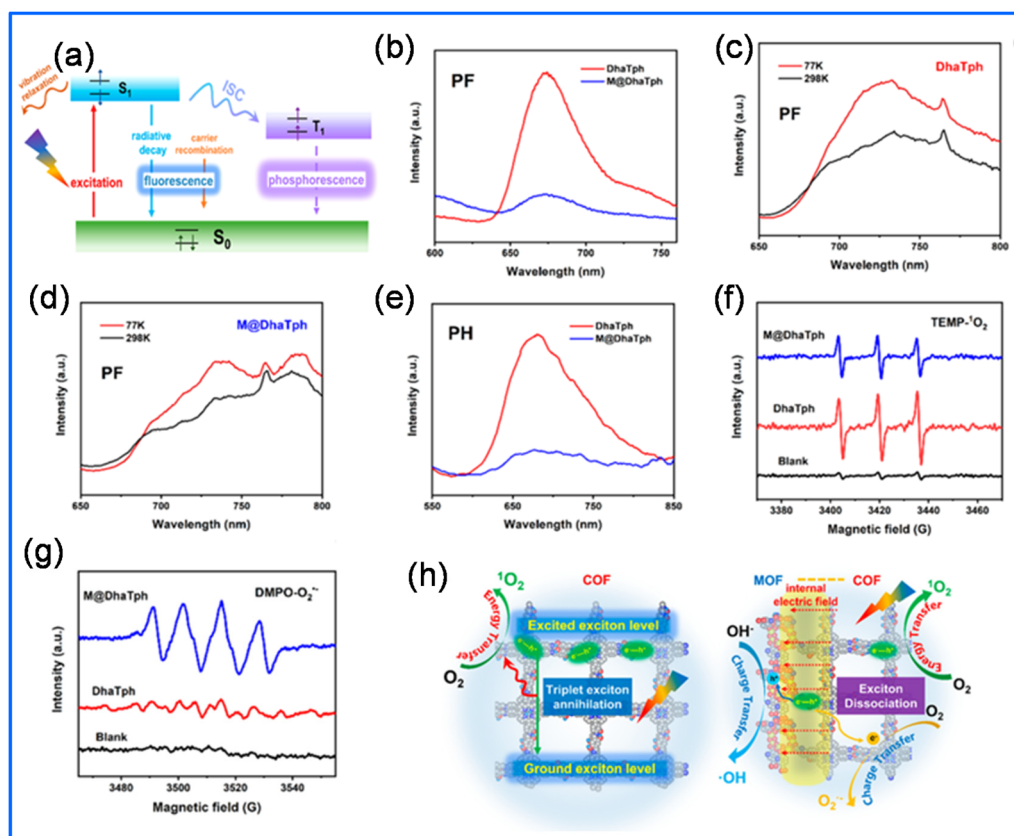

Fig. 17 (a) Representation of the typical excitonic processes in DhaTph. (b) PL spectra at 298 K for DhaTph and M@DhaTph. Temperature-dependent PL of (c) DhaTph and (d) M@DhaTph. (e) Phosphorescence spectra at 77 K of DhaTph and M@DhaTph. ESR spectra of M@DhaTph and DhaTph in the presence of (f) TEMP and (g) DMPO. (h) Schematic diagram of the energy transfer and charge transfer processes in COFs and MOF@COF. Reproduced with permission from ref. 170. Copyright 2022, the American Chemical Society.

derivatives showed excitonic energy transfer between the exciton triplet state and exciton ground state for generating $^1O_2$. Triple-excitons may significantly increase when carbonyl groups are incorporated in the CN matrix (called oxidized g-C_3N_4 or CNO) by oxidization treatment, which obviously enhanced the generation of $^1O_2$, enhancing the photocatalytic performance. The existence of triplet excitons in CNO compared to pristine CN was studied through PH spectra, which showed the greater generation of $^1O_2$ in CNO than the pristine material. Notably, the ΔE_{ST} was lower for CNO compared to pristine CN and the spin–orbit coupling was higher in CNO. This indicates that the ISC rate is higher in CNO, which favours $^1O_2$ generation.

3.2 CO_2 reduction

Recently, excitonic effects have been considered to be a crucial parameter for identifying promising photocatalytic materials for CO_2 reduction and valuable-added products.[172] To reduce the recombination of charge carriers in semiconductors and improve the utilization of electrons for CO_2 reduction, similar strategies have been proposed, including the formation and disassociation of excitons, exciton regulation *via* vacancies and construction of heterojunctions. Ma *et al.*[173] explored the role of oxygen vacancies in layered bismuth oxychloride nanosheets (BOC-OV) to overcome the effect of the excitonic process, which lowers the catalytic CO_2 conversion reactions. Conceptually, oxygen vacancies can capture excited electrons instead of their recombination with holes, which lowers the recombination rate of charge carriers. Consequently, the dissociation of excitons resulted in the superior CO_2 conversion efficiency of BOC-OV under light irradiation. The transient photocurrent of BOC-OV demonstrated a high current density, which suggests that the oxygen vacancies mediated exciton dis-

sociation to generate more photo-induced electrons, as shown in Fig. 18a. The smaller diameter of the semicircle arc of BOC-OV compared to BOC also indicates a lower electron transfer resistance value and the photo-induced charge separation may improve by the oxygen vacancies (Fig. 18b). Fig. 18c shows the radiative lifetimes of about 2.06 and 1.34 ns for BOC-OV and BOC, respectively. The decrease in PL lifetime can be related to the acceleration of the nonradiative intersystem crossing process, which suggests more effective conversion from singlet into triplet excitons.[24,26] Hence, the increased lifetime (about 54% increase) of BOC-OV suggests enhanced exciton dissociation in BOC-OV. A similar trend was observed in the catalytic performance, where 35.03 and 14.78 mmol g^{-1} of CO were generated using BOC-OV and BOC, respectively, under UV-Vis light irradiation, as shown in Fig. 18d. Alternatively, a relatively lower amount of 8.66 and 2.33 mmol g^{-1} CO was evolved over BOCOV and BOC, respectively, under visible light irradiation. The valence band XPS spectra (Fig. 18e) showed a higher VB position for BOC-OV. Based on the same energy gap (3.33 eV) of BOC-OV and BOC, BOC-OV (1.58 V) has a higher CB position than BOC (0.98 V), which supports its improved photocatalytic reduction ability (Fig. 18f). Based on *in situ* FTIR measurement and DFT calculation, the CO_2 reduction pathways to CO and CH_4 were proposed with six elemental hydrogenation steps, as shown in Fig. 18g. Interestingly, the hydrogenation of CH_2OH^* was identified as the rate-determining step of the CH_4^* generation path using BOC-OV as the photocatalyst. The DFT calculation suggested a lower barrier (0.46 eV) for the formation of CO^* on BOC-OV than BOC (2.46 eV).

In another example, Li *et al.*[174] reported that nitrogen vacancies facilitate the dissociation of excitons into free charges, and the electron concentration in Nv-rich-CN
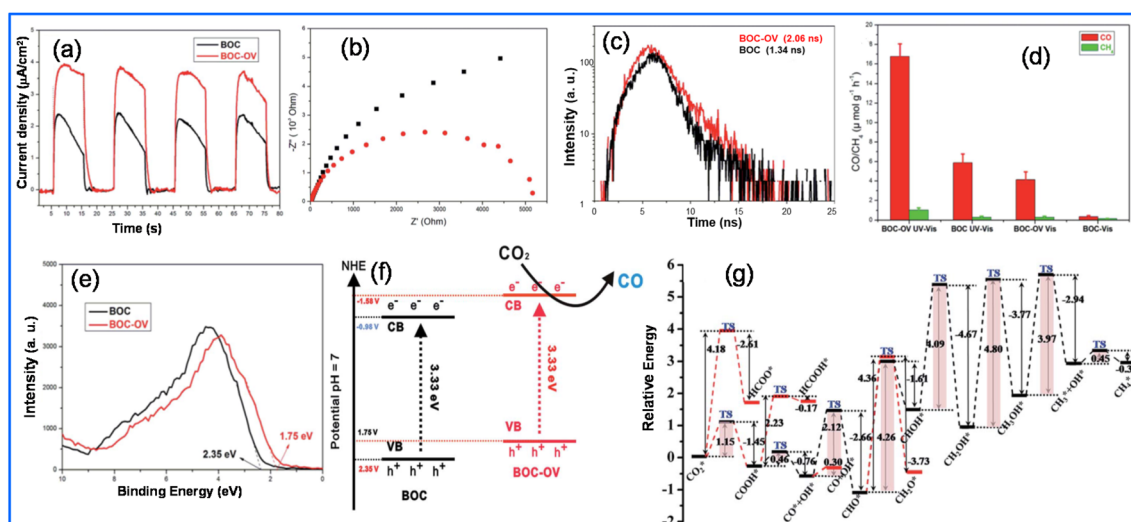

Fig. 18 (a) Transient photocurrent response, (b) electrochemical impedance spectra, (c) time-resolved PL spectra and (d) rate of CO and CH_4 generation under light irradiation using BOC-OV and BOC as photocatalysts. (e) Valence band XPS spectra of BOC-OV and BOC. (f) Band energy diagram of BOC-OV and BOC. (f) Reaction pathways for CO_2 reduction to CH_4 on BOC-OV. "*" represents adsorption on the substrate. The red route is the alternative pathway. Reproduced with permission from ref. 173. Copyright 2017, The Royal Society of Chemistry.

increased by ~3 times compared to pristine g-C$_3$N$_4$ (CN) (Fig. 19a). Nv-rich-CN showed enhanced activity for CO$_2$ photoreduction, with a higher CO and CH$_4$ evolution rate (6.61 and 0.20 μmol h^{-1} g^{-1}) than that of pristine CN (2.89 μmol h^{-1} g^{-1} and 0.07 μmol h^{-1} g^{-1}), as shown in Fig. 19b and c, respectively. The reduction in the PL intensity suggests that the concentration of singlet excitons is reduced in Nv-rich-CN, and hence the number of vacancies may be directly proportional to the degree of exciton dissociation (Fig. 19d). A similar trend was also observed in the time-resolved PL spectra (inset of Fig. 19d) of Nv-rich-CN, where the lifetime of the singlet excitons is the lowest, which indicates that N vacancies promote the dissociation of excitons. The positive slope in the Mott–Schottky curves of all the materials suggests n-type semiconductor behaviour; however, the more negative flat-band potential of Nv-rich-CN supports stronger CO$_2$ reduction ability (Fig. 19e). The presence of $^1O_2$ in the ESR spectra of Nv-rich-CN was confirmed using TEMP as a trapping agent, showing a 1 : 1 : 1 triplet signal, whereas the triplet signal of ESR was profoundly reduced in the presence of NaN$_3$ scavenger (Fig. 19f). It was proposed that the triplet excitons in the photocatalyst transfer energy to the ground-state oxygen molecules, which produce singlet oxygen ($^1O_2$), also validating the presence of excitons and promoted exciton dissociation. Moreover, DFT calculation suggested that N vacancies act as active sites for CO$_2$ reduction, promoting the adsorption and activation of CO$_2$ by the photocatalyst. This suggests the huge significance of the modulation of excitons in semiconductors, which improves the utilization of charge carriers for photocatalysis. Yang et al.[175] highlights role of vacancies to modulate the electronic structure for designing efficient photocatalysts through DFT calculation. The CO generation efficiency achieved a 10-fold enhancement using O-modified orange polymeric carbon nitrogen as the photocatalyst. The charge
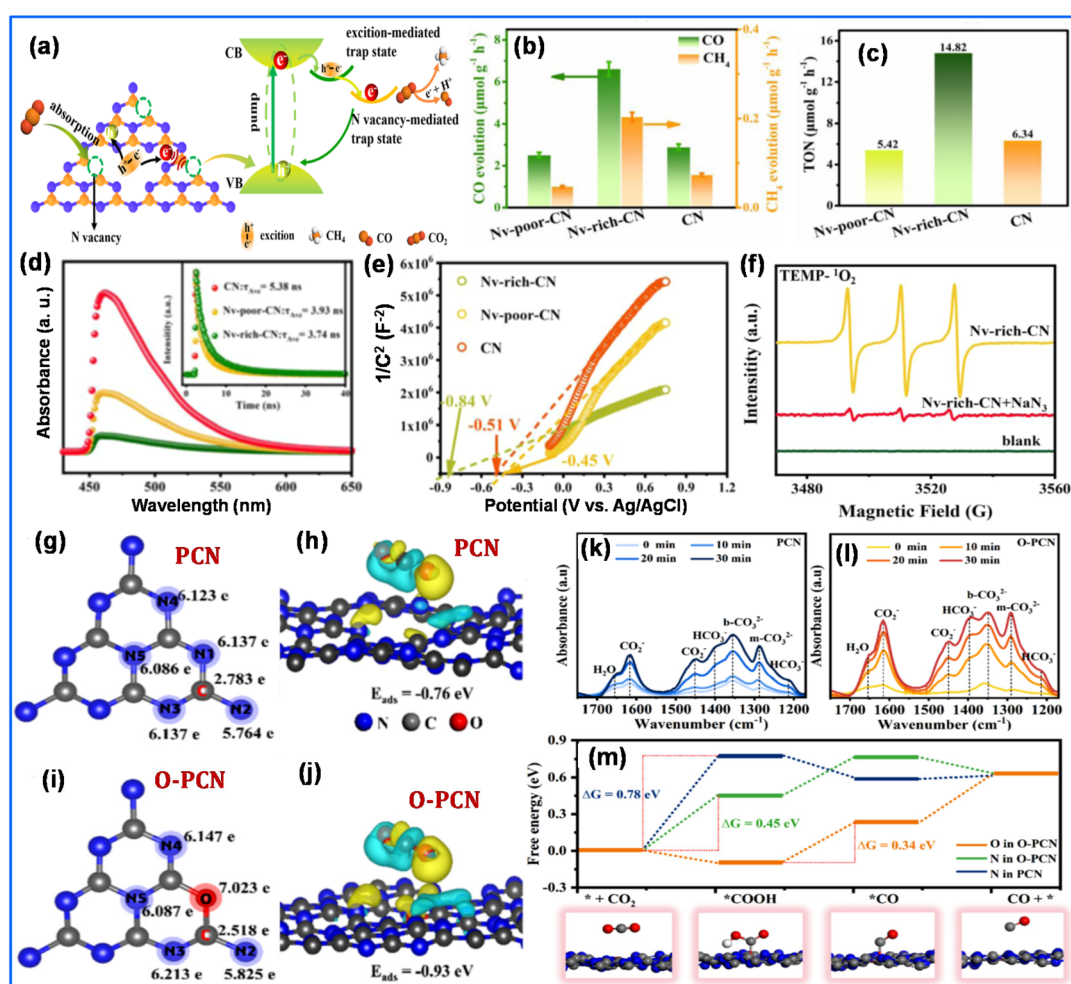

Fig. 19 (a) Schematic representation of CO$_2$ reduction on Nv-rich-CN surface. (b) Evolution rate of CO and CH$_4$. (c) Turnover numbers of CO generation for Nv-rich-CN, Nv-poor-CN, and CN. (d) PL of Nv-rich-CN, Nv-poor-CN, and CN. Inset: TRPL spectra, (e) Mott–Schottky plots, and (f) ESR spectra of the materials. Reproduced with permission from ref. 174. Copyright 2021, Elsevier Publishing Group. (g and h) Calculated Bader charge, (i and j) charge difference density distribution and (k and l) in situ FTIR spectra of PCN and O-PCN, respectively. (m) Free energy diagram of photocatalytic CO$_2$ reduction and intermediate adsorption model of O-PCN. Reproduced with permission from ref. 175. Copyright 2023, Elsevier Publishing Group.

distribution values of the control PCN and O-PCN were compared through the Bader charge, as shown in Fig. 19g–j. Remarkably, the O atom accumulates a high electron density at N1 7.023 eV compared to PCN (6.137 eV) and a similar trend was observed for the electron density of N2, N3 and N4, suggesting the stronger charge transfer behaviour of O-PCN. They followed the CO_2 photoreduction pathway of PCN and O-PCN using *in situ* Fourier transform infrared spectroscopy with solar illumination, as demonstrated in Fig. 19k and l, respectively. The experimental data suggested that both catalysts follow a similar reaction pathway; however, with an increase in time, the evolution of intermediate species increased for O-PCN due the high reaction rate. The possible pathways of CO generation are as follows (eqn (12)–(15)):

$$* + CO_2 \rightarrow *CO_2 \tag{12}$$

$$*CO_2 + H^+ + e^- \rightarrow *COOH \tag{13}$$

$$*COOH + H^+ + e^- \rightarrow *CO + H_2O \tag{14}$$

$$*CO \rightarrow CO \uparrow + * \tag{15}$$

The free energy diagram for photocatalytic CO_2 reduction is shown in Fig. 19m. DFT calculation indicated that the O atoms act as the dominant active sites and reduce the free energy of the rate-determining step.

Recently, Zhang and co-workers[175] reported a new approach using boron (B) doping to concurrently engineer the bulk and surface structures of 2D BiOCl photocatalysts for photocatalytic CO_2 reduction. They used the molten B_2O_3 doping strategy, where B_2O_3 is expanded by homogeneous B doping both from the surface into the bulk with dual functionalities. DFT calculation showed that surface-doped B may reconstruct the atomic BiOCl surfaces, resulting in B-oxygen vacancy (B-OV) associates (Fig. 20a). Fig. 20b illustrates that the low concentration of defects in the surface atom arrangement of BiOCl-OV was relatively ordered, whereas surface distortion was observed on BiOCl-B-OV due to the light element B on the annular bright-field (ABF)-STEM images (Fig. 20c). The density of states (DOS) calculations indicated that the B-OV associated with the BiOCl-(001) surface introduced a donor level above the VB maximum and a localized state below the CB minimum, which further lowered the band gap and induced electronic interactions due to the hybridization of the Bi 6p orbital around the OV and neighbouring B 2p orbital (Fig. 20d). Notably, BiOCl-B-OV revealed a significantly high and selective catalytic performance for CO production, which is 4.2- and 28.6-times higher than that of BiOCl-OV and B-BiOCl, respectively (Fig. 20e). It is important to note that in the present system, water can efficiently act as a sacrificial electron donor of holes, which is supported by the close value of experimental CO/O_2 yield (1.92 : 1) with the theoretical yield (2 : 1) based on $2CO_2 \rightarrow 2CO + O_2$ (Fig. 20f). Compared to discrete OV, which can be easily deactivated, this vacancy associate exhibits ultra-high stability for practical long-term application (>120 h) and an impressive CO_2-to-CO conversion rate of 83.64 μmol g^{-1} h^{-1} with selectivity of over 98% (Fig. 20g and h). Based on the experimental and theoretical study, bulk B doping eases strong excitonic effects confined in 2D BiOCl by reducing the binding energy (E_b) of excitons, which in turn accelerates the dissociation of bulk excitons into free charge carriers for CO_2 reduction.

Moreover, Singh *et al.*[176] employed a first-principles computation-based screening strategy for highly selective photocatalysts and 52 materials were shortlisted based on their thermo-
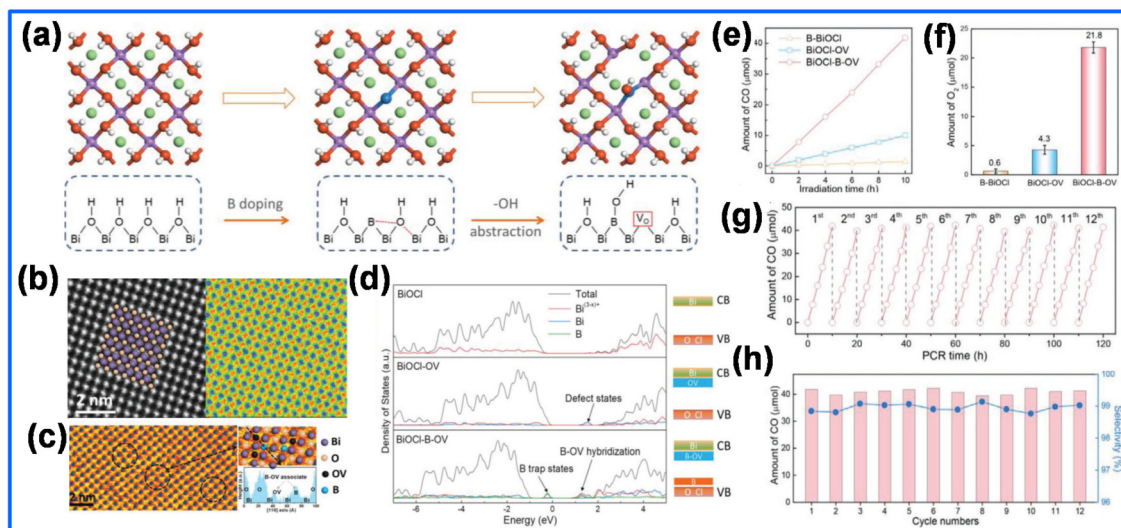

Fig. 20 (a) Structure evolution of BiOCl surface toward the formation of B-OV associate. (b) Atomic-resolution (high-angle annular dark-field scanning transmission electron microscopy) HAADF-STEM image of BiOCl-OV and the corresponding rainbow-colored scale image. (c) ABF-STEM image of BiOCl-B-OV. (d) Calculated DOS of BiOCl, BiOCl-OV, and BiOCl-B-OV. (e) Dynamic CO generation over BiOCl-B-OV surface. (f) O_2 yield during the photocatalytic CO_2 reduction within 10 h. (g) Cycling tests of photocatalytic CO_2 reduction performance over BiOCl-B-OV for 120 h. (h) Selectivity of CO production. Reproduced with permission from ref. 132. Copyright 2021, Wiley Publishing Group.

dynamic and electrochemical stability and electronic structure compatibility for the CO_2 reduction reaction. Singh *et al.*[52] further considered the excitonic effects of several photocatalysts including those comprised of oxides, sulphides, tellurides, *etc.* for CO_2 reduction based on many-body perturbation theory in GW approximation together with Bethe–Salpeter–formalism (BSE).[177–179]

3.3 N_2 fixation

Photocatalytic nitrogen fixation (PNF) involves three steps, as follows: (i) photoexcitation from the valence band to the conduction band, while generating holes in the valence band when the incident light energy is higher than or equal to the forbidden band range of the semiconductor ($h\nu > E_g$); (ii) subsequently, a fraction of the photogenerated electrons and holes migrates to the surface of the semiconductor and recombines at both the surface and in the bulk phase; and (iii) alternatively, other separated electrons and holes migrate to the catalytic sites to participate in the redox reaction. The adsorbed species on the surface of the catalyst undergo a reduction reaction using the photogenerated electrons and an oxidation reaction using the photogenerated holes. Following a sequence of steps, N_2 is reduced to NH_3 by the proton-coupled electron transfer (Scheme 3). With water and nitrogen serving as the starting components, photocatalytic nitrogen fixation can generate ammonia by oxidizing photogenerated holes (eqn (16) and (17)), as follows:

$$6H_2O + 12h^+ \rightarrow 12H^+ + 3O_2 \qquad (16)$$

$$2N_2 + 12H^+ + 12e^- \, 4NH_3 \qquad (17)$$
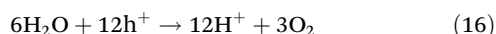
Thus, for the redox reaction to happen, the reduction and oxidation potential of the NRR and water should lie between the CB and VB of the photocatalyst.[180] There are three major considerations in design of photocatalysts from an energetics point of view, as follows: (a) the semiconductor should be able to harvest light efficiently; (b) dissociation of bound electron–hole pairs (excitons) and transfer of excitons should be efficient; and (c) the energy levels of the semiconductor photocatalyst should meet the redox potential of the photo-induced half reactions, referring to the reduction of N_2 and the oxidation of H_2 or H_2O. One of the major factors that govern the overall efficiency of the PNF is the efficacy of separation of excitons and kinetics, in addition to the activation of N_2. The quantum yield of both the exciton- and carrier-triggered photocatalytic processes is strongly influenced by excitonic effects. A promising path towards the creation of enhanced photocatalysts has emerged in recent years with the advancement of nanomaterials and nanotechnology. When discussing photocatalytic nitrogen fixation processes, it is necessary to consider the objective existence of excitonic effects in semiconductors. The performance of PNF systems is substantially hindered by the easy recombination of photo-induced carriers and the lack of active sites.

Some precursor modification methods need to be considered. To optimize this, a variety of approaches are being exploited including the formation of heterojunctions, Schottky junctions, and p–n junctions;[181–183] the development of novel semiconductor materials that expose several crystal planes and permit electron–hole-directed migration to the surface[184–186] and lowering the energy barrier for surface reactions to accelerate the generation of NH_3.[187] Before presenting the strategies for catalyst design, here we briefly explain the two major reaction mechanisms for N_2 fixation, where is the dissociation mechanism and other the association mechanism, depending on whether the N≡N bond is broken before hydrogenation. N_2 is end-on adsorbed on the catalyst surface during the association mechanism. With the hydrogenation of the N atom and the release of the initial NH_3, the N≡N bond gradually breaks. Two types of associative mechanisms are involved, namely,
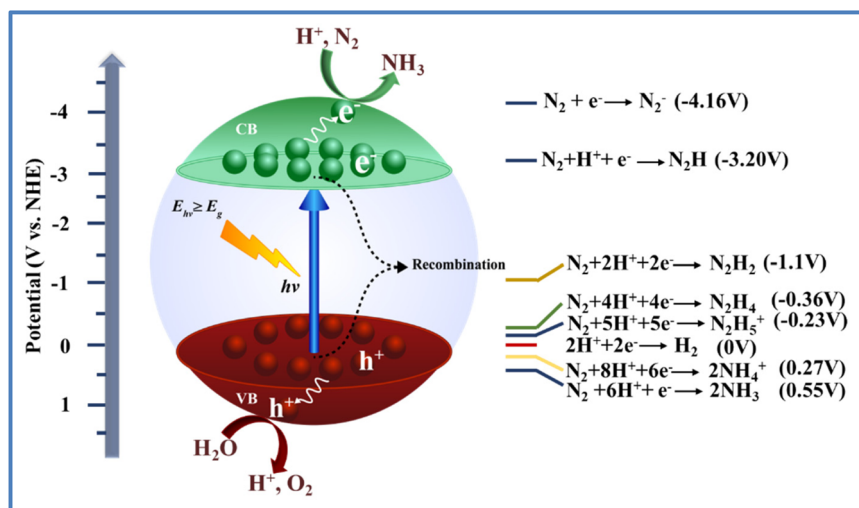
Scheme 3 Schematic representation of overall photocatalytic N_2 reduction to NH_3 over semiconductor-based photocatalyst with energy diagram for N_2 reduction.

associative distal mechanism and associative alternating mechanism, depending on the various sequences of hydrogenation in the direction of the N atom. In contrast to the association process, the enzymatic mechanism involves a side-on mode of firmly adsorbed N_2 on nitrogenases and certain catalysts, followed by an alternative method of hydrogenation.[188] Recent theoretical calculations examined several novel mechanisms, including the Mars-van Krevelen (MvK) mechanism[189] and the surface hydrogenation mechanism.[190] The former is further supported by an [15]N_2 isotope labelling experiment.[191] Since the ground-breaking study by Schrauzer *et al.* in 1977,[192] efforts have been made to design catalysts and modify them to improve the overall efficiency of PNF. Nonetheless, its overall efficiency is limited due to several challenges, which need to be addressed synergistically, including inadequate N_2 adsorption and activation, generation of bound electron hole pairs (excitons) and their poor separation efficacy and competitive side reactions including the HER. The various strategies that are being adopted to address these aspects are discussed below.

3.3.1 Defect engineering. Defects can be divided into four categories depending on their dimensions including zero-dimensional (0D) point defects (such as doping and vacancies), one-dimensional (1D) line defects (such as edge dislocations and screw dislocations), two-dimensional (2D) planar defects (such as grain boundaries and twin boundaries), and three-dimensional (3D) volume defects (*e.g.*, void and lattice disorder).[129,193,194] High-dimensional defects and 1D defects are rarely discussed topics in photocatalytic nitrogen reduction. It has been observed that 0D point defects, such as vacancies and impurities, tend to improve nitrogen reduction. These defects can further be divided into surface/interface, subsurface, and bulk categories based on where they are located.[196,197] According to recent findings,[197,198] bulk defects can serve as recombination sites for excitons, which can be detrimental to photocatalytic activity. Alternatively, surface defects may provide new active sites for the dissociation of photogenerated excitons on the adsorbate, increasing the carrier separation and promoting the adsorption of small molecules on the photocatalyst.[199] The introduction of surface defects and bulk defects creates electrical and spatial synergy. This helps to separate electrons and holes in the bulk and effectively lowers the conduction band edge, acting as an electron capture centre.[200] It has been discovered that subsurface oxygen vacancies improve the conductivity and electron transport of TiO_2, which is advantageous for photocatalytic activity.[201,202] The defects can be categorised into oxygen (OVs), nitrogen (NVs), sulphur (SVs), carbon (CVs), fluorine (FVs), and other elemental vacancies depending on the elements involved. Additionally, single-atom catalysts are also regarded as flaws starting from a larger definition.[203,204] The nature and location of a defect may determine whether it has positive or negative effects, as briefly mentioned above. A defect that is advantageous in one material may be detrimental in another, which makes it challenging to develop generic applicable design guidelines for photocatalysis. To date, the

following fundamental guidelines have been established: (i) the excitons trapped in the bulk cannot participate in the catalytic process, and thus surface defects are typically desirable than bulk defects when they are envisioned to act as trap states;[198,199] (ii) the bound electron–hole pairs at the defects site must possess enough oxidation or reduction potential to facilitate the target reaction; therefore, shallow traps are typically preferred over deep traps, and (iii) to generate enough oxidation or reduction potential to enable the intended reaction to occur, catalytic active sites usually require defects.[205]

3.3.1.1 Oxygen vacancies. Oxygen vacancies (OVs) are the most common anion vacancies in transition-metal oxides due to their low formation energy. Their physicochemical characteristics may be greatly influenced by the presence of OVs. Thus, the concentration of oxygen defects can be used to modify the surface electrical characteristics and band gap states of metal oxides.[206] The performance of the PNF can be improved by Ovs, which have an impact on the adsorption and activation of inert N_2 gas molecules. OVs have received considerable attention in the fields of electrocatalytic and photocatalytic reactions, where they demonstrate great promise for modifying the activities of different catalytic processes. Bastia *et al.*[195] synthesized ultra-small metal nanocrystal-modified $NiTiO_3$ nanocubes, which possessed Ovs, as confirmed by the XPS analysis. The synergistic effects of OVs and the formed heterointerface led to 5-fold enhancement in ammonia yield rate (~14.28 µg h^{-1} mg^{-1} at −0.003 V *vs.* RHE), a faradaic efficiency of 27% (at 0.097 V *vs.* RHE) compared to that for bare $NiTiO_3$ (3.08 µg h^{-1} mg^{-1}), and 9-fold higher activity than that shown by the commercial TiO_2 (P_{25}) (1.52 µg h^{-1} mg^{-1}).[207–209] Yang *et al.*[210] successfully synthesized $WO_{3−x}$ nanosheets *via* the solvothermal method with rich oxygen vacancies, which act as active sites for the chemisorption of N_2 molecules. The OVs induced a defect state, broadened the visible light harvesting, and accelerated the dissociation and transport of excitons for the proficient activation of chemisorbed N_2. Different modulation techniques of generating free charge carriers from excitons for photocatalytic N2reduction have been tabulated and represented in Table 3. The $WO_{3−x}$ nanosheets rich in OVs displayed improved photocatalytic activity (nearly 3.59-times higher) for N_2 reduction to ammonia (82.41 µmol g_{cat}^{-1} h^{-1}) under visible light irradiation (420 nm) than that of the $WO_{3−x}$ nanoparticles having poor OVs.[206] OVs having rich localized-electrons have been shown to serve as electron trapping centres, which can effectively adsorb and activate inert gas molecules (O_2, CO_2, and N_2, in particular). OV modulation holds great promise to improve the photocatalytic activity of materials for efficient nitrogen fixation under mild conditions. Zhang *et al.*[211] prepared $Bi_2Sn_2O_7$ quantum dots *via* a one-step solvothermal method to tune the active sites on the surface and energy band structure. Consequently, enhanced charge migration and optimized molecular nitrogen activation were achieved in the $Bi_2Sn_2O_7$ QDs due to the quantum size effect and electron back-donation mechanism of surface OVs, triggering excellent PNF activity (334.8 µmol g^{-1} h^{-1}), 12-times higher than that

Table 3 Summary of the separation of excitons by different modification strategies for photocatalytic nitrogen reduction

Material	Process of dissociation of excitons	Ref.
WO_{3-x} nanosheets	Oxygen vacancy	210
$Bi_2Sn_2O_7$ QDs	Oxygen vacancy	211
$Bi_2O_2CO_3$ nanosheets	Oxygen vacancy	212
Pd-NiTiO$_3$ nanocubes	Oxygen vacancy and heterojunction	129
Polymeric carbon nitride	Nitrogen vacancy	180
Mo- and Ni co-doped CdS	Sulfur vacancy	215
Ternary metal sulfide ($Zn_{0.1}Sn_{0.1}Cd_{0.8}S$)	Sulfur vacancy	216
MoS_2/CdS	Sulfur vacancy	217
Fe-doped Bi_2MoO_6	Fe doping	219
Fe-doped BiOCl nanosheets	Fe doping and oxygen vacancy	218
Fe-doped BiOBr nanosheets	Fe doping and oxygen vacancy	220
Mo-modified $W_{18}O_{49}$	Mo doping	222
Plasmonic Au nanocrystal on Mo-doped $W_{18}O_{49}$ nanowires	Mo doping and Au loading	223
Ru single-atom modified on Mo_2CT_x MXene	Single atomic Ru modification	224
Co-doped graphitic carbon nitride	Co doping	225
Oxygen-doped g-C_3N_4	Oxygen vacancy	226
OV-In (OH)$_3$/CN heterojunction	Type-I heterojunction	133
MXene-derived TiO$_2$@C/g-C$_3$N$_4$	Type-II heterojunction	137
TiO$_2$/BiOBr heterojunction	p–n junction	139
Fe-MoS$_2$@C-TiO$_2$	Z-scheme	138
ZnO/ZnSnO$_3$/CD hybrid nanocomposite	S-scheme	149

achieved for their bulk counterpart. Feng et al.[212] successfully synthesized surface OV-modified micro-nanosheet-structured $Bi_2O_2CO_3$ (namely, BOC/OV) at room temperature. The surface OVs provided abundant active sites for N_2 activation, and the effect of scattered nanometre-size particles aided the separation of excitons. Among the catalysts synthesized, BOC/OV3 exhibited the highest NH_4^+ yield (1178 mol L^{-1} g^{-1} h^{-1}), which is 10-times more than that achieved for pristine $Bi_2O_2CO_3$.[213]

3.3.1.2 Nitrogen vacancy. Besides oxygen vacancies, to fix nitrogen, an alternative non-metal vacancy is nitrogen vacancy (NV), which can adsorb and weaken the N_2 molecule. Given that NVs have the same size and shape as that of the nitrogen atom in N_2, NVs favour the selective chemisorption and activation of N_2. NVs can also affect the electronic and band structure of nanomaterials. A variety of transition metal nitrides have been computationally studied. The findings show that VN, CrN, ZrN, and NbN have a lower onset potential for the NRR.[212]

Lv et al.[214] introduced NVs in metal-free PCN to enhance the electrocatalytic NRR. For creating NVs, PCN was calcined at 620 °C for 4 h in an argon atmosphere, which was denoted as PCN-NV4. The X-ray diffraction (XRD) analysis showed two peaks at 13.0° and 27.3° for pristine PCN, whereas for PCN-NV4, it only exhibited one broad peak at around 26.5°, as shown in Fig. 21a, which may be due to the destruction of the atomic arrangements after calcination. Fig. 21b displays the Fourier-transform infrared (FTIR) spectra, where it can be determined that the short-range structure of the s-triazine ring

(81 cm^{-1}) and aromatic C–N heterocycles (1200–1600 cm^{-1}) can be well maintained in PCN-NV4. The TEM images indicate that post-calcination has a small impact on the 2D sheet-like morphology of PCN. The XPS spectra (Fig. 21c) indicated no changes in the fitting peaks but the ratio of C–N=C and N–(C)$_3$ decreased drastically from 3.7 to 1.7, implying that NVs were forcefully introduced in PCN, as shown in Fig. 21d. The highest intensity peak for PCN-NV4 in EPR than PCN implies the presence of the maximum number of unpaired electrons in PCN-NV4 compared to PCN. The UV-Vis DRS spectra imply the increased π-electron delocalization in the conjugated system of PCN, as shown in Fig. 21f. Thus, NH_3 production should be more facile in PCN-NVs and nearly 11-times higher yield of NH_3 was realized using PCN-NVs compared to pristine PCN.

3.3.1.3 Sulfur vacancy. Ternary metal sulfides, such as ZnSnCdS and MoNiCdS, and hybrid heterojunctions such as g-C$_3$N$_4$/ZnSnCdS and g-C$_3$N$_4$/ZnMoCdS have been synthesized via the hydrothermal and calcination methods, which exhibit outstanding photocatalytic nitrogen fixation ability.[209] According to the constituent element of nitrogenase, Mo and S play an important role in the NRR. Recently, TMDCs have attracted wide attention for catalysis due to their inherent advantages such as 2D structure and tuneable bandgap for various reactions (e.g., CO_2 electroreduction and HER). Therefore, TMDCs have potential to exhibit efficient NRR catalytic performances.[212] Cao et al.[215] reported the synthesis of Mo and Ni co-doped CdS photocatalysts with different loadings of co-dopants. Among the variations, $Mo_{0.1}Ni_{0.1}Cd_{0.8}S$ exhibited the highest efficiency for PNF. The inductively coupled plasma optical emission spectroscopy (ICP-OES) analysis revealed the concentration of Mo, Ni, Cd and S, corresponding to 7.6, 5.1, 63.9 and 23.4 wt%, respectively, which suggest the actual atomic ratio of $Mo_{0.12}Ni_{0.13}Cd_{0.86}S_{1.1}$ for the optimized photocatalyst. Considering that this photocatalyst is electroneutral at the molecular level, the number of sulphur atoms is supposed to be 1.23. This signifies the formation of many SVs. Moreover, the quantitative relationship between SV concentration and PNF activity was noticeably correlated, given that the NH_4^+ generation rate was linearly related to the SV concentration ($R = 0.9754$). Similarly, Hu et al.[216] reported the synthesis of a ternary metal sulphide photocatalyst, $Zn_{0.1}Sn_{0.1}Cd_{0.8}S$, with excellent PNF activity. The SVs in $Zn_{0.1}Sn_{0.1}Cd_{0.8}S$ not only serve as active sites to adsorb and activate N_2 molecules but also stimulate interfacial charge transfer from $Zn_{0.1}Sn_{0.1}Cd_{0.8}S$ to N_2 molecules, thus significantly enhancing the PNF activity. Zheng et al.[217] reported the synthesis of a series of MoS_2/CdS heterojunctions with abundant sulphur vacancies, which was used for photocatalytic N_2 reduction. UV-Vis DRS showed that the band gap of MoS_2 and CdS is about 1.32 and 2.25 eV (Fig. 22a and b), respectively. The complementing ESR results confirmed that the defect was caused by the sulphur vacancy, revealing that CdS possesses some defects naturally ($g = 1.969$). The shift in signal from 1.969 to 2.003 after the formation of the CdS/MoS$_2$ heterojunction, which indicates that the coordination environment of
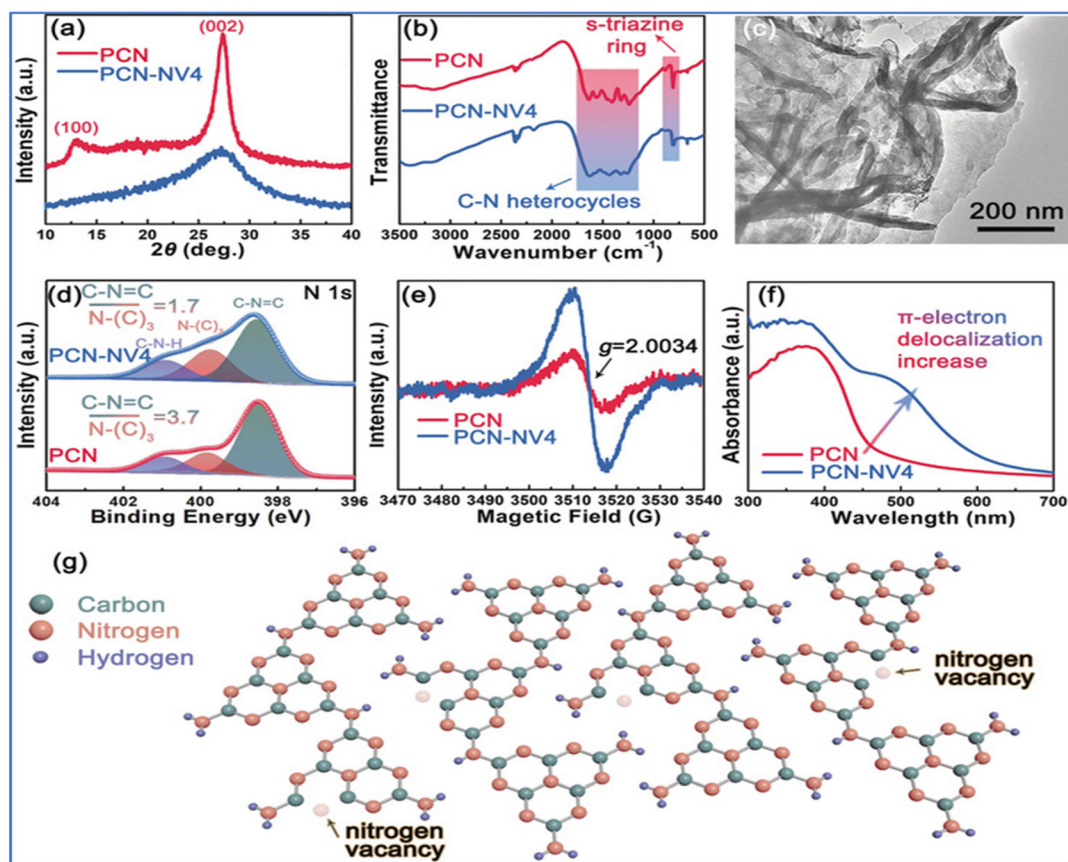
Fig. 21 (a) XRD pattern, (b) FTIR spectra, (c) TEM image, (d) N 1s XPS spectra of PCN and PCN-NV4, (e) EPR spectra, (f) UV-Vis DRS, and (g) schematic illustration of NV-engineered polymeric carbon nitride. Reproduced with permission from ref. 214. Copyright 2022, Wiley Publishing Group.
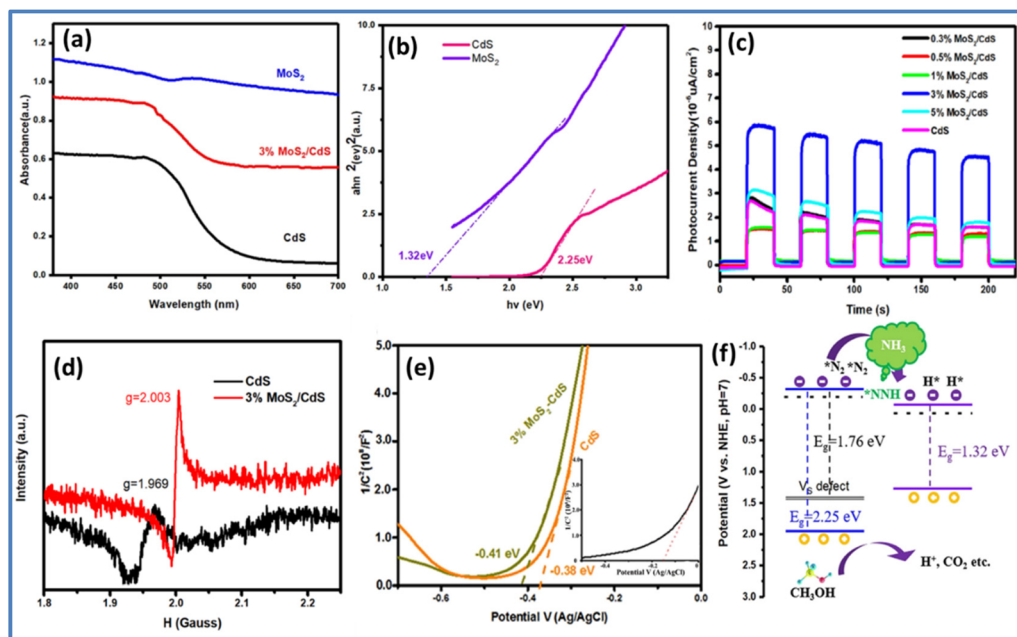

Fig. 22 (a) UV-vis DRS spectra of MoS$_2$, CdS and MoS$_2$/CdS composite, (b) corresponding plots of $(\alpha h\nu)^2$ vs. $h\nu$, (c) transient photocurrent response, (d) EPR spectra of CdS and MoS$_2$/CdS heterojunctions, (e) Mott–Schottky plots of MoS$_2$, CdS, and 3% MoS$_2$/CdS heterojunctions and (f) schematic illustration of band structures and the proposed photocatalytic mechanism of N$_2$ reduction at MoS$_2$ and CdS heterojunctions. Reproduced with permission from ref. 217. Copyright 2022, the American Chemical Society.

Cd changed. Meanwhile, the intensity of the EPR signal of 3% MoS_2/CdS was higher than that of CdS, demonstrating that more sulphur vacancies are formed in the 3% MoS_2/CdS heterojunctions (Fig. 22d). To observe the separation behaviour of electrons and holes, the transient photocurrent of the pure and heterojunction samples was investigated. It was found that the 3% MoS_2/CdS showed the highest photocurrent density, indicating the better separation efficiency of photoexcited carriers (Fig. 22c). The Mott–Schottky analysis showed the flat potential of the bare and composite samples and the mechanism of the photocatalytic nitrogen reduction reaction was proposed (Fig. 22e and f). The 3% MoS_2/CdS heterojunction exhibited more than 5.4- and 3.9-times higher ammonia yield than the bare MoS_2 and CdS, respectively.[217]

3.3.2 Heteroatom doping. Together with defect engineering, heteroatom doping provides a suitable way to generate active sites for the adsorption and activation of N_2 molecules. Generally, the doping of transition metals (TM, Fe, Co, Ag, and Cu) has been found to improve the PNF activity by enhancing visible light harvesting and activation of N_2 molecules. Because of its varying valence states, empty 3D orbitals, and low cost, Fe is a desirable dopant for nitrogen fixation. Zhang et al.[218] synthesized BiOCl NSs-Fe via a facile hydrothermal method, in which Fe act as electron sinks to form a Schottky barrier at the metal/semiconductor interface, which traps excitons, reducing the recombination process.

Fig. 23a and b illustrate the volcano-type activity of Fe-doped BiOCl NSs with OVs for the NRR as a function of Fe content. The shift in the peaks from 158.5 to 158.0 eV implies the electron transfer from Fe to Bi, and eventually the increased electron cloud density around Bi. Therefore, the modification of the electronic properties of Bi boosts the PNF activity (Fig. 23c and d). BiOCl NSs-Fe-5% exhibited a d-band centre close to the Fermi level, which suggests intense interaction with adsorbed N_2 during catalysis (Fig. 23e and f). The photocurrent density of BiOCl NSs-Fe-5% was greater than that
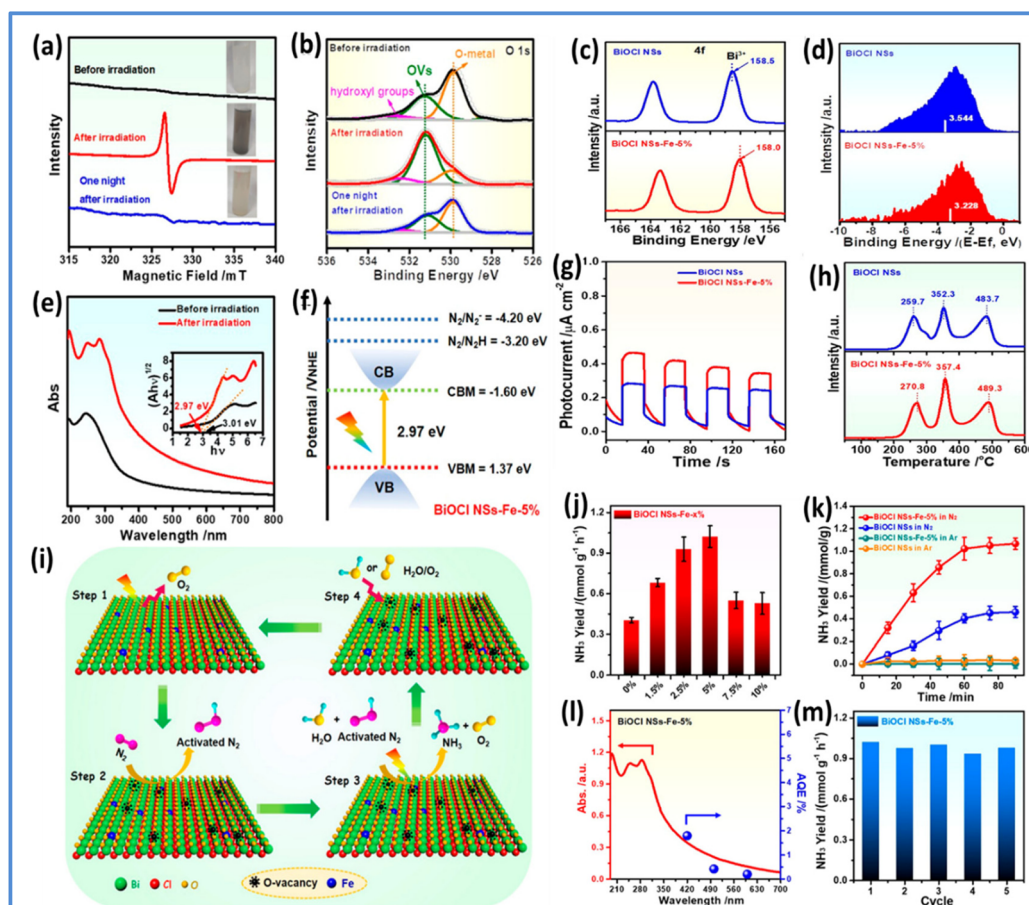

Fig. 23 (a) EPR spectra, (b) XPS O 1s spectra for BiOCl NSs-Fe-5, (c) Bi 4f XPS spectra, (d) valence band photoemission spectra, and (e) UV-vis absorption spectra and corresponding Tau plots for BiOCl NSs-Fe-5%. (f) Electronic energy-level diagram for BiOCl NSs-Fe5%, (g) photocurrent response under UV-Vis illumination, and (h) N_2-temperature-programmed desorption (TPD) profiles for BiOCl NSs and BiOCl NSs-Fe-5%. (i) Schematic illustration of the photocatalytic N_2 fixation model. (j) Photocatalytic NH_3 production rate over BiOCl NSs-Fe-x%. (k) NH_3 yield over the BiOCl NSs and BiOCl NSs-Fe-5% in N_2 and Ar. (l) Calculated AQEs (blue dots) for N_2 fixation over BiOCl NSs-Fe5% under monochromatic light irradiation. (m) Photocatalytic cycling tests for BiOCl NSs-Fe-5%. Reproduced with permission from ref. 218. Copyright 2019, the American Chemical Society.

of BiOCl NSs, suggesting enhanced charge separation (Fig. 23g and h). BiOCl NSs-Fe-5% having light-switchable surface OVs exhibited the maximum NH_3 yield rate (1.022 mmol h^{-1} g^{-1}, TOF of 0.863 h^{-1}, and AQE of 1.8% at 420 nm) and negligible activity loss after 5 cycles (Fig. 23j–m).[219]

Meng et al.[219] successfully synthesized Fe-doped Bi_2MoO_6 (BMO) via the solvothermal method. The separation of excitons and charge transfer to the catalyst surface increased as a result of the reduction in surface work function caused by Fe doping. Additionally, Fe-doping can enhance charge collection via the Fe^{3+}/Fe^{2+} redox pathway, which acts as active nitrogen reduction sites. Fe-doped Bi_2MoO_6 showed better photocatalytic activity compared to the pristine BMO, where 0.5% Fe-BMO presented a 3.7-times enhancement in PNF activity under visible light irradiation. Liu et al.[220] reported the synthesis of Fe-doped BiOBr (Fe-BiOBr) with active NRR sites that are OV-connected Fe atoms. Fe draws the electron cloud of the O atoms around it in the charge-density map of Fe-BiOBr. It was clear that the photoexcited electrons from neighboring atoms were withdrawn by the OV-connected Fe atoms to create the electron-rich Fe(II) (Fig. 24a and b). Additionally, the extra electrons in the 3d Fe orbitals signify the deposited –N≡N antibonding orbitals of N_2, facilitating N_2 activation.

Mo is also an essential component of nitrogenases, which are responsible for biological N_2 fixation, and thus numerous Mo-doped based materials for PNF have been developed and investigated.[221] Zhang et al.[222] reported the synthesis of Mo-modified $W_{18}O_{49}$, which uses Mo–W centres as the active sites for the chemisorption of N_2 molecules. Upon Mo doping, the charge difference increased between the adsorbed N atoms and the N_2-adsorption energy release, indicating that the N_2 molecule is more readily adsorbed and activated at the Mo–W centre. Therefore, the photocatalytic activity of $W_{18}O_{49}$ was greatly improved. The ESR spectrum indicated the presence of Mo–O tetragonal pyramids, where the ESR spectrum of the MWO-1 ultrathin nanowires (UTNWs) displayed a hyperfine structure with parallel (g = 1.846) and perpendicular (g = 1.907) bands. In N_2 molecules, the penta-coordination of a

doped Mo atom revealed its unsaturated coordination and left a free coordination site. Qiu et al.[223] reported the preparation of Au-decorated MWO, where the anchored Au nanocrystals not only increased the light harvesting to produce excitons but also decreased the energy of NH_3 desorption, which made it easier to release the active sites, thus further enhancing the PNF activity. In addition, Mo doping improved the adsorption and activation of N_2. Additionally, various doped transition metals can operate as active sites for N_2 adsorption and activation, including Ru, Co, and Li. Peng et al.[224] synthesized Mo_2CT_x MXene nanosheets modified by single atomic Ru. The catalyst showed an NH_3 yield rate of 40.57 μg h^{-1} mg^{-1}. DFT simulations highlighted the significance of single-atomic Ru, which served as the back donation centre for the NRR.[220] Wang et al.[225] reported the synthesis of Co-doped graphitic carbon nitride (Co-GCN) via the molten salt-assisted method. N≡N could be lengthened by the Co–N bond in Co-GCN and facilitate the processes of N_2 activation and adsorption.

3.3.3 Non-metal doping. In addition to using metal dopants, nonmetal species have been investigated as dopant active sites for nitrogen fixation reactions, particularly for electrocatalysis. Theoretical research on carbon-based materials with boron doping has been extensively undertaken. Boron acts as electron back donation centres. The effect of doping has been investigated and proven for the photocatalytic nitrogen reduction reaction. Later, it was established that N- and B-doped carbon-based materials, such as graphene, are effective catalysts for electro(photo)catalytic nitrogen reduction. Graphitic carbon nitride has fascinating potential to convert inert chemical bonds into high value-added products, but it has a low NH_3 conversion efficiency, which gives unsatisfactory results for practical application. Thus, to enhance the photocatalytic activity of g-C_3N_4, its electronic structure can be improved by doping with metal-free atoms. To increase the visible-light photocatalytic activity of g-C_3N_4, for instance, oxygen doping may change the electronic and band structure and widen the light absorbance range. Feng et al.[226] reported that sulphur-doped g-C_3N_4 improved the photo-
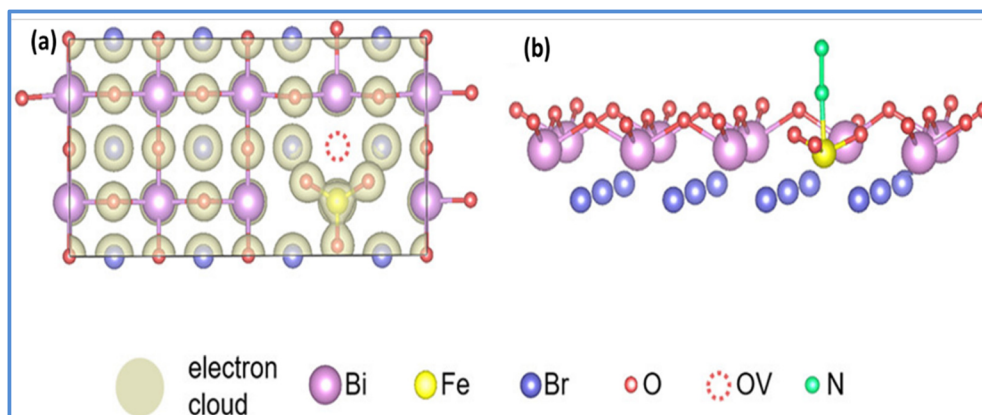

Fig. 24 (a) Charge density map of Fe-BiOBr. (b) Schematic of N_2 binding to the OV-connected Fe atom in Fe-BiOBr. Reproduced with permission from ref. 220. Copyright 2020, the American Chemical Society.

catalytic performance of g-C_3N_4 by raising the conduction band minimum and increasing the conductivity.

4 Future prospect and conclusion

This review aimed to open an avenue to design functional semiconductor materials through the modulation of excitons for solar fuel production. Compared to bulk materials, the exciton binding energy is immensely higher in low-dimensional (0D, 1D and 2D) of semiconductors. With a change in the length of different systems, 0D shows the highest binding energy and exciton energy, while bulk materials show low dependency on length. Conceptually, Wannier–Mott excitons in bulk materials can be easily disrupted by applying a low external energy; however, Frenkel excitons are forms for low-dimensional materials, which require a UV or low wavelength range light source for dissociation. Hence, excitons play a crucial role in the photocatalytic activity of low-dimensional semiconductors due to their robust coulombic attraction force, which increases the exciton binding energy and prevents the recombination of free charge carriers. Additionally, trions are formed in TMDCs, which further reduce the generation of free charge carriers. In the present review, we summarized the different approaches such as vacancy engineering, element doping, heterostructure formation, edge grafting and introduction of an order–disorder interface to facilitate the dissociation of excitons into free charge carriers. Notably, upon vacancy engineering and element doping, the stable excitons are forcefully disturbed in a semiconductor crystal for further exciton dissociation. Similarly, the introduction of several moieties into CFTs produces an intermolecular electric field, which may reduce the exciton binding. Also, by integrating single atomic S-vacancy, a PEF opposite to the coulombic attraction force arises, hindering the formation of excitons or reducing the exciton binding energy, resulting in the formation of high energetic charge carriers. In another approach, by the formation of heterostructures, the work function differences between semiconductors are higher than the exciton binding energy of each semiconductor, where the CB is more negative than the excitons, causing them to be dissociated and producing free charge carriers, which participate in photo-redox reactions. Importantly, polymeric semiconductors possesses a low charge carrier density due to their intrinsic large exciton binding energies, which restrict their photocatalytic performances. In another approach, enhanced photocatalytic activity is realized considering the direct charge transfer mechanism from exciton dissociation and excitonic energy transfer to triplet oxygen to form $^1O_2$. Further, the impact of excitons on the optimization of low–dimensional semiconductor–based photocatalysis was discussed with relevant examples. Moreover, the common characterization techniques for exciton modulation and their effect on band structure, spin polarization, etc. were described in detail. The strategic functionalization of materials with superior catalytic activity guided through theoretical approaches may significantly improve the energy conversion efficiency for scaled-up operation. Various electronic parameters such as electronic coupling, band alignment and interfacial charge transfer rate were considered to precisely regulate the catalytic performance for photocatalytic water splitting, CO_2 reduction and N_2 reduction. Hence, the modulation of electronic structure and excitons offers a promising strategy for improved activity and stability of semiconductor nanostructures for practical solar-to-fuel conversion. However, direct measurement of the electron delocalization of a group of molecules is limited and its impact on exciton dissociation is still under debate.

Solar fuel production is still in its infancy in the lab-scale and the involvement of computational studies can assist in a deeper understanding of the reaction mechanism, role of excitons in photocatalysis, exciton dynamics in semiconductors, and tuning active sites to improve the catalytic reaction kinetics. The correlation of exciton modulation with other parameters still remains impractical (current density, conversion efficiency, overpotential, etc.), which suggests that significant efforts are required in this direction. Presently, various spectroscopic tools such as EPR, TRPL, and low-temperature PL have been employed to study the excitonic effect; however, detailed analysis is required to explore the role of excitons at the interface of semiconductors and the availability of sophisticated instrumental techniques can facilitate further understanding. For example, the exciton dynamics in semiconductor nanocrystals are more complex than that in the bulk and the presence of surface states or trap states significantly alters the dynamics. Ultrafast exciton relaxation, interband electron–hole recombination, and electronic dephasing can be followed in semiconductor nanostructures by ultrafast pump probe transient absorption measurement. The effect of multiple exciton generation on photocatalysis has not been explored to date, where probing the nonlinear dynamic process at the semiconductor interface may help to improve the photocatalytic performance. Surface science together with spectro-electrochemical approaches presents an opportunity to control the surface structure and excitonic effect, which is a beneficial parameter of photocatalysis. The enhanced excitonic effect is important to develop stable and efficient semiconductor photocatalysts.

Conflicts of interest

The authors declare no conflict of interest.

Acknowledgements

References

1   J. A. Herron, J. Kim, A. A. Upadhye, G. W. Huber and C. T. Maravelias, *Energy Environ. Sci.*, 2015, **8**, 126–157.

2   H. L. Tuller, *Mater. Renewable Sustainable Energy*, 2017, **6**, 3.

3   X. Fang, S. Kalathil and E. Reisner, *Chem. Soc. Rev.*, 2020, **49**, 4926–4952.

4   S. Ghosh, *Visible-Light-Active Photocatalysis–Nanostructured Catalyst Design, Mechanisms, and Applications*, 2018.

5   L. R. Johnson, S. Sridhar, L. Zhang, K. D. Fredrickson, A. S. Raman, J. Jang, C. Leach, A. Padmanabhan, C. C. Price, N. C. Frey, A. Raizada, V. Rajaraman, S. A. Saiprasad, X. Tang and A. Vojvodic, *ACS Catal.*, 2020, **10**, 253–264.

6   Z.-B. Fang, T.-T. Liu, J. Liu, S. Jin, X.-P. Wu, X.-Q. Gong, K. Wang, Q. Yin, T.-F. Liu, R. Cao and H.-C. Zhou, *J. Am. Chem. Soc.*, 2020, **142**, 12515–12523.

7   D. F. Swearer, N. R. Knowles, H. O. Everitt and N. J. Halas, *ACS Energy Lett.*, 2019, **4**, 1505–1512.

8   M. Volokh and M. Shalom, *Nat. Catal.*, 2021, **4**, 350–351.

9   S. Sorcar, J. Thompson, Y. Hwang, Y. H. Park, T. Majima, C. A. Grimes, J. R. Durrant and S.-I. In, *Energy Environ. Sci.*, 2018, **11**, 3183–3193.

10   J. Wu, Y. Huang, W. Ye, Y. Li, J. Wu, Y. Huang, W. Ye and Y. Li, *Adv. Sci.*, 2017, **4**, 1700194.

11   X. Chen, N. Li, Z. Kong, W.-J. Ong and X. Zhao, *Mater. Horiz.*, 2018, **5**, 9–27.

12   N. Li, X. Chen, W.-J. Ong, D. R. MacFarlane, X. Zhao, A. K. Cheetham and C. Sun, *ACS Nano*, 2017, **11**, 10825–10833.

13   Y. Ren, C. Yu, X. Tan, H. Huang, Q. Wei and J. Qiu, *Energy Environ. Sci.*, 2021, **14**, 1176–1193.

14   M. J. Chalkley, M. W. Drover and J. C. Peters, *Chem. Rev.*, 2020, **120**, 5582–5636.

15   T. W. Woolerton, S. Sheard, Y. S. Chaudhary and F. A. Armstrong, *Energy Environ. Sci.*, 2012, **5**, 7470–7490.

16   H. Wang, W. Liu, X. He, P. Zhang, X. Zhang and Y. Xie, *J. Am. Chem. Soc.*, 2020, **142**, 14007–14022.

17   Y. Wang, Z. Nie and F. Wang, *Light: Sci. Appl.*, 2020, **9**, 192.

18   H. Wang, S. Jin, X. Zhang and Y. Xie, *Angew. Chem., Int. Ed.*, 2020, **59**, 22828–22839.

19   G. Swain, S. Sultana and K. Parida, *ACS Sustainable Chem. Eng.*, 2020, **8**(12), 4848–4862.

20   P. Li, K. Yuan, D.-Y. Lin, T. Wang, W. Du, Z. Wei, K. Watanabe, T. Taniguchi, Y. Ye and L. Dai, *RSC Adv.*, 2019, **9**, 35039–35044.

21   D. Wang, Q. Zhao, A. Tang and H. Yang, *Commun. Mater.*, 2022, **3**, 98.

22   T. O'Connor, M. S. Panov, A. Mereshchenko, A. N. Tarnovsky, R. Lorek, D. Perera, G. Diederich, S. Lambright, P. Moroz and M. Zamkov, *ACS Nano*, 2012, **6**, 8156–8165.

23   W. Hui, J. Sen, W. Aolei, J. Xiang, L. Wenxiu, Z. Xiaodong, Y. Wensheng, Y. Kuai, Z. Jin and X. Yi, *CCS Chem.*, 2022, **5**, 234–244.

24   W. Shao, L. Wang, H. Wang, Z. Zhao, X. Zhang, S. Jiang, S. Chen, X. Sun, Q. Zhang and Y. Xie, *J. Phys. Chem. Lett.*, 2019, **10**, 2904–2910.

25   G. Li, H. Duan, W. Cheng, C. Wang, W. Hu, Z. Sun, H. Tan, N. Li, Q. Ji, Y. Wang, Y. Lu and W. Yan, *ACS Appl. Mater. Interfaces*, 2019, **11**, 45561–45567.

26   Y. Li, H. Wang, X. Zhang, S. Wang, S. Jin, X. Xu, W. Liu, Z. Zhao and Y. Xie, *Angew. Chem., Int. Ed.*, 2021, **60**, 12891–12896.

27   L. Lei, H. Fan, Y. Jia, X. Wu, Q. Zhong and W. Wang, *Appl. Surf. Sci.*, 2022, **606**, 154938.

28   Y. Wang, W. Xu, Y. Zhang, C. Zeng, W. Zhang, L. Fu, M. Sun, Y. Wu, J. Hao, W. Zhong, Y. Du and R. Yang, *Energy Environ. Mater.*, 2022, **0**, 1–9.

29   Y. Li, H. Wang, X. Zhang, S. Wang, S. Jin, X. Xu, W. Liu, Z. Zhao and Y. Xie, *Angew. Chem., Int. Ed.*, 2021, **60**, 12891–12896.

30   W. Shao, L. Wang, H. Wang, Z. Zhao, X. Zhang, S. Jiang, S. Chen, X. Sun, Q. Zhang and Y. Xie, *J. Phys. Chem. Lett.*, 2019, **10**, 2904–2910.

31   K. L. Corp and C. W. Schlenker, *J. Am. Chem. Soc.*, 2017, **139**, 7904–7912.

32   H. Ou, X. Chen, L. Lin, Y. Fang and X. Wang, *Angew. Chem., Int. Ed.*, 2018, **57**, 8729–8733.

33   H. Sun, K. Wei, D. Wu, Z. Jiang, H. Zhao, T. Wang, Q. Zhang and P. K. Wong, *Appl. Catal., B*, 2020, **264**, 118480.

34   Z.-A. Lan, M. Wu, Z. Fang, X. Chi, X. Chen, Y. Zhang and X. Wang, *Angew. Chem., Int. Ed.*, 2021, **60**, 16355–16359.

35   G. Swain, S. Sultana and K. Parida, *ACS Sustainable Chem. Eng.*, 2020, **8**, 4848–4862.

36   K. Wu, H. Zhu, Z. Liu, W. Rodríguez-Córdoba and T. Lian, *J. Am. Chem. Soc.*, 2012, **134**, 10337–10340.

37   S. Dong, C. Liu and Y. Chen, *J. Colloid Interface Sci.*, 2019, **553**, 59–70.

38   Y. Yang, C. Zhang, D. Huang, G. Zeng, J. Huang, C. Lai, C. Zhou, W. Wang, H. Guo, W. Xue, R. Deng, M. Cheng and W. Xiong, *Appl. Catal., B*, 2019, **245**, 87–99.

39   Y. Zhang, J. Yuan, Y. Ding, B. Zhang, S. Zhang and B. Liu, *Sep. Purif. Technol.*, 2023, **304**, 122297.

40   J. S. Jang, H. G. Kim and J. S. Lee, *Catal. Today*, 2012, **185**, 270–277.

41   H. Li, C. Mao, H. Shang, Z. Yang, Z. Ai and L. Zhang, *Nanoscale*, 2018, **10**, 15429–15435.

42   A. Kumar and V. Krishnan, *Adv. Funct. Mater.*, 2021, **31**, 2009807.

43   J. Li, H. Li, G. Zhan and L. Zhang, *Acc. Chem. Res.*, 2016, **50**, 112–121.

44   S. Wang, X. Hai, X. Ding, K. Chang, Y. Xiang, X. Meng, Z. Yang, H. Chen and J. Ye, *Adv. Mater.*, 2017, **29**, 1701774.

45 M. Cheng, C. Xiao and Y. Xie, *J. Mater. Chem. A*, 2019, **7**, 19616–19633.

46 G. Zhang, Q. Ji, K. Zhang, Y. Chen, Z. Li, H. Liu, J. Li and J. Qu, *Nano Energy*, 2019, **59**, 10–16.

47 X. Chen, N. Li, Z. Kong, W.-J. Ong and X. Zhao, *Mater. Horiz.*, 2018, **5**, 9–27.

48 C. Mao, J. Wang, Y. Zou, H. Li, G. Zhan, J. Li, J. Zhao and L. Zhang, *Green Chem.*, 2019, **21**, 2852–2867.

49 H. Hirakawa, M. Hashimoto, Y. Shiraishi and T. Hirai, *J. Am. Chem. Soc.*, 2017, **139**, 10929–10936.

50 G. Dong, W. Ho and C. Wang, *J. Mater. Chem. A*, 2015, **3**, 23435–23441.

51 L. Shi, Y. Yin, S. Wang and H. Sun, *ACS Catal.*, 2020, **10**, 6870–6899.

52 T. Biswas and A. K. Singh, *npj Comput. Mater.*, 2021, **7**, 1–10.

53 J. P. Wolfe, *Phys. Today*, 1982, **35**, 46–54.

54 F. Wang, Y. Wu, M. S. Hybertsen and T. F. Heinz, *Phys. Rev. B: Condens. Matter Mater. Phys.*, 2006, **73**, 245424.

55 A. Splendiani, L. Sun, Y. Zhang, T. Li, J. Kim, C.-Y. Chim, G. Galli and F. Wang, *Nano Lett.*, 2010, **10**, 1271–1275.

56 A. J. Gillett, A. Privitera, R. Dilmurat, A. Karki, D. Qian, A. Pershin, G. Londi, W. K. Myers, J. Lee, J. Yuan, S.-J. Ko, M. K. Riede, F. Gao, G. C. Bazan, A. Rao, T.-Q. Nguyen, D. Beljonne and R. H. Friend, *Nature*, 2021, **597**, 666–671.

57 D. Qian, Z. Zheng, H. Yao, W. Tress, T. R. Hopper, S. Chen, S. Li, J. Liu, S. Chen, J. Zhang, X.-K. Liu, B. Gao, L. Ouyang, Y. Jin, G. Pozina, I. A. Buyanova, W. M. Chen, O. Inganäs, V. Coropceanu, J.-L. Bredas, H. Yan, J. Hou, F. Zhang, A. A. Bakulin and F. Gao, *Nat. Mater.*, 2018, **17**, 703–709.

58 H. Yan, M. Shen, Y. Shen, X. D. Wang, W. Lin, J. Pan, J. He, Y. X. Ye, X. Yang, F. Zhu, J. Xu, J. He and G. Ouyang, *Proc. Natl. Acad. Sci. U. S. A.*, 2022, **119**, e2202913119.

59 Y. Wang, Z. Nie and F. Wang, *Light: Sci. Appl.*, 2020, **9**, 1–16.

60 J. Sun, X. Li and J. Yang, *Nanoscale*, 2018, **10**, 3738–3743.

61 C. Liang, L. Cheng, S. Zhang, S. Yang, W. Liu, J. Xie, M.-D. Li, Z. Chai, Y. Wang and S. Wang, *J. Am. Chem. Soc.*, 2022, **144**, 2189–2196.

62 H. Wang, S. Jiang, S. Chen, X. Zhang, W. Shao, X. Sun, Z. Zhao, Q. Zhang, Y. Luo and Y. Xie, *Chem. Sci.*, 2017, **8**, 4087–4092.

63 Y. Han, L. Cao, S. Pan, X. Xu, H. Han and F. Xu, *J. Mater. Sci.*, 2018, **53**, 1326–1334.

64 Y. Lv, P. Chen, J. J. Foo, J. Zhang, W. Qian, C. Chen and W.-J. Ong, *Mater. Today Nano*, 2022, **18**, 100191.

65 M. J. Varjovi, M. E. Kilic and E. Durgun, *Phys. Rev. Mater.*, 2022, **6**, 34004.

66 *Appl. Nanophotonics*, ed. H. V. Demir and S. v. Gaponenko, Cambridge University Press, Cambridge, 2018, pp. 52–91.

67 Y. Zhong, Y. Shao, F. Ma, Y. Wu, B. Huang and X. Hao, *Nano Energy*, 2017, **31**, 84–89.

68 Y. Fu, D. Kim, W. Jiang, W. Yin, T. K. Ahn and H. Chae, *RSC Adv.*, 2017, **7**, 40866–40872.

69 J. Park, K. H. Lee, J. F. Galloway and P. C. Searson, *J. Am. Chem. Soc.*, 2008, **46**, 17849–17854.

70 X. Xu, Q. Zhang, J. Zhang, Y. Zhou and Q. Xiong, *J. Phys. D: Appl. Phys.*, 2014, **47**, 394009.

71 A. Raja, A. Chaves, J. Yu, G. Arefe, H. M. Hill, A. F. Rigosi, T. C. Berkelbach, P. Nagler, C. Schüller, T. Korn, C. Nuckolls, J. Hone, L. E. Brus, T. F. Heinz, D. R. Reichman and A. Chernikov, *Nat. Commun.*, 2017, **8**, 15251.

72 S. Wu, L. Cheng and Q. Wang, *Mater. Res. Express*, 2017, **4**, 085017.

73 J. Xiao, M. Zhao, Y. Wang and X. Zhang, *Nanophotonics*, 2017, **6**, 1309–1328.

74 B. Wu, X. Liu, J. Yin and H. Lee, *Mater. Res. Express*, 2017, **4**, 095902.

75 M. Madhu, R. Ramakrishnan, V. Vijay and M. Hariharan, *Chem. Rev.*, 2021, **121**, 8234–8284.

76 W. Popp, D. Brey, R. Binder and I. Burghardt, *Annu. Rev. Phys. Chem.*, 2021, **72**, 591–616.

77 H. Wang, X. Sun, D. Li, X. Zhang, S. Chen, W. Shao, Y. Tian and Y. Xie, *J. Am. Chem. Soc.*, 2017, **139**, 2468–2473.

78 Y. Tao, X. Yu, J. Li, H. Liang, Y. Zhang, W. Huang and Q. J. Wang, *Nanoscale*, 2018, **10**, 6294–6299.

79 W. Zhang, Z. Deng, J. Deng, C.-T. Au, Y. Liao, H. Yang and Q. Liu, *J. Mater. Chem. A*, 2022, **10**, 22419–22427.

80 Y. Shi, H. Li, C. Mao, G. Zhan, Z. Yang, C. Ling, K. Wei, X. Liu, Z. Ai and L. Zhang, *ACS ES&T Engg*, 2022, **2**, 957–974.

81 H. Ouhbi and J. Wiktor, *J. Phys. Chem. C*, 2022, **126**, 19956–19961.

82 W. Xing, W. Ma, Z. Li, A. Wang, M. Liu, J. Han, G. Wu and W. Tu, *J. Mater. Chem. A*, 2022, **10**, 18333–18342.

83 Z. Xie, W. Wang, X. Ke, X. Cai, X. Chen, S. Wang, W. Lin and X. Wang, *Appl. Catal., B*, 2023, **325**, 122312.

84 M. R. Narayan and J. Singh, *J. Appl. Phys.*, 2013, **114**, 073510.

85 K. K. Nanda, S. Swain, B. Satpati, L. Besra and Y. S. Chaudhary, *RSC Adv.*, 2014, **4**, 10928–10934.

86 D. Y. Qiu, G. Cohen, D. Novichkova and S. Refaely-Abramson, *Nano Lett.*, 2021, **21**, 7644–7650.

87 J. Sun, X. Li and J. Yang, *Nanoscale*, 2018, **10**, 3738–3743.

88 Y.-H. Chiu, K.-D. Chang and Y.-J. Hsu, *J. Mater. Chem. A*, 2018, **6**, 4286–4296.

89 C.-W. Tsao, M.-J. Fang and Y.-J. Hsu, *Coord. Chem. Rev.*, 2021, **438**, 213876.

90 M.-J. Fang, C.-W. Tsao and Y.-J. Hsu, *J. Phys. D: Appl. Phys.*, 2020, **53**, 143001.

91 T.-H. Lai, K. Katsumata and Y.-J. Hsu, *Nanophotonics*, 2021, **10**, 777–795.

92 N. J. Hestand, R. v. Kazantsev, A. S. Weingarten, L. C. Palmer, S. I. Stupp and F. C. Spano, *J. Am. Chem. Soc.*, 2016, **138**, 11762–11774.

93 Z. Pan, M. Liu, G. Zhang, H. Zhuzhang and X. Wang, *J. Phys. Chem. C*, 2021, **125**, 9818–9826.

94 X. Yu, S. Tian, F. Zhang, G. Gao, C. Zhang, Y. Han, S. Ji, H. Guo and X.-H. Jin, *ACS Sustainable Chem. Eng.*, 2022, **10**, 16182–16188.

95 X. Gao, Y. Shen, J. Liu, L. Lv, M. Zhou, Z. Zhou, Y. P. Feng and L. Shen, *J. Mater. Chem. C*, 2021, **9**, 15026–15033.

96 J. Xiao, Z. Xiao, J. Hu, X. Gao, M. Asim, L. Pan, C. Shi, X. Zhang and J.-J. Zou, *Macromolecules*, 2022, **55**, 5412–5421.

97 Z. Zeng, X. Quan, H. Yu, S. Chen, Y. Zhang, H. Zhao and S. Zhang, *Appl. Catal., B*, 2018, **236**, 99–106.

98 H. Sun, K. Wei, D. Wu, Z. Jiang, H. Zhao, T. Wang, Q. Zhang and P. K. Wong, *Appl. Catal., B*, 2020, **264**, 118480.

99 H. Guo, C.-G. Niu, C. Liang, H.-Y. Niu, Y.-Y. Yang, H.-Y. Liu, N. Tang and H.-X. Fang, *J. Chem. Eng.*, 2021, **409**, 128030.

100 Y. Yang, C. Zhang, D. Huang, G. Zeng, J. Huang, C. Lai, C. Zhou, W. Wang, H. Guo, W. Xue, R. Deng, M. Cheng and W. Xiong, *Appl. Catal., B*, 2019, **245**, 87–99.

101 H. Guo, C.-G. Niu, C.-Y. Feng, C. Liang, L. Zhang, X.-J. Wen, Y. Yang, H.-Y. Liu, L. Li and L.-S. Lin, *J. Chem. Eng.*, 2020, **385**, 123919.

102 G. Li, P. Fu, Q. Yue, F. Ma, X. Zhao, S. Dong, X. Han, Y. Zhou and J. Wang, *Chem. Catal.*, 2022, **2**, 1734–1747.

103 K. Cheng, W. Shao, H. Li, W. Guo, H. Bian, J. Han, G. Wu and W. Xing, *Ind. Crops Prod.*, 2023, **192**, 116086.

104 R. Guan, L. Wang, D. Wang, K. Li, H. Tan, Y. Chen, X. Cheng, Z. Zhao, Q. Shang and Z. Sun, *J. Chem. Eng.*, 2022, **435**, 135138.

105 M. Song, X. Deng, G. Li, Q. Wang, H. Peng, P. Chen and S.-F. Yin, *J. Mater. Chem. A*, 2022, **10**, 16448–16456.

106 A. G. Shende, T. Bhoyar, D. Vidyasagar, J. Singh, P. T. Kosankar and S. S. Umare, *ChemistrySelect*, 2021, **6**, 6707–6713.

107 G. Chen, Z.-D. Zhang, Y.-X. Liao, Z. Zhang, Y.-Z. You, G. Chen, Y.-X. Liao, Z. Zhang, Y.-Z. You and Z.-D. Zhang, *Small*, 2021, **17**, 2100698.

108 G. Zhang, Y. Xu, D. Yan, C. He, Y. Li, X. Ren, P. Zhang and H. Mi, *ACS Catal.*, 2021, **11**, 6995–7005.

109 Y. Zhang, J. Yuan, L. Zhao, B. Wu, B. Zhang, P. Zhang, S. Zhang and C. Dong, *Ceram. Int.*, 2022, **48**, 4031–4046.

110 Y. Shi, C. Zhang, Z. Yang, X. Liu, X. Zhang, C. Ling, J. Cheng, C. Liang, C. Mao and L. Zhang, *J. Phys. Chem. C*, 2022, **126**, 21847–21856.

111 L. Tian, W. Xie, X. Wu, B. Guo, G. Xie, P. Cheng, X. Liu and J. R. Gong, *J. Phys. Chem. C*, 2020, **124**, 24667–24676.

112 F. Li, L. Cheng, J. Fan and Q. Xiang, *J. Mater. Chem. A*, 2021, **9**, 23765–23782.

113 J. He, L. Hu, C. Shao, S. Jiang, C. Sun and S. Song, *ACS Nano*, 2021, **15**, 18006–18013.

114 H. Wang, D. Yong, S. Chen, S. Jiang, X. Zhang, W. Shao, Q. Zhang, W. Yan, B. Pan and Y. Xie, *J. Am. Chem. Soc.*, 2018, **140**, 1760–1766.

115 Q. Song, J. Hu, Y. Zhou, Q. Ye, X. Shi, D. Li and D. Jiang, *J. Colloid Interface Sci.*, 2022, **623**, 487–499.

116 D. Zhang, G. Tan, M. Wang, B. Li, M. Dang, H. Ren and A. Xia, *Mater. Res. Bull.*, 2020, **122**, 110685.

117 H. Wang, D. Yong, S. Chen, S. Jiang, X. Zhang, W. Shao, Q. Zhang, W. Yan, B. Pan and Y. Xie, *J. Am. Chem. Soc.*, 2018, **140**, 1760–1766.

118 Z. Ma, P. Li, L. Ye, Y. Zhou, F. Su, C. Ding, H. Xie, Y. Bai and P. K. Wong, *J. Mater. Chem. A*, 2017, **5**, 24995–25004.

119 F. Li, X. Yue, D. Zhang, J. Fan and Q. Xiang, *Appl. Catal., B*, 2021, **292**, 120179.

120 V. Carozo, Y. Wang, K. Fujisawa, B. R. Carvalho, A. McCreary, S. Feng, Z. Lin, C. Zhou, N. Perea-López, A. L. Elías, B. Kabius, V. H. Crespi and M. Terrones, *Sci. Adv.*, 2017, **3**, 1–10.

121 Y. Li, K. Xu, H. Hu, L. Jia, Y. Zhang, C. Zhuoga, P. Yang, X. Tan, W. Guo, W. Hao, T. Yu and J. Ye, *J. Chem. Eng.*, 2022, **450**, 138106.

122 X. He, S. Bai, J. Jiang, W. J. Ong, J. Peng, Z. Xiong, G. Liao, J. Zou and N. Li, *Chem. Eng. J. Adv.*, 2021, **8**, 100175.

123 M. Shen, L. Zhang, M. Wang, J. Tian, X. Jin, L. Guo, L. Wang and J. Shi, *J. Mater. Chem. A*, 2019, **7**, 1556–1563.

124 B. Wang, S. Z. Yang, H. Chen, Q. Gao, Y. X. Weng, W. Zhu, G. Liu, Y. Zhang, Y. Ye, H. Zhu, H. Li and J. Xia, *Appl. Catal., B*, 2020, **277**, 119170.

125 Y. Zhang, D. Yao, B. Xia, H. Xu, Y. Tang, K. Davey, J. Ran and S.-Z. Qiao, *Small Sci.*, 2021, **1**, 2000052.

126 Q. Song, J. Hu, Y. Zhou, Q. Ye, X. Shi, D. Li and D. Jiang, *J. Colloid Interface Sci.*, 2022, **623**, 487–499.

127 Y.-P. Yuan, L.-W. Ruan, J. Barber, S. C. J. Loo and C. Xue, *Energy Environ. Sci.*, 2014, **7**, 3934–3951.

128 Y. Subramanian, B. Mishra, R. P. Mishra, N. Kumar, S. Bastia, S. Anwar, R. Gubendiran and Y. S. Chaudhary, *New J. Chem.*, 2022, **46**, 11851–11861.

129 K. K. Nanda, S. Swain, B. Satpati, L. Besra, B. Mishra and Y. S. Chaudhary, *ACS Appl. Mater. Interfaces*, 2015, **7**, 7970–7978.

130 J. Lee, L.-L. Tan and S.-P. Chai, *Nanoscale*, 2021, **13**, 7011–7033.

131 L. Zhang, S. Hou, T. Wang, S. Liu, X. Gao, C. Wang and G. Wang, *Small*, 2022, **18**, 2202252.

132 Y. Shi, G. Zhan, H. Li, X. Wang, X. Liu, L. Shi, K. Wei, C. Ling, Z. Li, H. Wang, C. Mao, X. Liu and L. Zhang, *Adv. Mater.*, 2021, **33**, 2100143.

133 J. Fan, M. Zuo, Z. Ding, Z. Zhao, J. Liu and B. Sun, *J. Chem. Eng.*, 2020, **396**, 125263.

134 V. Devthade, A. Gupta and S. S. Umare, *ACS Appl. Nano Mater.*, 2018, **1**, 5581–5588.

135 P. Xing, P. Chen, Z. Chen, X. Hu, H. Lin, Y. Wu, L. Zhao and Y. He, *ACS Sustainable Chem. Eng.*, 2018, **6**, 14866–14879.

136 S. Bera, S. Ghosh and R. N. Basu, *New J. Chem.*, 2018, **42**, 541–554.

137 Q. Liu, L. Ai and J. Jiang, *J. Mater. Chem. A*, 2018, **6**, 4102–4110.

138 Q. Song, C. Sun, Z. Wang, X. Bai, K. Wu, Q. Li, H. Zhang, L. Zhou, H. Pang, Y. Liang, S. Yue and Z. Zhao, *Mater. Today Phys.*, 2021, **21**, 100563.

139 J. Wang, Y. Fang, W. Zhang, X. Yu, L. Wang and Y. Zhang, *Appl. Surf. Sci.*, 2021, **567**, 150623.

140 L. Wang, W. Wu, K. Liang and X. Yu, *Energy Fuels*, 2022, **36**, 11278–11291.

141 K. Zhang, Z. Ai, M. Huang, D. Shi, Y. Shao, X. Hao, B. Zhang and Y. Wu, *J. Catal.*, 2021, **395**, 273–281.

142 E. Vesali-Kermani, A. Habibi-Yangjeh and S. Ghosh, *Ceram. Int.*, 2020, **46**, 24472–24482.

143 S. Ghosh, H. Remita and R. N. Basu, *Appl. Catal., B*, 2018, **239**, 362–372.

144 S. Ghosh, S. R. Keshri, S. Bera and R. N. Basu, *Int. J. Hydrogen Energy*, 2020, **45**, 6159–6173.

145 S. Sardar, P. Kar, H. Remita, B. Liu, P. Lemmens, S. K. Pal and S. Ghosh, *Sci. Rep.*, 2015, **5**, 17313.

146 S. Bera, S. Ghosh, T. Maiyalagan and R. N. Basu, *ACS Appl. Energy Mater.*, 2022, **5**, 3821–3833.

147 S. Bera, S. Ghosh and R. N. Basu, *J. Alloys Compd.*, 2020, **830**, 154527.

148 Q. Xu, L. Zhang, B. Cheng, J. Fan and J. Yu, *Chem*, 2020, **6**, 1543–1559.

149 V.-H. Nguyen, M. Mousavi, J. B. Ghasemi, Q. van Le, S. A. Delbari, M. S. Asl, M. Mohammadi, M. Shokouhimehr and A. S. Namini, *J. Taiwan Inst. Chem. Eng.*, 2021, **118**, 140–151.

150 S. Samajdar, S. Bera, P. S. Das, H. Finch, V. R. Dhanak, S. Chakraborty, T. Maiyalagan, K. Annapurna and S. Ghosh, *Int. J. Hydrogen Energy*, 2023, **48**, 17838–17851.

151 Y. Wang, Z. Hu, W. Wang, H. He, L. Deng, Y. Zhang, J. Huang, N. Zhao, G. Yu and Y. N. Liu, *Chem. Sci.*, 2021, **12**, 16065–16073.

152 Z. Pan, M. Liu, G. Zhang, H. Zhuzhang and X. Wang, *J. Phys. Chem. C*, 2021, **125**, 9818–9826.

153 C. Cui, X. Zhao, X. Su, N. Xi, X. Wang, X. Yu, X. L. Zhang, H. Liu and Y. Sang, *Adv. Funct. Mater.*, 2022, **32**, 2208962.

154 L. Hu, J. Huang, J. Wang, S. Jiang, C. Sun and S. Song, *Appl. Catal., B*, 2023, **320**, 121945.

155 J. Wang, S. Jiang, C. Sun and S. Song, *J. Chem. Eng.*, 2023, **452**, 139468.

156 Y. Qian, D. Li, Y. Han and H.-L. Jiang, *J. Am. Chem. Soc.*, 2020, **142**, 20763–20771.

157 R. Zha, T. Shi, L. He and M. Zhang, *J. Chem. Eng.*, 2021, **421**, 129883.

158 D. Zhang, P. Wang, J. Wang, Y. Li, Y. Xia and S. Zhan, *Proc. Natl. Acad. Sci. U. S. A.*, 2021, **118**, 1–9.

159 R. Guan, L. Wang, D. Wang, K. Li, H. Tan, Y. Chen, X. Cheng, Z. Zhao, Q. Shang and Z. Sun, *J. Chem. Eng.*, 2022, **435**, 135138.

160 Z. Pan, M. Liu, G. Zhang, H. Zhuzhang and X. Wang, *J. Phys. Chem. C*, 2021, **125**, 9818–9826.

161 F. Liu, Y. He, X. Liu, Z. Wang, H.-L. Liu, X. Zhu, C.-C. Hou, Y. Weng, Q. Zhang and Y. Chen, *ACS Catal.*, 2022, **12**, 9494–9502.

162 A. R. Clapp, I. L. Medintz and H. Mattoussi, *ChemPhysChem*, 2006, **7**, 47–57.

163 Y.-C. Cheng and G. R. Fleming, *Annu. Rev. Phys. Chem.*, 2009, **60**, 241–262.

164 I. Nabiev, A. Rakovich, A. Sukhanova, E. Lukashev, V. Zagidullin, V. Pachenko, Y. P. Rakovich, J. F. Donegan, A. B. Rubin and A. O. Govorov, *Angew. Chem., Int. Ed.*, 2010, **49**, 7217–7221.

165 C. P. Hsu, *Acc. Chem. Res.*, 2009, **42**, 509–518.

166 C. B. Murphy, Y. Zhang, T. Troxler, V. Ferry, J. J. Martin and W. E. Jones, *J. Phys. Chem. B*, 2004, **108**, 1537–1543.

167 J. Ding, Z. Dai, F. Tian, B. Zhou, B. Zhao, H. Zhao, Z. Chen, Y. Liu and R. Chen, *J. Mater. Chem. A*, 2017, **5**, 23453–23459.

168 Y. Shi, H. Li, C. Mao, G. Zhan, Z. Yang, C. Ling, K. Wei, X. Liu, Z. Ai and L. Zhang, *ACS ES&T Engg*, 2022, **2**, 957–974.

169 H. Wang, S. Jiang, S. Chen, X. Zhang, W. Shao, X. Sun, Z. Zhao, Q. Zhang, Y. Luo and Y. Xie, *Chem. Sci.*, 2017, **8**, 4087–4092.

170 G. Yu, W. Li, H. Gao, M. Zhang, Y. Guo and S. Chen, *J. Phys. Chem. Lett.*, 2022, **13**, 2814–2823.

171 H. Wang, S. Jiang, S. Chen, D. Li, X. Zhang, W. Shao, X. Sun, J. Xie, Z. Zhao, Q. Zhang, Y. Tian and Y. Xie, *Adv. Mater.*, 2016, **28**, 6940–6945.

172 A. K. Singh, J. H. Montoya, J. M. Gregoire and K. A. Persson, *Nat. Commun.*, 2019, **10**(1), 1–9.

173 Z. Ma, P. Li, L. Ye, Y. Zhou, F. Su, C. Ding, H. Xie, Y. Bai and P. K. Wong, *J. Mater. Chem. A*, 2017, **5**, 24995–25004.

174 F. Li, X. Yue, D. Zhang, J. Fan and Q. Xiang, *Appl. Catal., B*, 2021, **292**, 120179.

175 J. Yang, L. Jing, X. Zhu, W. Zhang, J. Deng, Y. She, K. Nie, Y. Wei, H. Li and H. Xu, *Appl. Catal., B*, 2023, **320**, 122005.

176 A. K. Singh, L. Zhou, A. Shinde, S. K. Suram, J. H. Montoya, D. Winston, J. M. Gregoire and K. A. Persson, *Chem. Mater.*, 2017, **29**, 10159–10167.

177 A. Bafaqeer, M. Tahir, A. A. Khan and N. A. Saidina Amin, *Ind. Eng. Chem. Res.*, 2019, **58**, 8612–8624.

178 T. R. Kafle, B. Kattel, S. Wanigasekara, T. Wang and W.-L. Chan, *Adv. Energy Mater.*, 2020, **10**, 1904013.

179 B. Wu, T. Sun, N. Liu, L. Lu, R. Zhang, W. Shi and P. Cheng, *ACS Appl. Mater. Interfaces*, 2022, **14**, 26742–26751.

180 L. Zhang, S. Hou, T. Wang, S. Liu, X. Gao, C. Wang and G. Wang, *Small*, 2022, **18**, 2202252.

181 X. Li, J. Zhu and B. Wei, *Chem. Soc. Rev.*, 2016, **45**, 3145–3187.

182 K. Das and S. K. De, *J. Phys. Chem. C*, 2009, **113**, 3494–3501.

183 F. Meng, J. Li, S. K. Cushing, M. Zhi and N. Wu, *J. Am. Chem. Soc.*, 2013, **135**, 10286–10289.

184 J. Li, L. Zhang, Y. Li and Y. Yu, *Nanoscale*, 2014, **6**, 167–171.

185 J. Li, L. Cai, J. Shang, Y. Yu and L. Zhang, *Adv. Mater.*, 2016, **28**, 4059–4064.

186 J. Li, G. Zhan, Y. Yu and L. Zhang, *Nat. Commun.*, 2016, **7**, 1–9.

187 J. Li, X. Guo, L. Gan, Z.-F. Huang, L. Pan, C. Shi, X. Zhang, G. Yang and J.-J. Zou, *ACS Appl. Energy Mater.*, 2022, **5**, 9241–9265.

188 R. R. Schrock, *Acc. Chem. Res.*, 2005, **38**, 955–962.

189 Y. Abghoui and E. Skúlason, *Catal. Today*, 2017, **286**, 69–77.

190 C. Ling, Y. Zhang, Q. Li, X. Bai, L. Shi and J. Wang, *J. Am. Chem. Soc.*, 2019, **141**, 18264–18270.

191 Y. Abghoui, A. L. Garden, J. G. Howalt, T. Vegge and E. Skúlason, *ACS Catal.*, 2016, **6**, 635–646.

192 G. N. Schrauzer and T. D. Guth, *J. Am. Chem. Soc.*, 2002, **99**, 7189–7193.

193 G. Li, G. R. Blake and T. T. M. Palstra, *Chem. Soc. Rev.*, 2017, **46**, 1693–1706.

194 S. Bai, N. Zhang, C. Gao and Y. Xiong, *Nano Energy*, 2018, **53**, 296–336.

195 S. Bastia, N. Kumar, R. P. Mishra, S. Swain and Y. S. Chaudhary, *ACS Apply. Mater. Interfaces*, 2023, **15**, 13052–13063.

196 W. Zhou and H. Fu, *Inorg. Chem. Front.*, 2018, **5**, 1240–1254.

197 M. Kong, Y. Li, X. Chen, T. Tian, P. Fang, F. Zheng and X. Zhao, *J. Am. Chem. Soc.*, 2011, **133**, 16414–16417.

198 L. Li, J. Yan, T. Wang, Z. J. Zhao, J. Zhang, J. Gong and N. Guan, *Nat. Commun.*, 2015, **6**, 1–10.

199 H. Hirakawa, M. Hashimoto, Y. Shiraishi and T. Hirai, *J. Am. Chem. Soc.*, 2017, **139**, 10929–10936.

200 Y. Mao, P. Wang, L. Li, Z. Chen, H. Wang, Y. Li and S. Zhan, *Angew. Chem., Int. Ed.*, 2020, **59**, 3685–3690.

201 H. Feng, Z. Xu, L. Ren, C. Liu, J. Zhuang, Z. Hu, X. Xu, J. Chen, J. Wang, W. Hao, Y. Du and S. X. Dou, *ACS Catal.*, 2018, **8**, 4288–4293.

202 B. Mishra, S. Mishra, B. Satpati and Y. S. Chaudhary, *ChemSusChem*, 2019, **12**, 3383–3389.

203 M. Cheng, C. Xiao and Y. Xie, *J. Mater. Chem. A*, 2019, **7**, 19616–19633.

204 X. Yan, D. Liu, H. Cao, F. Hou, J. Liang and S. X. Dou, *Small Methods*, 2019, **3**, 1800501.

205 P. Naliwajko and J. Strunk, in *Heterogeneous Photocatalysis*, 2021, pp. 101–126.

206 Y. Lv, Y. Liu, Y. Zhu and Y. Zhu, *J. Mater. Chem. A*, 2014, **2**, 1174–1182.

207 L. Xu, Q. Jiang, Z. Xiao, X. Li, J. Huo, S. Wang and L. Dai, *Angew. Chem., Int. Ed.*, 2016, **55**, 5277–5281.

208 L. Zhuang, L. Ge, Y. Yang, M. Li, Y. Jia, X. Yao and Z. Zhu, *Adv. Mater.*, 2017, **29**, 1606793.

209 D. Yan, H. Li, C. Chen, Y. Zou and S. Wang, *Small Methods*, 2019, **3**, 1800331.

210 Z. Yang, J. Wang, J. Wang, M. Li, Q. Cheng, Z. Wang, X. Wang, J. Li, Y. Li and G. Zhang, *Langmuir*, 2022, **38**, 1178–1187.

211 Y. Zhang, J. Di, X. Qian, M. Ji, Z. Tian, L. Ye, J. Zhao, S. Yin, H. Li and J. Xia, *Appl. Catal., B*, 2021, **299**, 120680.

212 Y. Feng, Z. Zhang, K. Zhao, S. Lin, H. Li and X. Gao, *J. Colloid Interface Sci.*, 2021, **583**, 499–509.

213 X. Xue, R. Chen, H. Chen, Y. Hu, Q. Ding, Z. Liu, L. Ma, G. Zhu, W. Zhang, Q. Yu, J. Liu, J. Ma and Z. Jin, *Nano Lett.*, 2018, **18**, 7372–7377.

214 C. Lv, Y. Qian, C. Yan, Y. Ding, Y. Liu, G. Chen and G. Yu, *Angew. Chem.*, 2018, **130**, 10403–10407.

215 Y. Cao, S. Hu, F. Li, Z. Fan, J. Bai, G. Lu and Q. Wang, *RSC Adv.*, 2016, **6**, 49862–49867.

216 S. Hu, X. Chen, Q. Li, Y. Zhao and W. Mao, *Catal. Sci. Technol.*, 2016, **6**, 5884–5890.

217 X. Zheng, H. Han, J. Liu, Y. Yang, L. Pan, S. Zhang, S. Meng and S. Chen, *ACS Appl. Energy Mater.*, 2022, **5**, 4475–4485.

218 N. Zhang, L. Li, Q. Shao, T. Zhu, X. Huang and X. Xiao, *ACS Appl. Energy Mater.*, 2019, **2**, 8394–8398.

219 Q. Meng, C. Lv, J. Sun, W. Hong, W. Xing, L. Qiang, G. Chen and X. Jin, *Appl. Catal., B*, 2019, **256**, 117781.

220 Y. Liu, Z. Hu and J. C. Yu, *Chem. Mater.*, 2020, **32**, 1488–1494.

221 Y.-G. Liu, M. Tian, J. Hou and H.-Y. Jiang, *Energy Fuels*, 2022, **36**, 11323–11358.

222 N. Zhang, A. Jalil, D. Wu, S. Chen, Y. Liu, C. Gao, W. Ye, Z. Qi, H. Ju, C. Wang, X. Wu, L. Song, J. Zhu and Y. Xiong, *J. Am. Chem. Soc.*, 2018, **140**, 9434–9443.

223 P. Qiu, C. Huang, G. Dong, F. Chen, F. Zhao, Y. Yu, X. Liu, Z. Li and Y. Wang, *J. Mater. Chem. A*, 2021, **9**, 14459–14465.

224 W. Peng, M. Luo, X. Xu, K. Jiang, M. Peng, D. Chen, T.-S. Chan and Y. Tan, *Adv. Energy Mater.*, 2020, **10**, 2001364.

225 K. Wang, G. Gu, S. Hu, J. Zhang, X. Sun, F. Wang, P. Li, Y. Zhao, Z. Fan and X. Zou, *J. Chem. Eng.*, 2019, **368**, 896–904.

226 X. Feng, H. Chen, F. Jiang and X. Wang, *J. Colloid Interface Sci.*, 2018, **509**, 298–306.